博 士 学 位 論 文
Doctoral Thesis

論文題目

Thesis Title

Effect of Helium Ion Irradiation on Spin and Magnetic Properties of Ta/CoFeB Structures

東 北 大 学 大 学 院 工 学 研 究 科

Graduate School of Engineering,

TOHOKU UNIVERSITY

専攻/Department: 知能デバイス材料学

学籍番号/ ID No: C0TD9503

氏 名 /Name: LIAO Qixian

Effect of Helium Ion Irradiation on Spin and Magnetic Properties of Ta/CoFeB Structures

ABSTRACT : As a promising engineering technology, the application of Helium ion irradiation is attracting more and more interest for spintronic devices, especially domain wall-based racetrack memory, since the advantages of precise control, significant improvement, modification on the pinning sites, and short processing time. Although many studies about the effects of Helium ion irradiation are reported, showing appreciable improvement in the performance, most of them are focusing on the effects on magnetic properties or domain wall motion and non-self-consistent effects are reported with reasons unknown, which suggests the research on the effects of Helium ion irradiation are still insufficient, and more physics behind has not been revealed well.

On the one hand, heavy metal/ferromagnetic (HM/FM) bilayers have been investigated a lot for the application of spin orbit-torque (SOT) driven domain wall (DW)-based racetrack memory in recent years because of the strong spin-orbit coupling in HM, which is possible to offer a high charge-to-spin conversion efficiency. Ta/CoFeB with perpendicular magnetic anisotropy (PMA) property is an archetypal structure for spintronic devices, which is already used in devices like magnetic tunnel junctions (MTJ) since the high spin Hall angle and PMA.

On the other hand, the typical DW-based racetrack memory requires an external field to drive the domain wall motion, which limits the application. Current-driven DW-based devices can obtain a very high DW velocity, but the Joule heat is an unavoidable problem in practical devices. SOT-driven DW-based devices can reduce the problem of Joule heat. However, a material with a high spin Hall angle is necessary—one of the feasible ways to improve the performance of new spintronic engineering technologies. Therefore, our motivation is to clarify the effects of Helium ion irradiation to promote its application for improving the performance of DW-based devices.

In this work, we systematically investigated the effects of Helium ion irradiation on the spin and magnetic properties of Ta/CoFeB structures. The samples of Ta/CoFeB with different thicknesses of the Ta layer are deposited and annealed for PMA and then irradiated by different doses. The different thicknesses of Ta lead to different properties in microscopic, and the dose-dependent effects can show the effects of the He ion irradiation.

First, to investigate the effects on magnetic properties, the M-H loop of irradiated samples is measured along the easy axis for extracting the saturation magnetization m_s and coercivity field h_c. The results show a significant difference between the thicker Ta(3,4)/CoFeB(1) and the thinner Ta(2)/CoFeB(1) samples, though all of them still keep PMA, suggesting their microscopic difference. The thicker group of Ta(3,4)/CoFeB(1) keeps a constant ms after irradiation, which is an advantage in device application for stability. On the opposite, the m_s of the thinner Ta(2)/CoFeB(1) shows a significant non-monotonic tendency. The m_s increases by about 30% in lower doses and then decreases again in higher doses. By measuring the X-ray Diffraction (XRD) patterns, we figure out that the increase of m_s is due to the increase in crystallinity and, for the first time, demonstrate that a new CoFe (110) phase is created only in Ta(2)/CoFeB(1) after irradiation. In the case of higher doses, the m_s decreases because the accumulated defects from the Helium ion irradiation damage the crystallinity of CoFe (001), which is the

dominant contribution to ms and PMA. Therefore, the m_s turns to decrease even if the crystallinity of CoFe (110) is still increasing.

Second, we measured the domain wall motion of irradiated Ta/CoFeB samples with Kerr microscopy by the domain expansion in identical magnetic field pulses. The extracted slope ζ is a critical parameter characterizing whether the domain wall motion is easy or not. A low value of ζ is supposed to improve the performance of DW-based devices. In the group of the thicker Ta(3,4)/CoFeB(1) samples, we found both the same tendency and a minimal point in the irradiation dose 6×10^{14} He^+/cm^2. However, in the group of the thinner Ta(2)/CoFeB(1), the tendency is opposite to the thicker group, showing a concave functional dependence on the irradiation doses. According to the model of the domain wall motion in the creep regime, the slope ζ depends on the materials parameters with a relationship $\zeta \propto m_s^{-\frac{1}{4}} K_{eff}^{\frac{5}{8}} n_i^{\frac{1}{2}}$. Following this relationship, we measured the effective magnetic anisotropy K_{eff} and compared the tendencies of ζ, m_s, and K_{eff}. We found that the m_s and K_{eff} of Ta(3,4)/CoFeB(1) keep almost constant values after irradiation, which means the dominant contribution to the change of ζ is from the pinning density n_i. The pinning density of thicker samples is reduced by irradiation. In the case of Ta(2)/CoFeB(1), we found the main contribution is from K_{eff}, though the contribution from n_i can not be separated. In Ta(2)/CoFeB(1), the change of K_{eff} shows the same tendency with m_s, suggesting that the crystallization of CoFe (110) should be the typical reason.

Third, we analyzed the SOT properties of irradiated Ta/CoFeB samples using the harmonic Hall method. The SOT of Ta(2)/CoFeB is decreased in the lower doses and reaches the minimum in the dose 8×10^{14} He^+/cm^2. The same tendency of SOT with ms and Keff suggests the main reason should be the unexpected crystallization. On the other hand, the SOT of Ta(3,4)/CoFeB(1) increased to double in doses 6×10^{14} He^+/cm^2 and 8×10^{14} He^+/cm^2, demonstrating the significant improvement by the Helium ion irradiation technology. However, the maximum point of the Ta(4)/CoFeB(1) is shifted to the higher dose due to the volume effects, which leads to a mismatch of the sweet spot between the domain wall motion and SOT.

Combining the results of magnetic properties, domain wall motion, and SOT, we figure out that the Helium ion irradiation is sensitive to the thickness of samples, and the Ta(3)/CoFeB(1) structure with irradiation dose 6×10^{14} He^+/cm^2 is the optimal design for improving the performance.

TOHOKU UNIVERSITY

DOCTORAL THESIS

Effect of Helium Ion Irradiation on Spin and Magnetic Properties of Ta/CoFeB Structures

---

Author:

LIAO Qixian

Supervisor:

Professor Makoto Kohda

A thesis submitted in fulfillment of the requirements for the Doctor of Philosophy (Engineering)

of the

GP-Spin Program
Materials Science
Graduate School of Engineering

January 19, 2024

Declaration of Authorship

I, LIAO Qixian, declare that this thesis titled, “Effect of Helium Ion Irradiation on Spin and Magnetic Properties of Ta/CoFeB Structures” and the work presented in it are my own. I confirm that:

- This work was done wholly or mainly while in candidature for a research degree at this University.
- Where any part of this thesis has previously been submitted for a degree or any other qualification at this University or any other institution, this has been clearly stated.
- Where I have consulted the published work of others, this is always clearly attributed.
- Where I have quoted from the work of others, the source is always given. With the exception of such quotations, this thesis is entirely my own work.
- I have acknowledged all main sources of help.
- Where the thesis is based on work done by myself jointly with others, I have made clear exactly what was done by others and what I have contributed myself.

Signed:

_____

Date:

_____

Contents

List of Figures

List of Tables

Chapter 1

Introduction and Background

1.1 Spintronic Devices

With the development of computer science and information technology, the thirst of human beings for devices with excellent performance never stops. The increasing requirement promoted the development of devices, which are the traditional electronic devices that we are widely using.

After many years of development, traditional electronic devices have many advantages, as shown in figure 1.1. Electronic devices make use of the charge of electrons, which means it is simple to control. To fabricate many devices, mature modification engineering is developed to control the properties of materials, and a mature integrated circuit (IC) is designed for the application. However, traditional electronic devices still can not satisfy all the requirements, for example, memory devices with high response speeds like random-access memory (RAM), which is volatile.

Spintronic devices, which make use of the spin of electrons, may satisfy such requirements. As shown in figure 1.1, it has many advantages.

In this thesis, we will investigate the effect of Helium ion irradiation on spin and magnetic properties of Ta/CoFeB Structures to clarify the impact of He^+ ion irradiation on both domain wall motion and spin-orbit torque (SOT) in Ta/CoFeB thin film for domain wall (DW) devices.

1.1.1 Spin-Orbit Torque Driven Domain Wall Memory Devices

Since the high efficiency of domain wall motion, especially in the out-of-plane magnetized ferromagnets, the application of DW-based memory attracts high attention.[1, 2, 3, 4, 5] The schematic of such a device is shown in figure **??**. The device is driven by the SOT of the injected current in the heavy metal layer.

1.2 Spintronic Engineering

1.2.1 Common Technologies of Spintronic Engineering

As a standard technology of spintronic engineering, annealing is usually used for obtaining the perpendicular magnetic anisotropy (PMA) property, as shown in figure 1.2. The PMA features are essential for developing spintronic devices such as magnetic tunnel junctions. However, in the annealing process, the entire substrate has to be annealed together, which limits its application on the circuits integrated with other devices. The annealing process is usually not precise and uniform and leads to the deterioration of the interface. Moreover, a long processing time, such as 1 or 2 hours, is necessary for the annealing process, which would be the bottleneck in production.

Ion implantation is another engineering technology for modifying the properties of spintronic devices, which is developed from traditional electronic devices. The ions of certain elements are accelerated and implanted into the thin films, as shown in figure 1.3. Such a technology has many advantages that are friendly to production, such as short processing time and precise area control. However, it also leads to massive defects because the ion will stay in the thin films.

1.2.2 He^+ Ion Irradiation Technology

He^+ ion irradiation technology is a kind of new technology aiming to solve those problems as shown in figure 1.4.

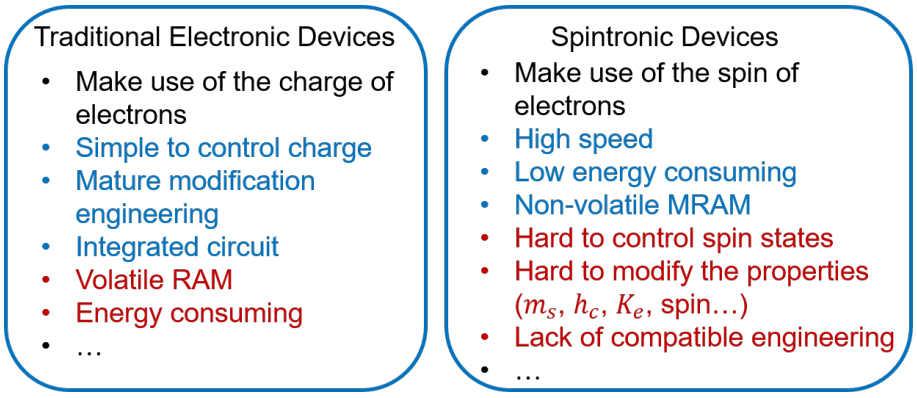

FIGURE 1.1: The comparison between spintronic devices and traditional electronic devices.

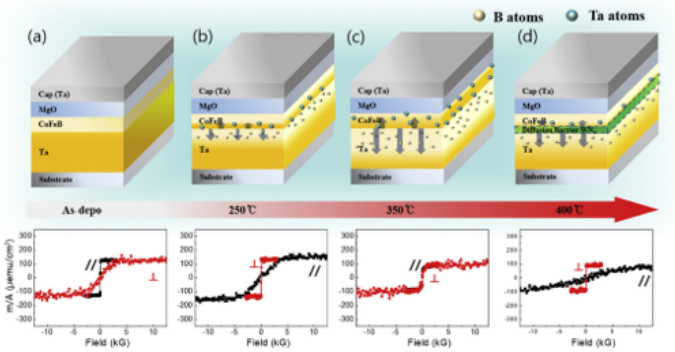

FIGURE 1.2: The annealing process on Ta/CoFeB/MgO for PMA property. Adapted from Ref. [6].

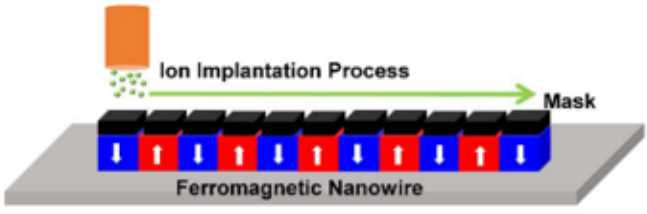

Fig. 10. Schematic of ion implantation process through mask for creating local modifications in magnetic properties along a ferromagnetic nanowire.

FIGURE 1.3: The schematic of the ion implantation process. Adapted from Ref. [5].

1.3 Objectives

As for the advantages and the present problems of the He^+ ion irradiation technology, the objective of this thesis is set, which is *to clarify the effects of He^+ ion irradiation on both domain wall motion and spin-orbit torque in Ta/CoFeB thin film for domain wall devices*. To reach this objective, we must start step-by-step and separate it into three sub-objectives.

Sub-objective 1: *The dose-dependent effect on the magnetic properties and the origin of it.*

The magnetic properties are the basis of the spintronic devices, and it would be critically helpful for understanding the domain wall dynamics of irradiated thin films. Moreover, it is easier to measure compared with the SOT properties. Thus, we start by investigating the magnetic properties of irradiated thin films. The different effects also show the different origins and the relationship between crystallization and irradiation. We will focus on the saturation magnetization m_s in Chapter 3 and the effective magnetic anisotropy K_{eff} in Chapter 4.

Sub-objective 2: *To clarify the domain wall motion of irradiated samples, figuring out the microscopic pinning properties.*

The domain wall motion is directly relative to the performance of domain-based devices; thus, how the irradiation modifies the domain wall dynamics should be investigated. With the results of the magnetic properties, we can interpret the results of domain wall motion measurements and elucidate the effect on the microscopic pinning properties by excluding the contribution from m_s and K_{eff}. This work is shown in Chapter 4.

Sub-objective 3: *To analyze the spin-orbit torque of irradiated samples for determining the modulation from He^+ ion irradiation using the harmonic Hall method.*

The SOT property of materials is always the key to spintronic device applications. However, the researches on the SOT effects from the He^+ ion irradiation are very insufficient. Here, we demonstrated the SOT results of the irradiation on Ta/CoFeB

and further figured out the sensitivity to the thickness of the Ta layer. This part is shown in Chapter 5.

1.4 Outline of Thesis

Chapter 1 introduces the background of the He^+ ion irradiation technology and its advantages and disadvantages. The background of the device application and some main concepts are included. The motivation and the target of this work are introduced.

Chapter 2 explains the method of sample deposition and device fabrication. In this work, we used the RF magnetron sputtering to deposit the Ta/CoFeB samples. The characterization methods for irradiated samples are described, and the details and parameters of measurements, including the deposition, irradiation process, and device fabrication, are shown.

Chapter 3 demonstrates the different effects of He^+ ion irradiation on the magnetic property of Ta/CoFeB thin films, which shows two completely different behaviors, separating the samples into two groups. To identify the origin, XRD measurements are processed, and the crystallization of CoFe (110) is shown in irradiated Ta(2)/CoFeB(1) samples. The mechanism of the different effects is discussed.

Chapter 4 demonstrates the domain wall dynamics of irradiated samples, which is very important for the application of domain-based racetrack memory. The results also show two completely different behaviors, consistent with the conclusion in Chapter 3. In order to figure out the contributions, the effective magnetic anisotropy K_{eff} is measured, and furthermore, the effects on the pinning density n_i are figured out.

Chapter 5 introduces the harmonic Hall measurements for investigating the effects on the spin-orbit torque (SOT) property Ta/CoFeB thin films, and the details and analysis method of the measurements are shown. Then, the results of SOT elucidate why and how the effects of He^+ ion irradiation are sensitive to the thickness of the Ta layer. Finally, we figured out that the Ta(3)/CoFeB(1) structure would be the best thickness as a candidate for device application.

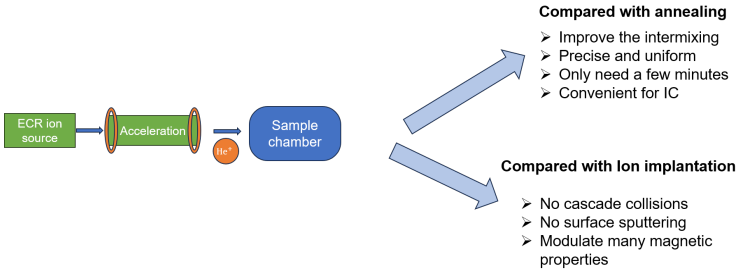

A: The schematic of He^+ ion irradiation technology.

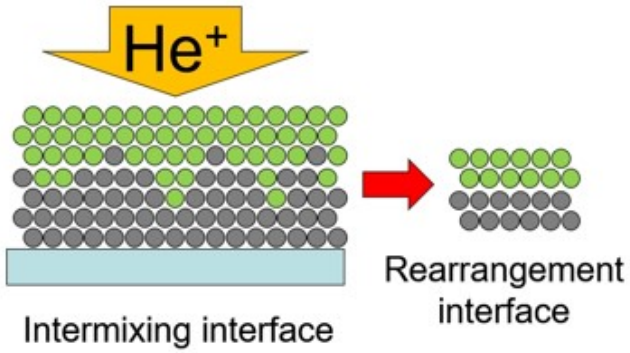

B: The intermixing interface is expected to be repaired.

FIGURE 1.4: (a) The schematic of He^+ ion irradiation technology and (b) expected effects.

Chapter 2

Sample Deposition and Device Fabrication

In this chapter, firstly, we show the details of the sample deposition and the stacks of the thin films(Section 2.1), as well as the method of sample characterization, including the crystallinity by X-ray diffraction measurements, and the perpendicular anisotropy property by magneto-optic Kerr effect (Section 2.2). Then, we describe the method and parameters of the Helium ion irradiation process (Section 2.3). Finally, we introduce the procedures and geometry of the device fabrication (Section 2.4).

2.1 Sample Deposition

The thin-film samples of Ta/CoFeB are deposited by RF magnetron sputtering. Sputtering is a common physical vapor deposition method for thin film with low deposition temperature, high deposition rate, and uniformity advantages. Under high vacuum, the incident Ar gas is ionized by a high voltage and then accelerated to bombard the target. The kinetic energy is transferred to target atoms because of the collision so that the target atoms can have enough kinetic energy to be ejected onto the substrate. A strong magnetic field is applied to focus the motion of ions to increase the sputtering efficiency.

The structure of samples is Subs./Ta(t)/$Co_{20}Fe_{60}B_{20}$(1)/MgO(2)/Ta(1), where the numbers or t in the brackets represent the thickness in nanometers. The stacks are shown as figure 2.1. The thickness t ranges from 2, 3, and 4 nanometers, and 5-nanometer samples are also deposited for reference. The 1-nm-thick Ta layer on the top of samples is the capping layer, avoiding oxidization. The Ta layer in the bottom is in an amorphous state. All the samples are deposited on $1 \times 1\,\mathrm{cm}^2$ size of common Si/SiO_2 substrates with thermal oxidization surface. Firstly, the bare substrates are cleaned with acetone and alcohol by 43 kHz ultrasonic for 5 mins to remove the dust. Then, the substrates are baked to remove the possible residue of alcohol. The cleaned substrates are then loaded onto a sample holder with nine slots, ensuring the samples with the same structure for different He^+ irradiation conditions are identical.

Next, after prevacuumizing, the holder with loaded samples is transferred into the main deposition chamber. The base pressure is lower than 10^{-5} Pa. When the pressure and temperature of the chamber are stable, the deposition is processed at room temperature. The sample stage with the holder is rotating at a constant speed for uniform deposition. For depositing the Ta layer, 15 sccm Ar gas flow is passed into the chamber, and the deposition pressure is held at 0.75 Pa. The power of the RF generator is set to 30 W. The detailed parameters of Ta and other layers are shown in Table 2.1. A movable shutter is covered between the target and samples stage,

and the thickness of the deposited layer is controlled through the time opening the shutter, depending on the deposition rate calibrated before. The CoFeB, MgO, and Ta capping layers are deposited subsequently on the Ta layer by the same processes with corresponding parameters.

After the deposition, the samples are annealed at 300 °C and high vacuum in the same chamber for obtaining perpendicular magnetic anisotropy (PMA). The magnetization of all samples is confirmed by Magneto-optic Kerr Effect (MOKE) measurements. The X-ray diffraction patterns are also checked in the next section to verify whether there is unexpected crystallization in the Ta and CoFeB layers.

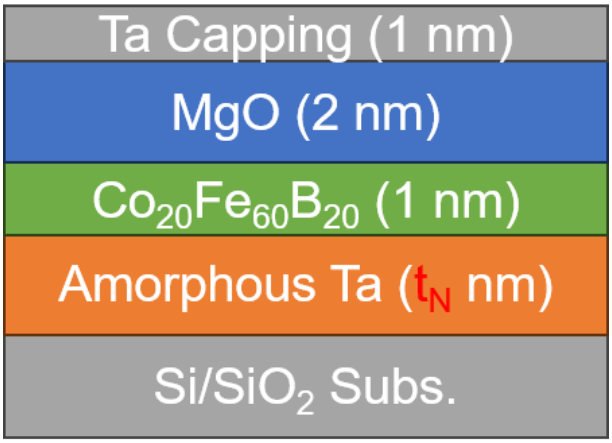

FIGURE 2.1: The stacks of Ta/CoFeB samples.

	Ta	CoFeB	MgO
Temperature	RT	RT	RT
Ar Flow (sccm)	15	15	15
Target Distance (mm)	100	100	100
Base Pressure (Pa)	$<10^{-5}$	$<10^{-5}$	$<10^{-5}$
Deposition Pressure (Pa)	0.75	0.27	0.7
Sputter Power (W)	30	40	50

TABLE 2.1: The deposition conditions for Ta/CoFeB/MgO thin-film.

2.2 Characterization

2.2.1 X-ray Diffraction Characterization

X-ray diffraction (XRD) measurements are processed on the samples after annealing to confirm whether there is unexpected crystallization because the annealing process at 300 °C is possible to give rise to the unexpected Ta(110) or Ta(111) crystallization[7, 8], which leads to disturbance in the subsequent analysis. The measurements are processed with a Rigaku SmartLab 9 kW machine, scanning from 20° to 120° of 2θ. In the case of the CoFeB layer, during the annealing process, the CoFe (001) crystallization is expected under the guidance of the MgO layer, leading to the interfacial perpendicular magnetic anisotropy (iPMA) from the formation of local bonding or hybridization between ferromagnetic and oxygen atoms. [9, 10] However, the (001) diffraction peak of the CoFe and MgO are unobservable in the XRD patterns since the bcc lattice structure, and the secondary (002) peak is too weak to be separated from the background signal. On the other hand, the crystallization of the CoFe (110) phase is also possible in the CoFeB layer that is not high-oriented during the annealing process[10, 11, 12], which is unexpected for the PMA property. The crystallization of the CoFe will be discussed again in Chapter 3.

The XRD patterns of pristine samples are shown in Figure 2.2. As the XRD patterns show, there is no characteristic peak of Ta and CoFe spotted in all the thickness of Ta(t_N)/CoFeB(1) samples, which means the Ta layer is still in amorphous status after the annealing process. And the possible crystallization of the unexpected CoFe (110) phase can be ignored.

2.2.2 Perpendicular Magnetic Anisotropy Characterization

When light is reflected from a magnetized surface, the polarization will change depending on the magnetization, called the Magneto-optic Kerr effect (MOKE). The magnetization of samples can be determined by measuring the change of the polarized

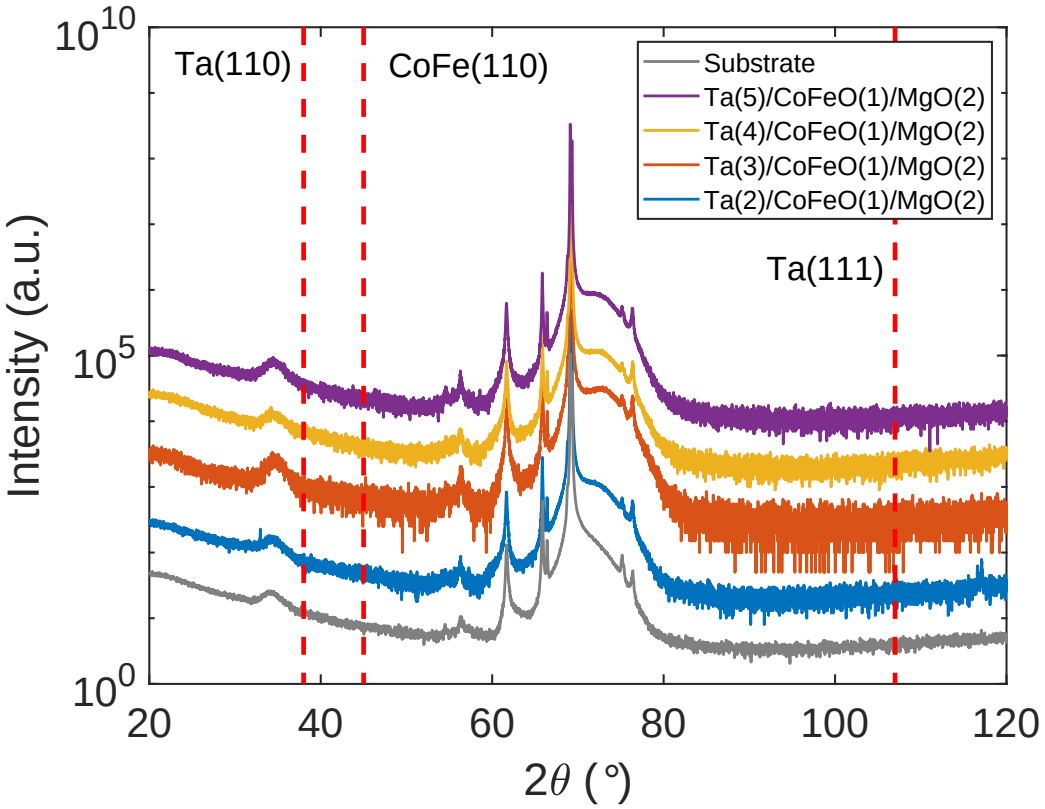

FIGURE 2.2: XRD patterns of pristine Ta/CoFeB/MgO samples.

The positions of characteristic peaks of Ta and CoFe are marked in the figure. The patterns are vertically shifted in order of the Ta thickness.

angle θ_k between the incident light and reflected light when an external magnetic field is applied. MOKE measurement is a very convenient method for quickly and qualitatively checking the magnetization. To confirm the magnetic anisotropy of our annealed samples, MOKE is measured under a sweeping magnetic field H_z that is perpendicular to the plane of samples, and the results of the polarized angle θ_k are shown in the figure 2.3. A square hysteresis loop appears in each curve, which is the signature of a suitable PMA property. θ_k goes to a constant stage when the magnetic field H_z over $\pm 50\,\mathrm{Oe}$, which means the magnetization is flipped up or down along with the H_z and saturated. The noise in the thinner samples is large due to the rough surface and environmental oscillation but enough to determine the PMA property.

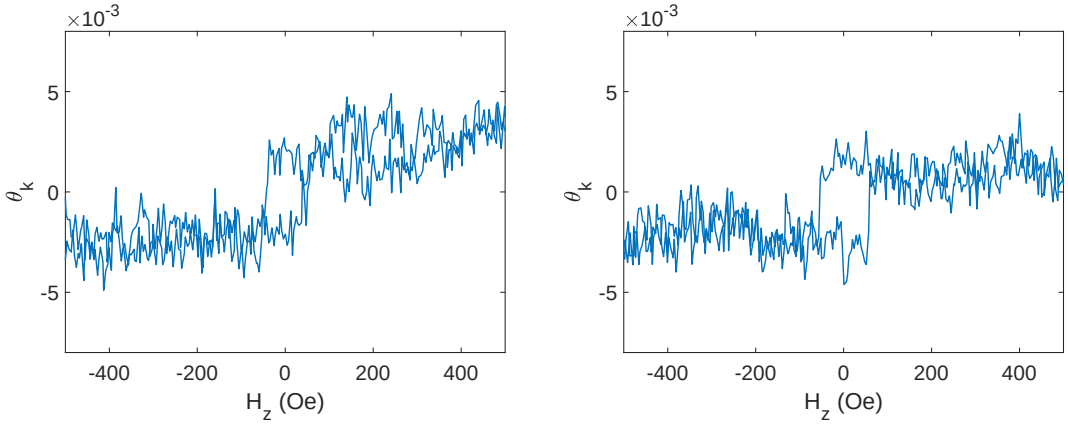

A: Ta(2)/CoFeB(1).

B: Ta(3)/CoFeB(1).

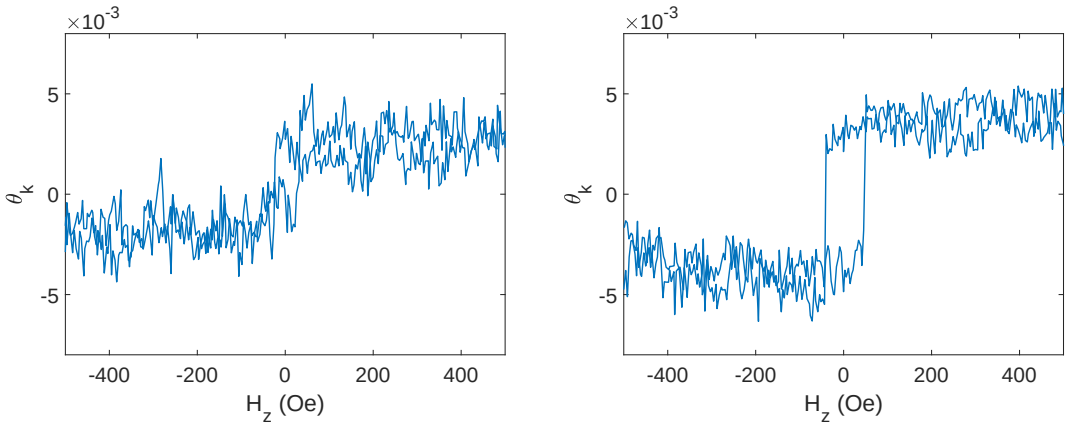

C: Ta(4)/CoFeB(1).

D: Ta(5)/CoFeB(1).

FIGURE 2.3: MOKE results of Ta(t_N)/CoFeB(1) pristine samples.

(a) Ta(2)/CoFeB(1). (b) Ta(2)/CoFeB(1). (c) Ta(2)/CoFeB(1). (d) Ta(2)/CoFeB(1).

2.3 Helium Ion Irradiation

The helium ion irradiation process is supported by Spin-Ion Technologies company and Dr. Dafiné Ravelosona's group and performed with a Helium-S facility as shown in figure 2.4. The working principles of the facility are shown in figure 2.5. The helium plasma is created in the electron cyclotron resonance (ECR) source by microwave radiation and helium gas. Then the ions are accelerated as an ion beam through a high electric field, where the voltage is set for the ion energy, and the amount of ions in the beam over a certain time is controlled by the ECR source. The ion beam subsequently goes through a filter, where the impurity ions and overly ionized ions will be removed. Finally, the pure helium ions beam will be focused and injected into the sample chamber, where the samples are bombarded at a certain angle. The different irradiation doses are linearly controlled by different irradiated times. The Helium-S facility is capable of creating a helium beam with energy from 1 to 30 keV to homogeneously irradiate a $15 \times 15\,\mathrm{mm}^2$ area, therefore multiple samples of different thicknesses with the same irradiation dose can be irradiated in the same time for ensuring the same irradiation effects.

The samples are irradiated by Helium ions with an energy of 15 keV, the irradiation doses (fluence) in $10^{14}\,\mathrm{ions/cm}^2$ ranged in 0 (pristine), 4, 6, 8, 10, 12, 14 for Ta(2)/CoFeB(1) and 0 (pristine), 4, 6, 10 for Ta(3,4)/CoFeB(1) samples. All samples are confirmed to show a good PMA property after the annealing process before the irradiation process.

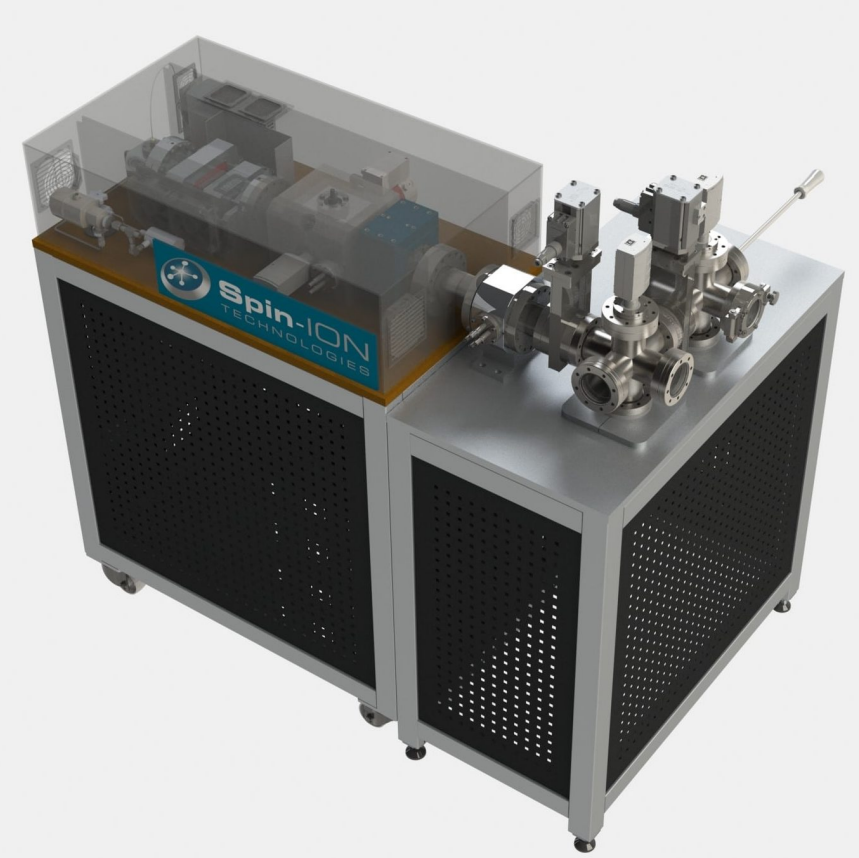

FIGURE 2.4: Helium-S facility for Helium ion irradiation.[13]

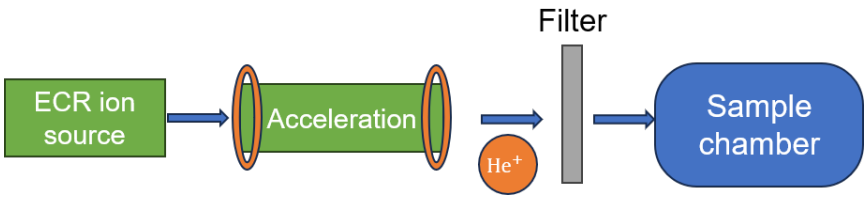

FIGURE 2.5: The working principles of the Helium-S facility for irradiation.

2.4 Device Fabrication

In order to perform electrical transport measurements for properties such as effective anisotropy K_e and spin-orbit torque, samples are fabricated into devices, or Hall bars in this work, after finishing the measurements with original thin films. The fabrication uses ordinary 2-step photolithography to pattern the devices and Ar ion milling to etch the patterns.

Firstly, the samples are smoothly cleaned by 23 kHz ultrasonic in alcohol for 1 min to remove the dust and dirty things from previous measurements. Then, the positive photoresist S1813 is covered on the film by spin-coating. The parameters of spin-coating are in 5000 RPM spin speed for 60 s. The thickness of the photoresist coating is supposed to be around 1.3 μm according to the recipe.[14] The coated samples are pre-baked at 115 °C for 60 s on a hotplate.

Subsequently, the first step of photolithography for Hall bar patterns is performed. A mask with patterns of Hall bars is aligned on the samples by a contact optical aligner and exposed to UV light for 9.7 s. The width and length of the measuring area are 10 μm and 25 μm, respectively. The geometry is shown in figure 2.6. Then the exposed samples are smoothly developed in developer for around 40 s until the patterns are clear as figure 2.7, the coating of the unpatterned region is cleaned.

Then, the samples are placed into an Ar ion milling machine for etching at a high vacuum level in the order of 10^{-5} Pa. An accelerated Ar ion beam is created to etch the samples, and the region without photoresist coating is etched. When the etching process is completed, the samples are taken out from the chamber to clean in acetone with 23 kHz ultrasonic for 1 min to remove the residue of photoresis smoothly. The resistivity of the unpatterned region is simply checked to ensure the film is wholly etched over the depth of the substrate.

The second step of photolithography is for the patterns of the electrodes of the Hall bar. The procedures are similar to the first step. The cleaned samples are immediately spin-coated with the photoresist again to prevent possible oxidization. The region

of electrodes is exposed for 13.5 s and developed to remove the photoresist on those areas. The 2-step photolithography is completed now.

After the photolithography process, samples are transferred into an EB-Evaporator machine for electron-beam physical vapor deposition. 10 nm Ti and 100 nm Au film are deposited as the electrodes at the vacuum around 10^{-6} Torr. Finally, the samples are cleaned in acetone and alcohol again for 1 min to remove the residue of the photoresist and the undesired region of Ti/Au, respectively. The whole flow of the sample preparation is shown in figure 2.8.

2.5 Conclusion

In this chapter, we demonstrate the methods used for sample deposition, characterization, He^+ irradiation process, and device fabrication. The basic structure of the facility setups is explained with images. The details are introduced in each corresponding section, and the parameters, such as the deposition conditions, irradiation energy, and the geometry of devices, are listed for reproducibility.

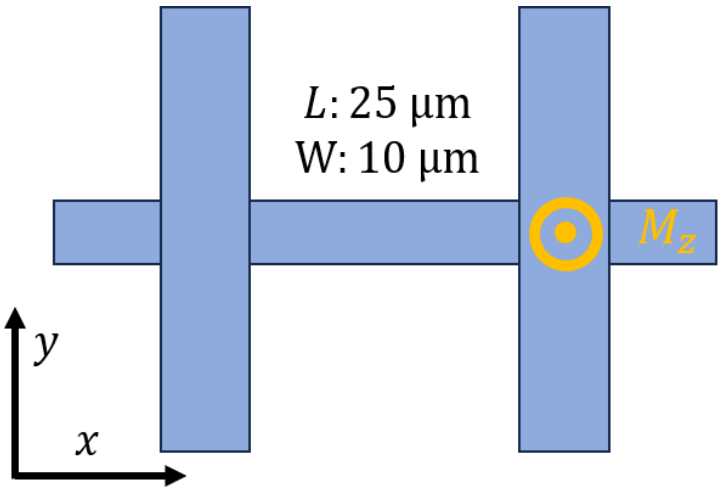

FIGURE 2.6: The geometry of the Hall bar device

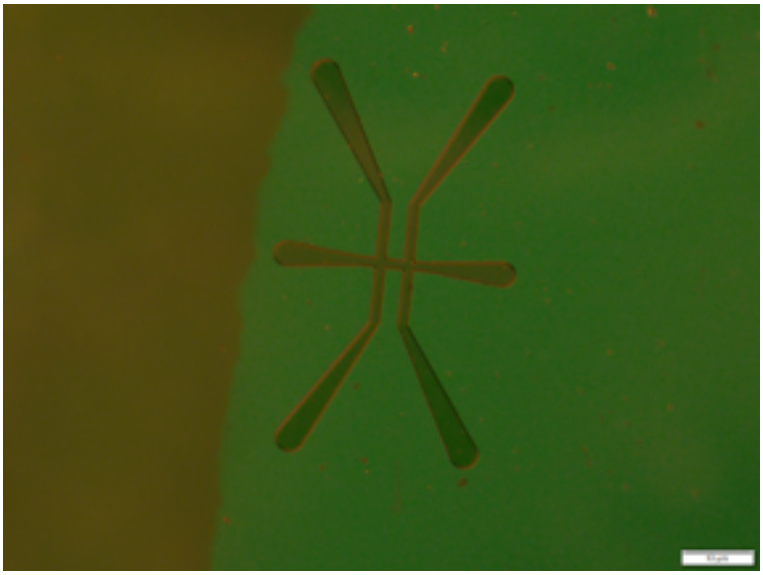

FIGURE 2.7: The optical image of the Hall bar device

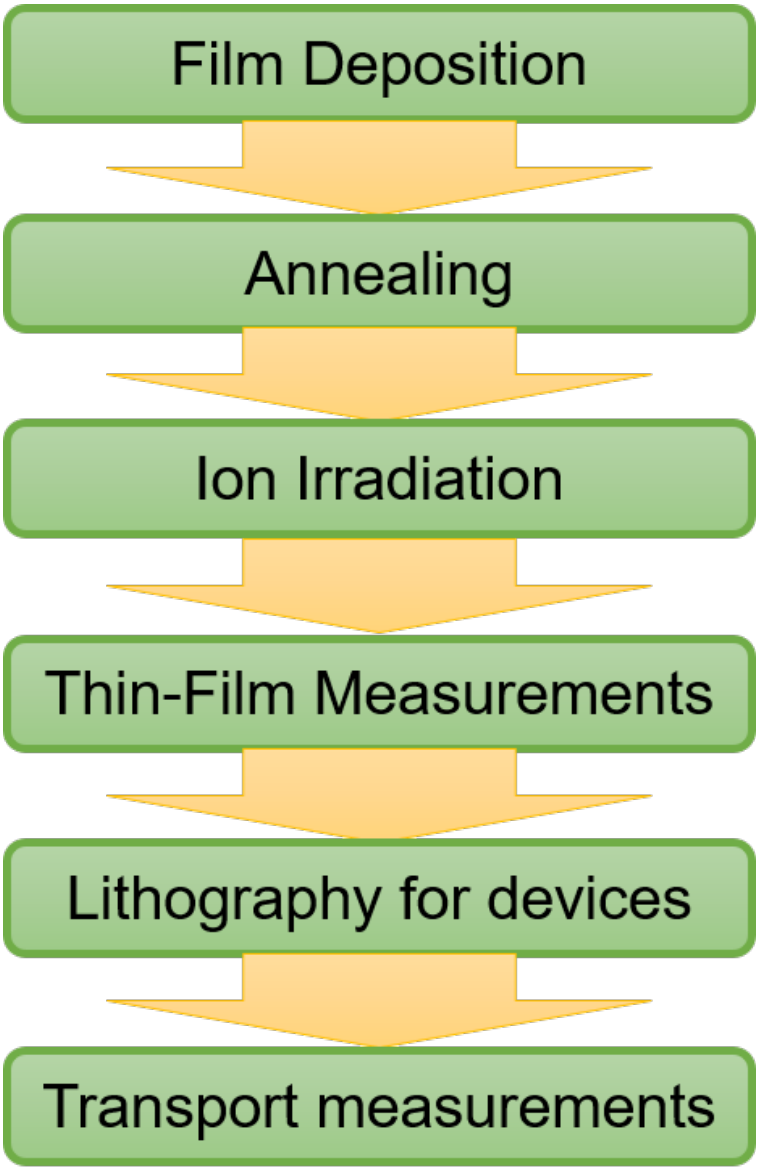

FIGURE 2.8: The diagram of the whole flow of sample preparation, including deposition and device fabrication.

Chapter 3

The Effect of He^+ Irradiation on the Magnetic Property

In this chapter, we present how the He^+ ion irradiation modifies the magnetic property of Ta/CoFeB thin films, especially the m_s in section 3.1. We found the m_s of Ta(2)/CoFeB(1) is significantly affected by irradiation, showing a significant difference from the other group of Ta(3,4)/CoFeB(1). In order to figure out its origin, we performed the XRD measurements on all irradiated samples and, for the first time, found the increased crystallization of the CoFe (110) phase by irradiation, and subsequently confirmed by STEM images. According to the mechanism of He^+ ion irradiation, we discussed how the irradiation modifies the crystallinity and the m_s.

3.1 The Effect of He^+ Irradiation on Saturation Magnetization m_s

3.1.1 Vibrating-sample Magnetometry (VSM) of Thin Films

In order to investigate the effect of He^+ irradiation on saturation magnetization m_s, VSM measurements are performed with the bare films and irradiated films. VSM is an instrument to measure materials' magnetic properties by measuring a magnetic field's magnitude and direction. The feasible samples are flexible, including solids, powders, single crystals, thin films, and liquids,[15]. Therefore, the large-size samples can be measured non-destructively to extract the small signal.

The schematic of a typical VSM facility is shown in figure 3.1. The sample, in the form of thin film on a Si substrate with $5 \times 10\,\mathrm{mm}^2$ size, is vertically mounted on the end of the sample holder, which is fixed in a specific position for the uniform magnetic field from an electromagnet, and the direction of the magnetic field is in perpendicular to the plain of samples along with the easy axis of PMA samples. A motor drives the sample holder to vibrate along the z-axis when measuring. Pickup coils surround the sample holder to pick up the signals by Faraday's law of induction from the magnetization change from vibrating samples.

3.1.2 The Magnetization of Irradiated Ta/CoFeB Thin films

In the process of Helium irradiation, the samples are cut into $5 \times 10\,\mathrm{mm}^2$ size for each irradiation dose for convenience. In the measurement of VSM, because the detected signal from samples is the total magnetization M_s, which depends on the size of each sample, we need to calculate the magnetization per volume m_s by $m_s = M_s/(S \times t_F)$, where S is the size of thin films, and t_F is the thickness of the ferromagnetic CoFeB layer. The accurate size of each sample is determined by optical photo as shown in figure 3.2, where the accurate number of pixels is read by ImageJ software and converted to practical millimeters. The uncoating area in the corner is excluded in the calculation to reduce error because of the cover of the sample holder in sputtering deposition.

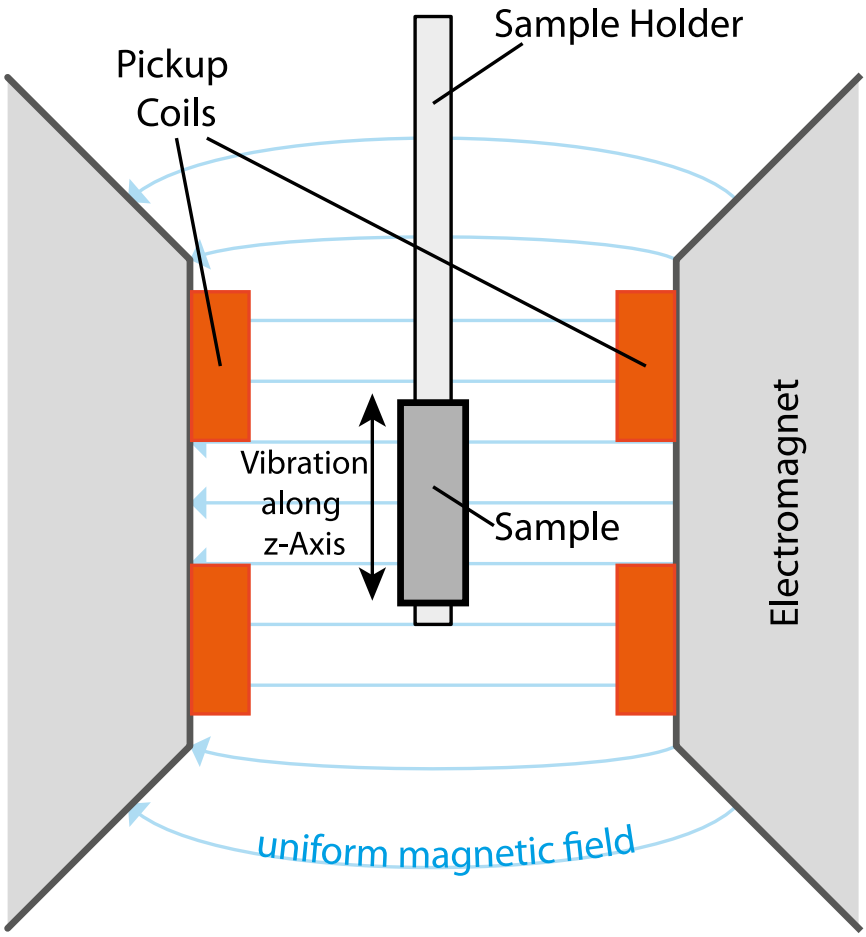

FIGURE 3.1: The schematic of a typical VSM facility.[16]

In the case of the thicker samples Ta(3,4)/CoFeB(1), the magnetization m of the pristine sample and samples with irradiation doses $(4, 6, 10) \times 10^{14}\,\mathrm{He}^+/\mathrm{cm}^2$ are measured as shown in the figure 3.3 for $3\,\mathrm{nm}$ and figure 3.4 for $4\,\mathrm{nm}$. The length of steps of scanning external magnetic field H_z around zero is shortened to show the hysteresis loop of m clearer. In general, all the Ta(3,4)/CoFeB(1) samples keep PMA property after irradiation, and the squareness of M-H loops is still good. The figure 3.5 a and 3.5 b show the m_s and h_c extracted from the results. The m_s keeps a value that is almost constant in 3 and 4 nm samples, which indicates the stable magnetic property of thicker Ta/CoFeB(1) thin films. Stable m_s values are important for the thermal stability of the spintronic device applications. The coercive field h_c of both thicknesses shows a similar behavior as shown in figure 3.5 b, decreasing firstly in the lower doses and increasing again in the high dose $10 \times 10^{14}\,\mathrm{He}^+/\mathrm{cm}^2$. The coercive field h_c indicates the intensity of the external field that is just strong enough to switch the magnetization direction. The intensity of h_c is proportional to the magnetic anisotropy and pining of materials. The decrease in lower doses is as expected because certain doses of He ion irradiation can rearrange the atoms gently and cause mixing and alloying, in which the decrease of h_c is attributed to the cause of the reduction in anisotropy.[17, 18] However, when the irradiation is too high, too many defects or vacancies are created in the film, playing a role as the pinning centers, which increase the coercivity again.

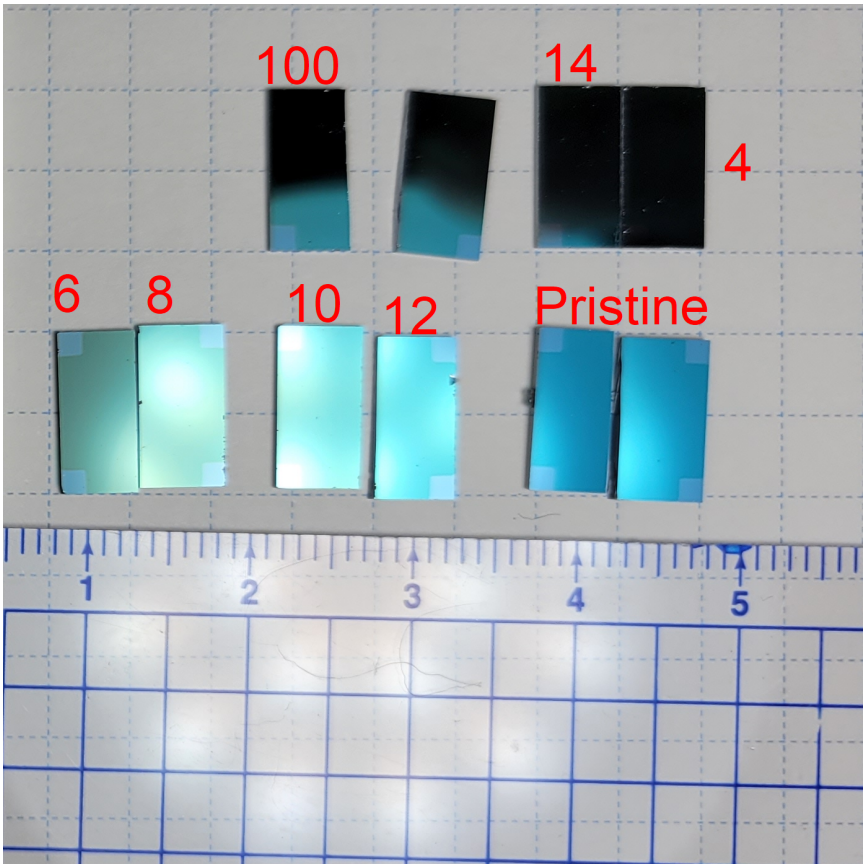

FIGURE 3.2: The Ta(2)/CoFeB(1) samples irradiated with different doses.

Red numbers indicate the doses in $= 10^{14}\,\mathrm{He}^+/\mathrm{cm}^2$. The accurate size of each sample is read by software from the photo. Other Ta(t_N)/CoFeB(1) samples are treated similarly.

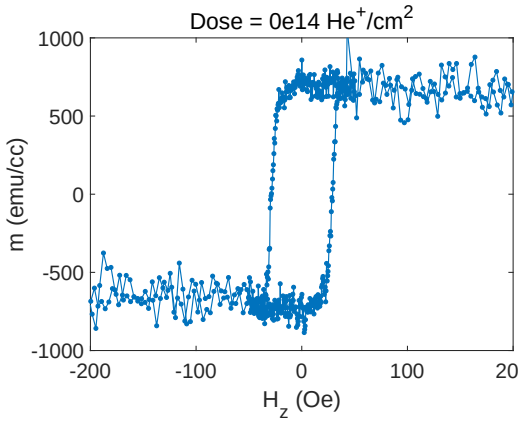

A: Pristine.

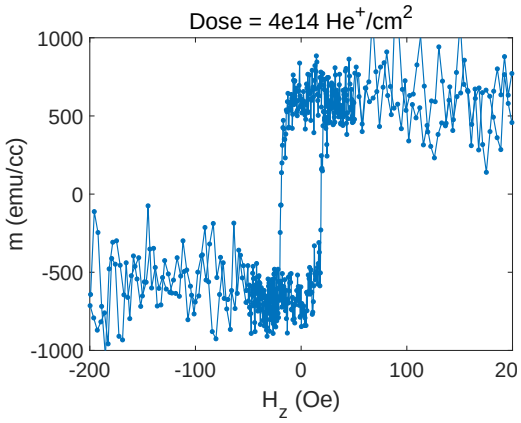

B: Irradiation dose $= 4 \times 10^{14}\,\mathrm{He}^+/\mathrm{cm}^2$.

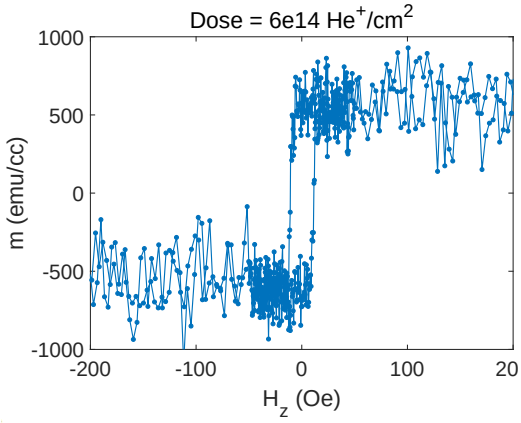

C: Irradiation dose $= 6 \times 10^{14}\,\mathrm{He}^+/\mathrm{cm}^2$.

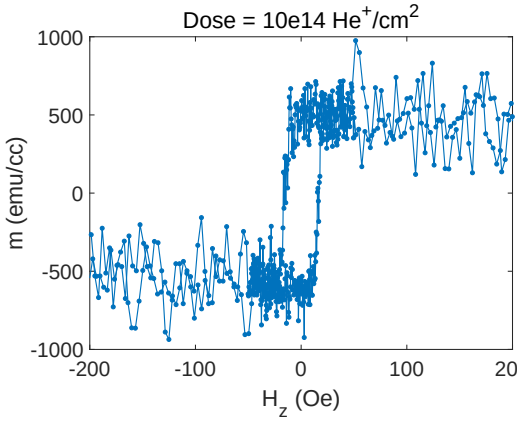

D: Irradiation dose $= 10 \times 10^{14}\,\mathrm{He}^+/\mathrm{cm}^2$.

FIGURE 3.3: The magnetization of Ta(3)/CoFeB(1) samples from VSM measuremens.

(a) Pristine sample. Irradiation dose = (b)$4 \times 10^{14}\,\mathrm{He}^+/\mathrm{cm}^2$. (c) $6 \times 10^{14}\,\mathrm{He}^+/\mathrm{cm}^2$. (d) $10 \times 10^{14}\,\mathrm{He}^+/\mathrm{cm}^2$.

In the case of Ta(2)/CoFeB(1), the magnetizaiton m of the pristine sample and samples with irradiation doses $(4, 6, 8, 10, 12) \times 10^{14}\,\mathrm{He}^+/\mathrm{cm}^2$ are measured as shown in the figure 3.6. The length of steps of scanning the external magnetic field H_z around zero is also shortened, as in the cases of thicker samples. In consistence of the results of MOKE in figure 2.3, all the samples, including the irradiated samples, are still in PMA property, which means the irradiation doses are not too high to significantly change the type of magnetic anisotropy as reported in Ref. [19, 20, 21, 22]. The extracted saturation magnetization m_s and the coercive field h_c are plotted depending on the irradiation dose as figure 3.7 a and b for showing the effect of irradiation visually, respectively.

Although all the Ta(2)/CoFeB(1) samples keep a good PMA, the m_s in figure 3.7 a shows a strong modulation from the He ion irradiation, which is very different from the case of thicker Ta(3,4)/CoFeB(1) samples. In the lower doses $(4 - 8 \times 10^{14}\,\mathrm{He}^+/\mathrm{cm}^2)$, the m_s is increased from $508\,\mathrm{emu/cc}$ until $647\,\mathrm{emu/cc}$, which is the 1.3 time of the pristine sample. In the higher doses $(> 8 \times 10^{14}\,\mathrm{He}^+/\mathrm{cm}^2)$, the m_s decreases again from $647\,\mathrm{emu/cc}$ to around $535\,\mathrm{emu/cc}$, showing a non-monotonic effect as reported [23, 24]. However, the h_c in figure 3.7 b also shows a non-monotonic effect that increases firstly and decreases subsequently, in the opposite of the expected decreasing tendency. [21, 23, 24, 25, 26] The opposite tendency of h_c suggests the different effects of He ion irradiation on the magnetic properties, and the same modulation with the m_s suggests their possible same origin. Because the relationship between the coercive field and materials properties is usually complicated, it's also easy to be impacted by extrinsic properties like roughness.[18] Therefore, more measurements directly on the material properties are necessary to figure out the nature, which will discussed in the next section and next chapter.

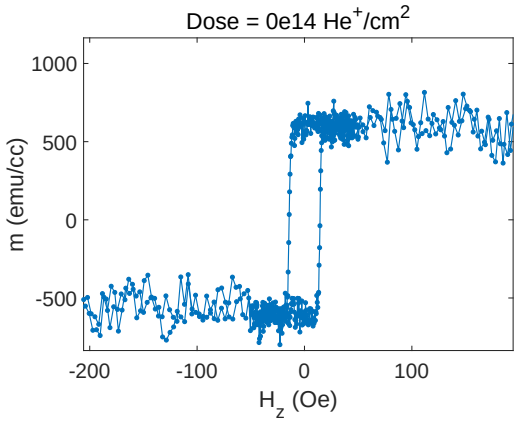

A: Pristine.

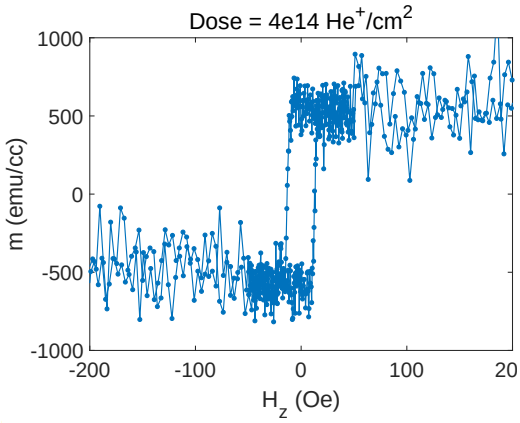

B: Irradiation dose $= 4 \times 10^{14}\,\mathrm{He}^+/\mathrm{cm}^2$.

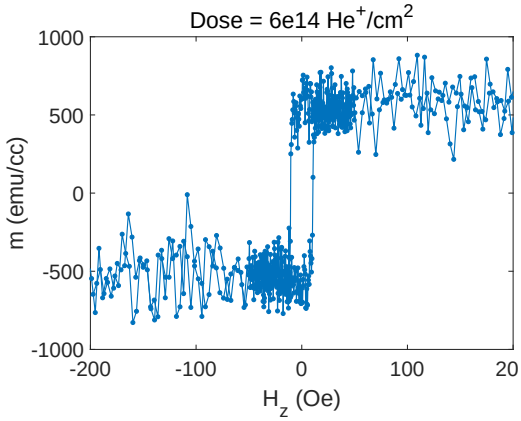

C: Irradiation dose $= 6 \times 10^{14}\,\mathrm{He}^+/\mathrm{cm}^2$.

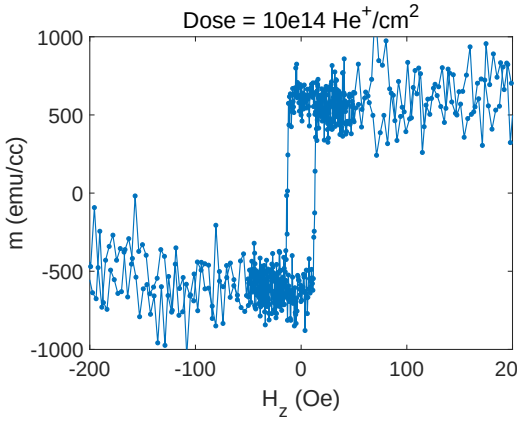

D: Irradiation dose $= 10 \times 10^{14}\,\mathrm{He}^+/\mathrm{cm}^2$.

FIGURE 3.4: The magnetization of Ta(4)/CoFeB(1) samples from VSM measuremens.

(a) Pristine sample. Irradiation dose = (b)$4 \times 10^{14}\,\mathrm{He}^+/\mathrm{cm}^2$. (c) $6 \times 10^{14}\,\mathrm{He}^+/\mathrm{cm}^2$. (d) $10 \times 10^{14}\,\mathrm{He}^+/\mathrm{cm}^2$.

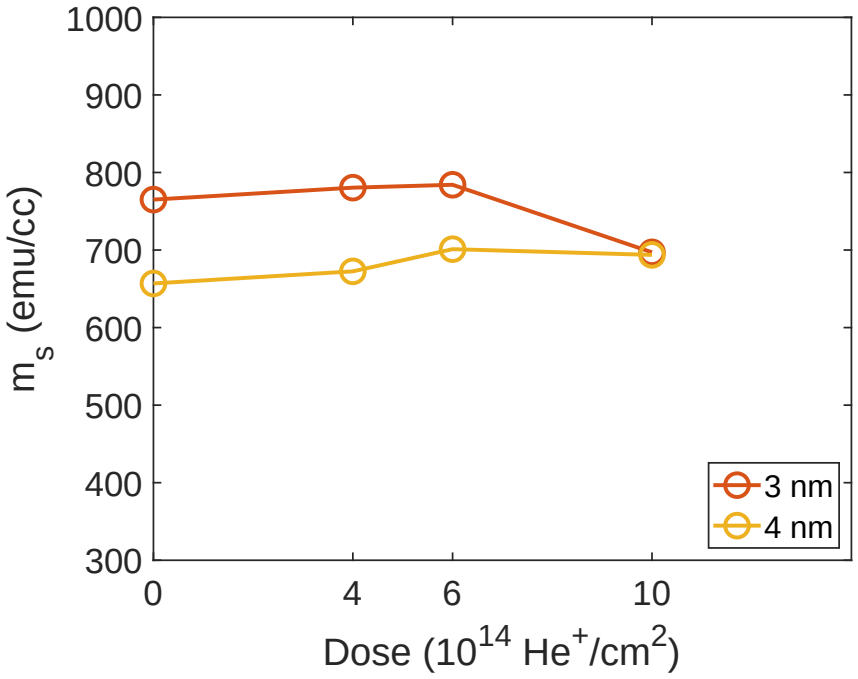

A: The saturation magnetization m_s of Ta(2)/CoFeB(1).

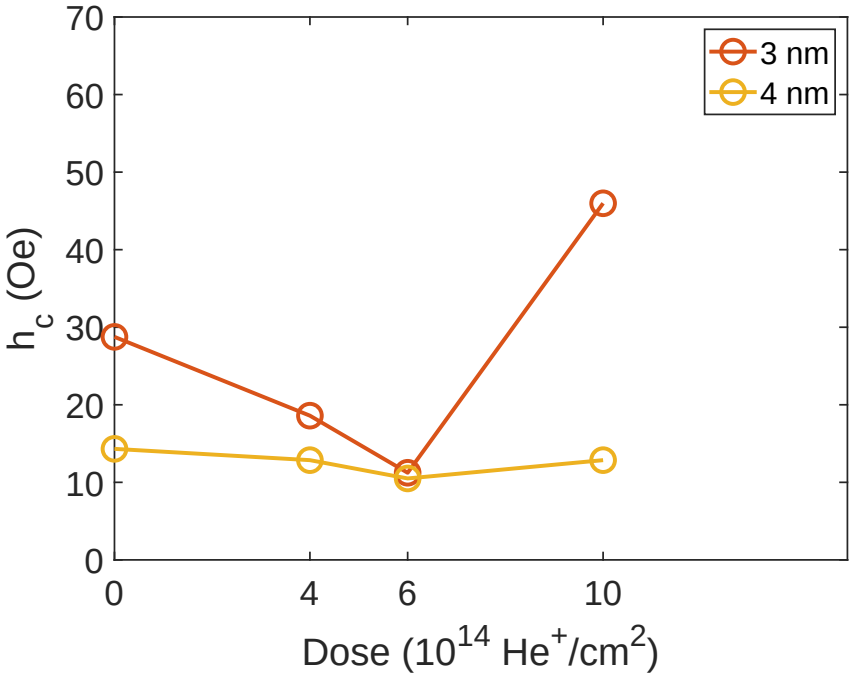

B: The coercive field h_c of Ta(2)/CoFeB(1).

FIGURE 3.5: The magnetic properties m_s and h_c of Ta(3,4)/CoFeB(1).

In summary, the M-H loop results of irradiated Ta(t_N)/CoFeB(1) samples show very different behavior between the thicker and thinner samples. It's convenient to separate them into two groups, the thicker Ta(3,4)/CoFeB(1) samples and the thinner Ta(2)/CoFeB(1) samples, to investigate the properties and the physical nature behind the difference. In the group of thicker samples, the m_s keeps constant, and the coercive field h_c decreases in the lower doses, which are advantages for the device application. In the group of thinner samples, the m_s and h_c show a significant modulation from the irradiation doses, suggesting the different effects behind them, requiring more investigation.

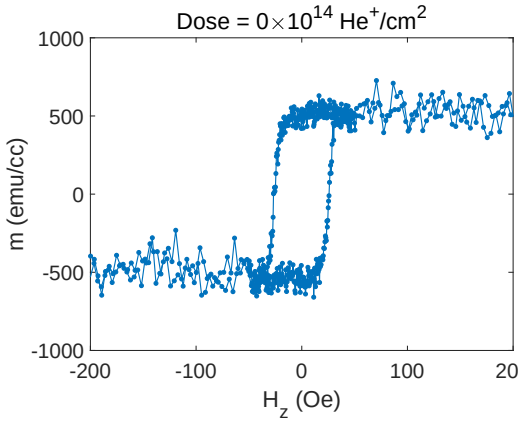

A: Pristine.

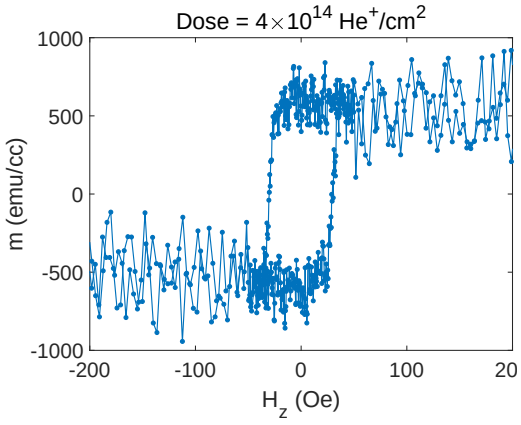

B: Irradiation dose $= 4 \times 10^{14}\,\mathrm{He}^+/\mathrm{cm}^2$.

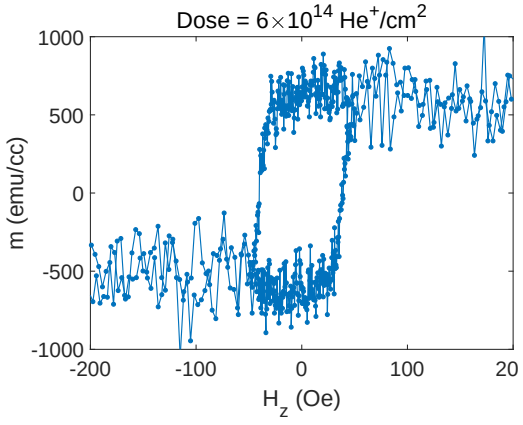

C: Irradiation dose $= 6 \times 10^{14}\,\mathrm{He}^+/\mathrm{cm}^2$.

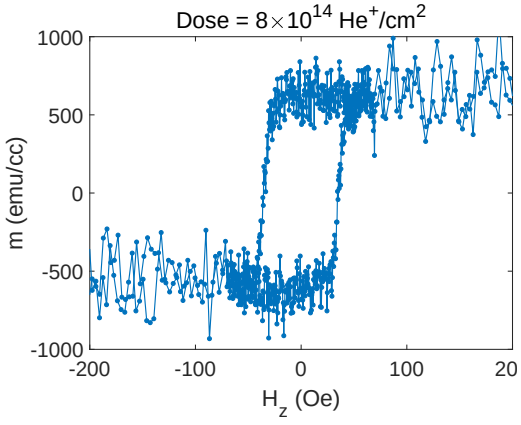

D: Irradiation dose $= 8 \times 10^{14}\,\mathrm{He}^+/\mathrm{cm}^2$.

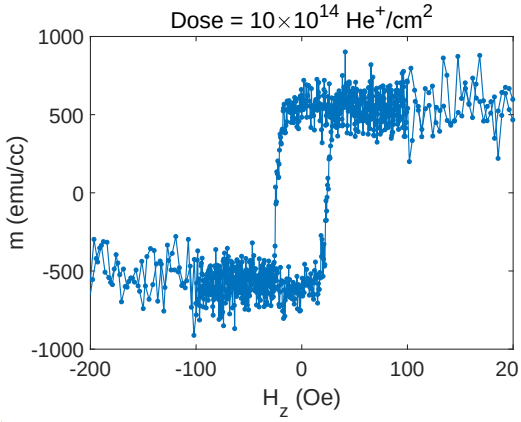

E: Irradiation dose $= 10 \times 10^{14}\,\mathrm{He}^+/\mathrm{cm}^2$.

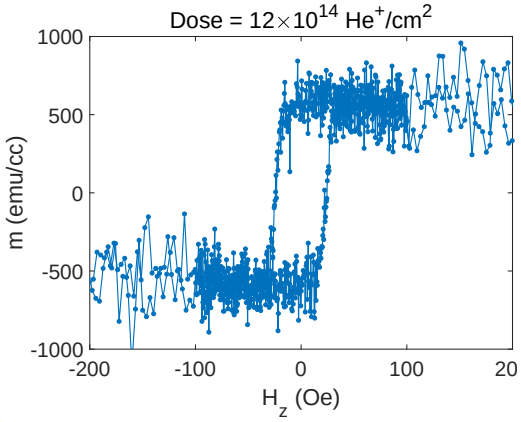

F: Irradiation dose $= 12 \times 10^{14}\,\mathrm{He}^+/\mathrm{cm}^2$.

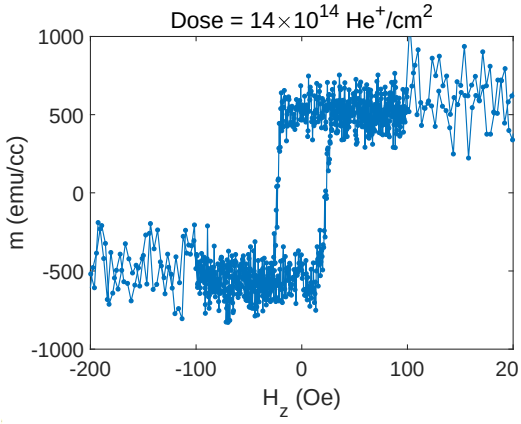

G: Irradiation dose $= 14 \times 10^{14}\,\mathrm{He}^+/\mathrm{cm}^2$.

FIGURE 3.6: The magnetization of Ta(2)/CoFeB(1) samples from VSM measuremens.

(a) Pristine sample. Irradiation dose $=$ (b)$4 \times 10^{14}\,\mathrm{He}^+/\mathrm{cm}^2$. (c) $6 \times 10^{14}\,\mathrm{He}^+/\mathrm{cm}^2$. (d) $8 \times 10^{14}\,\mathrm{He}^+/\mathrm{cm}^2$. (e) $10 \times 10^{14}\,\mathrm{He}^+/\mathrm{cm}^2$. (f) $12 \times 10^{14}\,\mathrm{He}^+/\mathrm{cm}^2$. (g) $14 \times 10^{14}\,\mathrm{He}^+/\mathrm{cm}^2$.

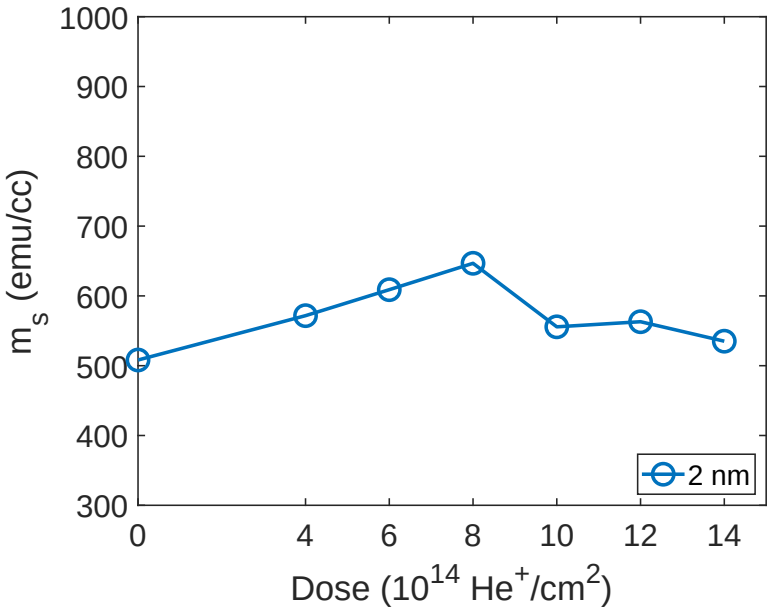

A: The saturation magnetization m_s of Ta(2)/CoFeB(1).

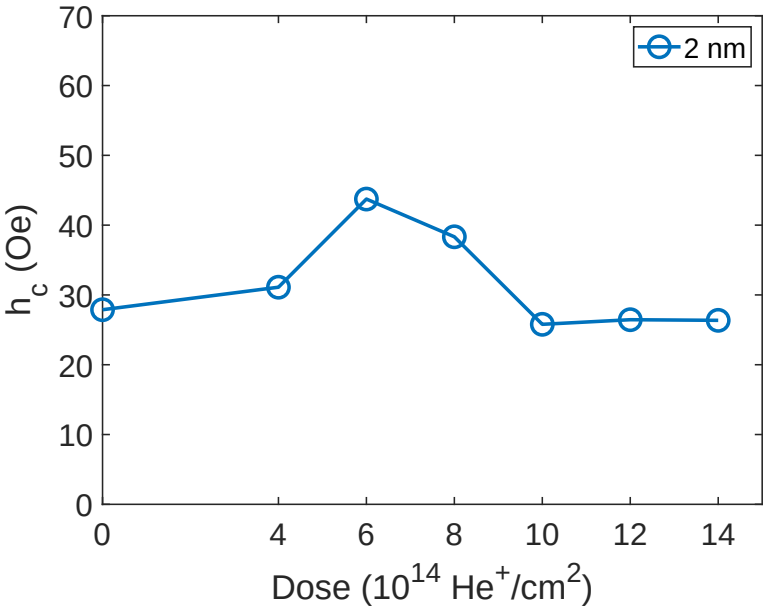

B: The coercive field h_c of Ta(2)/CoFeB(1).

FIGURE 3.7: The magnetic properties m_s and h_c of Ta(2)/CoFeB(1).

3.2 The XRD Patterns and the Crystallization of Ta/CoFeB Samples

In the last section, the magnetic properties of irradiated Ta/CoFeB samples from VSM measurements are discussed. The samples are separated into two groups depending on the thicker or thinner thickness of the Ta layer, and the thinner Ta(2)/CoFeB group shows a peculiar tendency on both m_s and h_c. The possible crystallization in the ferromagnetic layer is a reasonable candidate because the crystallization can change the m_s and h_c simultaneously, and the increasing grain boundary can explain the increase of coercivity. The possibility of crystallization of CoFe from He ion irradiation is reasonable because of the rearrangement of atoms.

However, although some previous studies mentioned the existence of crystallization increased by He ion irradiation[25, 23, 27, 20, 24], only indirect evidence of effective magnetic anisotropy K_{eff}, the redistribution of atoms, m_s, and h_c are raised, the direct evidence especially like XRD characteristic peaks have lacked. That's because the signal of the crystallization in the CoFeB layer is very weak due to the ultra-thin thickness (around 1 nm in usual cases) in PMA samples and the incomplete crystallization of CoFe.

3.2.1 The Crystallization in Ta(2)/CoFeB(1) Samples

Here, we use the Rigaku SmartLab 9 kW machine to process the XRD measurements on irradiated Ta/CoFeB samples, which offer much higher resolution. Since the anomalous tendency of m_s and h_c, we firstly focus on the XRD patterns of Ta(2)/CoFeB(1) samples, the general view of the complete range of 2θ are shown in figure 3.8, where there are no significant peaks shown compared with the pattern of the substrate. It notes that the y-axis is in a logarithm here to show the whole profile clearly. As for showing the effect of crystallization, a sample is irradiated by a much

higher dose $100 \times 10^{14}\,He^+/cm^2$ and measured by the same procedures. Nonetheless, if we zoom in on the patterns in a common axis until close to the background as figure 3.9, the XRD characteristic peak of CoFe (110) can be spotted. Although the intensity of the characteristic peak is very low, just about 10% higher than the background, it's clear to see the appearance of the peak in the samples irradiated by doses from $4 \times 10^{14}\,He^+/cm^2$ to $12 \times 10^{14}\,He^+/cm^2$. In the samples irradiated by higher doses, the characteristic peak of CoFe (110) is with a significantly stronger intensity, indicating a clear dose-dependent tendency, which means the signal of the characteristic peak is not from the background noise.

In the PMA Ta/CoFeB thin films, the CoFe (001) phase should crystallize in the CoFeB layer with a certain thickness and guidance of the MgO layer after the annealing process, leading to the out-of-plane easy axis along with (001), and the Boron atoms are mostly diffused into other adjacent layers.[9] However, the Crystal of CoFe is in a bcc lattice, where the diffraction peak of (001) is canceled. The simulated XRD patterns are as shown in figure 3.10, where the 2θ ranging from 20° to 120°. Compared with the measured results in figure 3.8 and simulated patterns, only the small signal of the characteristic peak of CoFe (110) can be spotted. Since the good PMA property is already confirmed for all irradiated samples in figure 3.6 of the previous section, we can confirm that the CoFe(001) is the main phase of the CoFeB layer, and the CoFe (110) is secondary created after He ion irradiation.

For quantitatively analyzing the increase of crystallization, the integrated intensity of this characteristic peak is extracted. Using profile shape functions to fit measured XRD patterns is a proper quantitative analysis method. In this work, the raw data is fitted by the LIPRAS[28], which is software for line-profile analysis based on MATLAB. The background signal of each sample is modeled by polynomial and removed for the very small or overlapped signal, then the line profile of only the peak is fitted by the pseudo-Voigt function.

The extracted results of the integrated intensity N are shown in figure 3.11. The integrated intensity of the pristine Ta(2)/CoFeB(1) sample is close to 0, indicating

negligible CoFe (110) crystallization before irradiation. After being irradiated with the dose of $4 \times 10^{14}\,\mathrm{He^+/cm^2}$ to $8 \times 10^{14}\,\mathrm{He^+/cm^2}$, the component of CoFe (110) phase increases quickly until the dose $8 \times 10^{14}\,\mathrm{He^+/cm^2}$, and then slightly decrease. Finally, in the very high doses $14 \times 10^{14}\,\mathrm{He^+/cm^2}$ and $100 \times 10^{14}\,\mathrm{He^+/cm^2}$, the component of CoFe (110) phase are almost double, indicating the much higher crystallization.

Compared with the modulation of m_s in figure 3.7 a, it's easy to find that the m_s changed in the same way of the crystallization of CoFe (110) phase in the range of doses $0 \times 10^{14}\,\mathrm{He^+/cm^2}$ to $12 \times 10^{14}\,\mathrm{He^+/cm^2}$, and the value of m_s is increased to the level of thicker Ta(3,4)/CoFeB(1) samples. It's reasonable to consider that the lower doses of He ion irradiation promoted the crystallization of CoFe, increasing the m_s of it. During this process, the crystallinity of the CoFe (110) phase is also promoted, and the promoted new phase leads to the increase of both m_s and h_c.

To further confirm the promoted crystallization in the CoFeB layer, the Scanning Transmission Electron Microscope (STEM) measurements are used to observe the lattice of Ta(2)/CoFeB(1) samples. The pristine sample and the sample with the dose $10 \times 10^{14}\,\mathrm{He}^{+}/\mathrm{cm}^2$ are measured as figure 3.12.

In figure 3.12 a, the crystallinity of the CoFeB layer and MgO layer, as marked by the red dotted lines is not very high, and their directions are not matched totally. The Fast Fourier Transform (FFT) image is shown in the top left corner. Due to the same reason as the XRD patterns, the characteristic spot of CoFe(001) is in cancellation, so there is only a very blurred polycrystalline ring shown in the FFT image, which is attributed to the tiny amount of CoFe (110) phase generated in the annealing process. In figure 3.12 b, the crystallinity of the CoFeB layer and MgO layer is obviously higher than the pristine sample in figure 3.12 a, and the FFT image of an identical size of the transferred area shows an apparent polycrystalline ring, which is the clear evidence of the crystallization of CoFe (110) phase. Different from the well-oriented CoFe (001) phase, the crystallization of CoFe (110) is polycrystalline and random-oriented, which leads to the increase of h_c.

The integrated intensity of the CoFe (110) component in figure 3.11 keeps increasing and almost doubled in the doses higher than $12 \times 10^{14}\,\mathrm{He}^{+}/\mathrm{cm}^2$. However, the m_s in figure 3.7 a decreases in the high doses, which can not be explained by the crystallization of CoFe (110). That's because only the crystallinity of CoFe (110) can be quantitatively measured, but not that of CoFe (001), which is the main contribution to the m_s. According to the physics of He ion irradiation, in the lower doses, the collision of atoms with He ions or the secondary scattered atoms creates Frenkel pairs, and most of the vacancies are unstable and soon recombined because of the very short displacement of atoms. Therefore, the apparent effect is rearranging the atoms and improving the crystallization. In the case of high doses, the accumulation of stable Frenkel pairs remains in more and more vacancies and interstitial atoms. Consequently, the crystal is destroyed. The mechanism will be discussed in the following subsection.

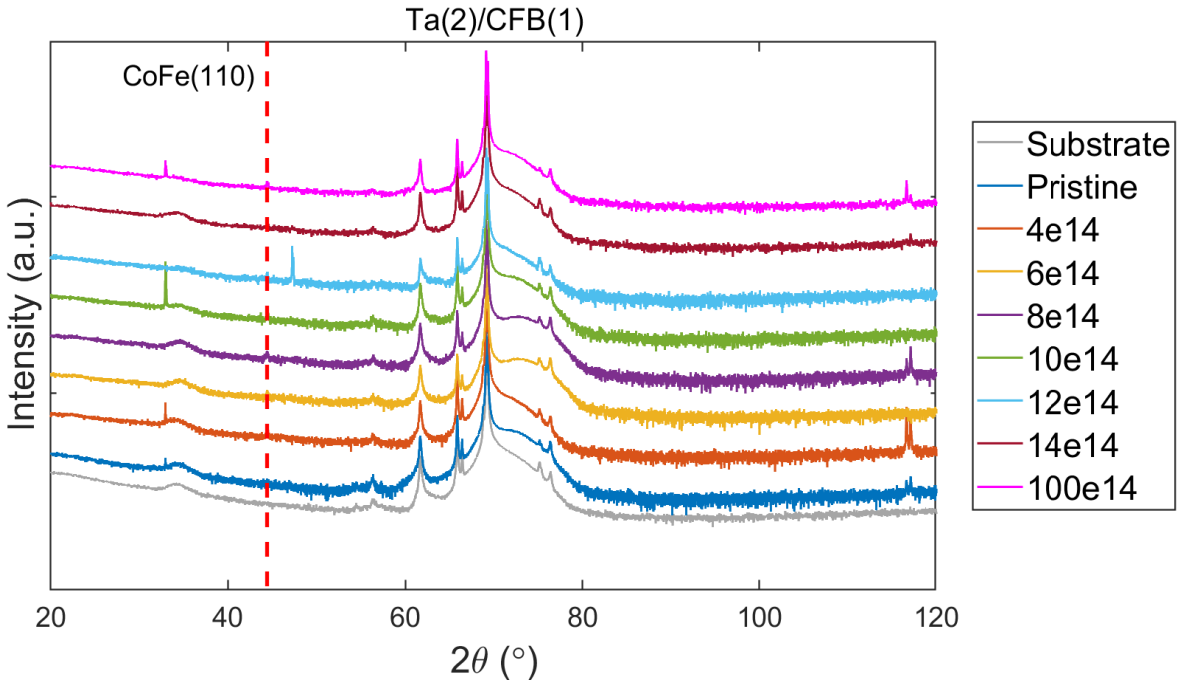

FIGURE 3.8: The XRD patterns of Ta(2)/CoFeB(1) samples irradiated with different doses.

The y-axis is in logarithm. The patterns are vertically shifted in order of the doses from the bottom to the top. The pattern of the Si substrate is shown at the bottom for reference. The position of the peak of CoFe (110) is marked with a red dotted line. The signal is too weak to be spotted in the common axis due to the stretch of background signals.

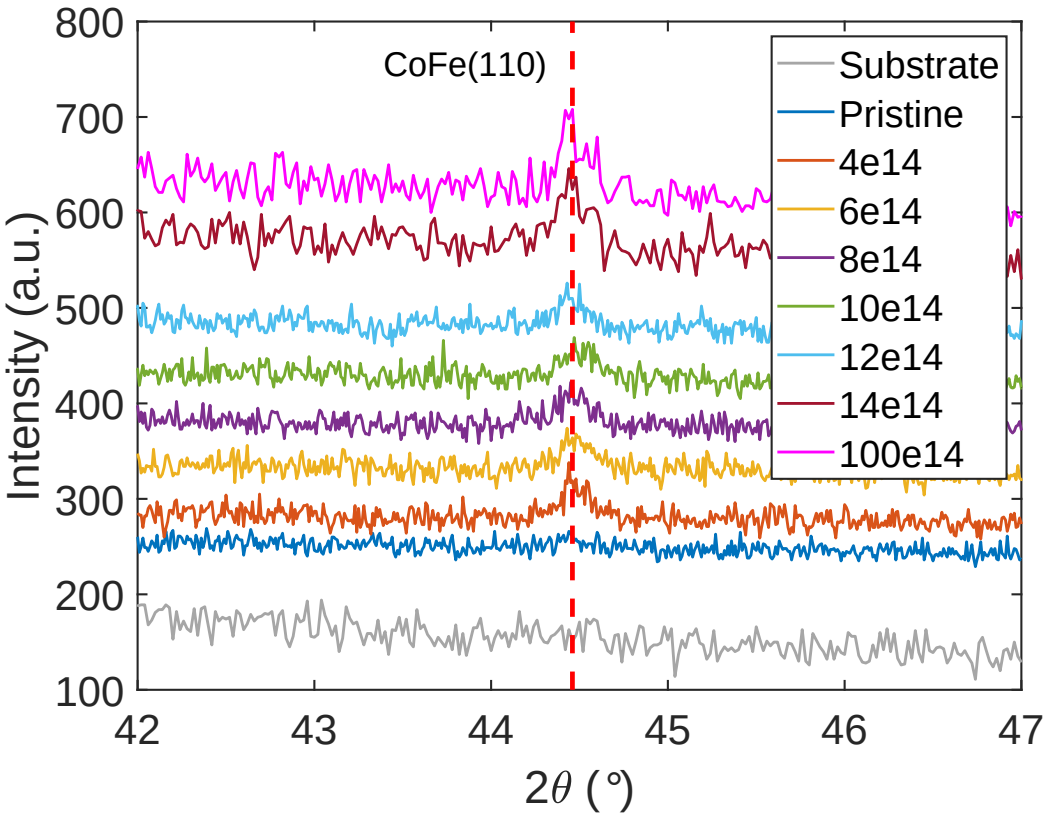

FIGURE 3.9: The XRD patterns around $2\theta = 44.5°$ of Ta(2)/CoFeB(1) samples

The samples are irradiated with different doses, where the peak position of the CoFe (110) direction is marked with a red dotted line. The y-axis is in a common axis. The patterns are vertically shifted in order of the doses from the bottom to the top. The pattern of the Si substrate is shown at the bottom for reference.

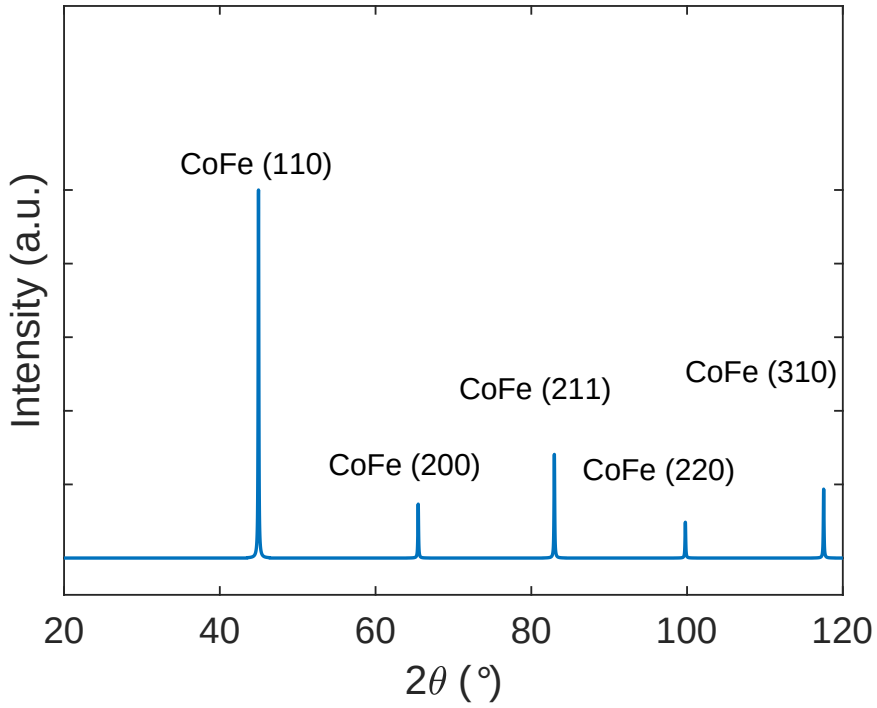

FIGURE 3.10: The simulated XRD patterns of CoFe crystal.

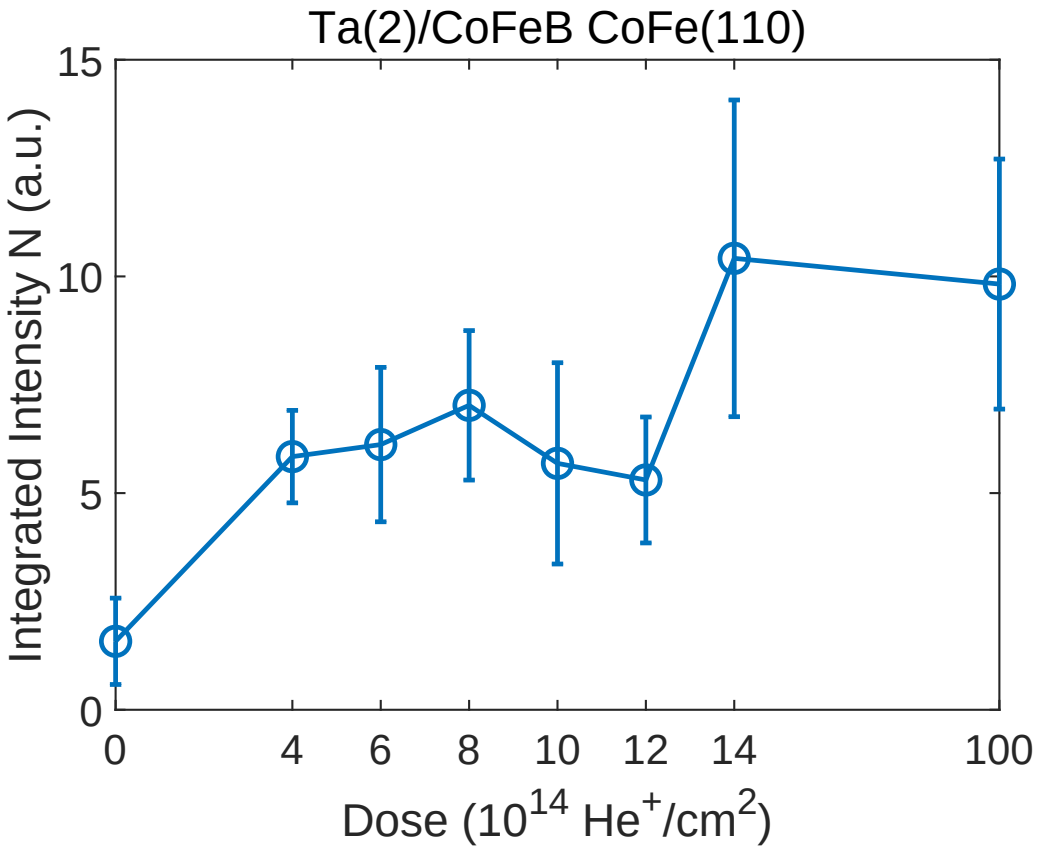

FIGURE 3.11: The integrated intensity of the CoFe (110) characteristic peak of irradiated Ta(2)/CoFeB(1) samples.

For verificating this mechanism, the sample of Ta(2)/CoFeB(1) irradiated by very high dose ($100 \times 10^{14}\,\mathrm{He}^+/\mathrm{cm}^2$), and measured by VSM. The M-H loop result is shown in figure 3.13. The scanning external field H_{ex} is from the out-of-plane direction and in-plane direction in figure 3.13 a and 3.13 b, respectively. Compared with the good PMA property of other samples shown in figure 3.6, the sample of dose $100 \times 10^{14}\,\mathrm{He}^+/\mathrm{cm}^2$ lost its PMA property completely after irradiation and changed into in-plane anisotropy as shown in figure 3.13 b. As known that the PMA property of Ta/CoFeB comes from the crystallization of the CoFe (001) phase, therefore the loss of PMA property in the samples irradiated by high doses means the destruction of CoFe (001) crystal. In the doses that are not too high $8 \times 10^{14}\,\mathrm{He}^+/\mathrm{cm}^2$ to $14 \times 10^{14}\,\mathrm{He}^+/\mathrm{cm}^2$), the CoFe (001) phase is still the dominant phase of CoFeB layer, though the crystallinity already started to decrease. Even if the crystallinity of CoFe (110) increases, its contribution to m_s is much smaller than the dominant phase, and there are no benefits to the PMA property. Consequently, the samples still keep PMA property, but the m_s turns to decrease from the dose $8 \times 10^{14}\,\mathrm{He}^+/\mathrm{cm}^2$.

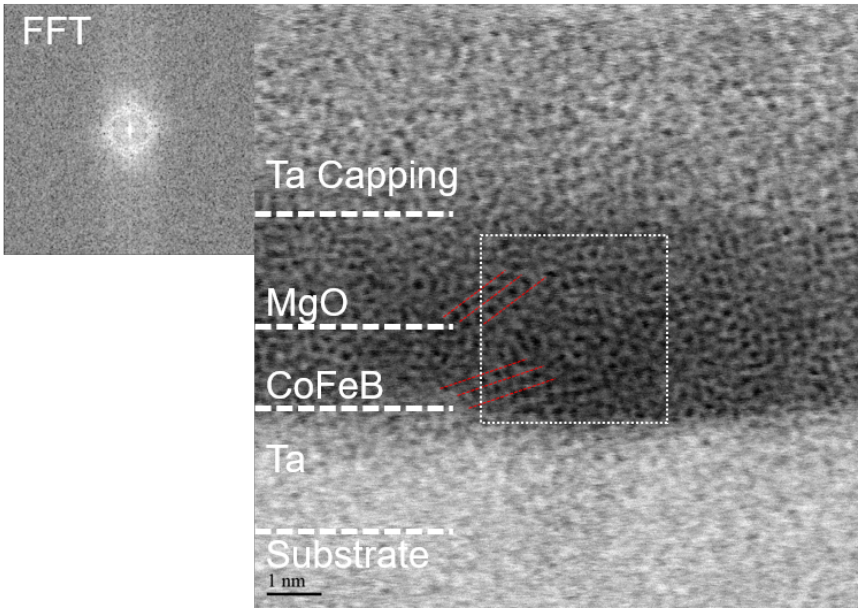

A: Pristine Ta(2)/CoFeB(1).

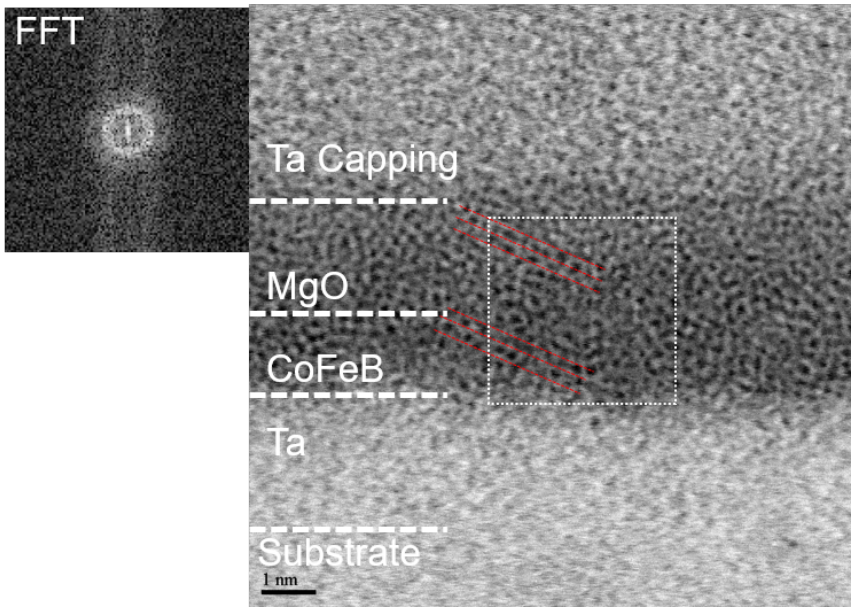

B: Ta(2)/CoFeB(1) with dose $10 \times 10^{14}\,He^+/cm^2$.

FIGURE 3.12: The STEM figures of pristine and dose $10 \times 10^{14}\,He^+/cm^2$ samples.

The FFT image of the white dotted square area is in the top left corner. The red dotted lines mark the periodic arrangement of atoms.

3.2.2 The Collision from He Ion Irradiation in Bulk and the Created Frenkel Pair

The Frenkel defect is a kind of defect in the bulk created by the displacement of atoms. When an atom in the lattice is kicked out from the lattice for some reason, a vacancy and an interstitial atom remain, which is called the Frenkel defect, and the pair of the vacancy and the interstitial atom is called the Frenkel pair.[29, 30] In the case of He ion irradiation, the collision of atoms with He ions or the secondary scattered atoms leads to the displacement of atoms from the lattice, creating a Frenkel pair.[31] The stability of the Frenkel pair depends on the transferred energy, thus related to different processes as shown in figure 3.14.[32, 23]

In each collision event, transferred energy T is transferred from the incident ion or secondary atom to the scattered atom, and the subsequent behavior of the scattered atom depends on the relationship between the transferred energy T and the displacement threshold energy U_d. In the case of very small T that we have $T < U_d$, the scattered atom is still bonded in the lattice; thus, no Frenkel pair is created, and the transferred energy T is dissipated into thermal energy of the bulk. In the case of intermediate T that we have $U_d < T < 2.5U_d$, the scattered atom is kicked out from the lattice for a short distance, remaining a vacancy, thus creating a meta-stable Frenkel pair. This is the most common case in He ion irradiation with doses not too high. There are two different results of this case. Firstly, the scattered atom may recombine with the vacancy to the original location within a very short relaxation time. The result of this collision event is similar to the thermal vibration. Secondly, the scattered atom may replace another lattice site as a substitution atom, which is the rearrangement of atoms. When this case happens in the interface between different layers, the intermixing is modified. In the case of a very high T, the scattered atom is kicked out far away from the original location, thus the Frenkel pair can not recombine anymore. This case remains a Frenkel defect in the bulk, and the damage accumulates more seriously with higher doses, leading to the crystal's destruction.

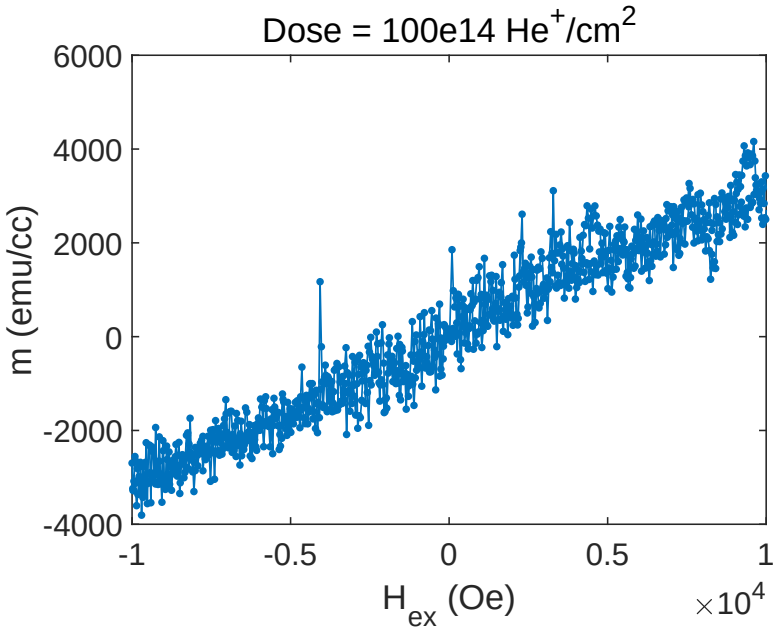

A: External field H_ex scanning from the out-of-plane direction.

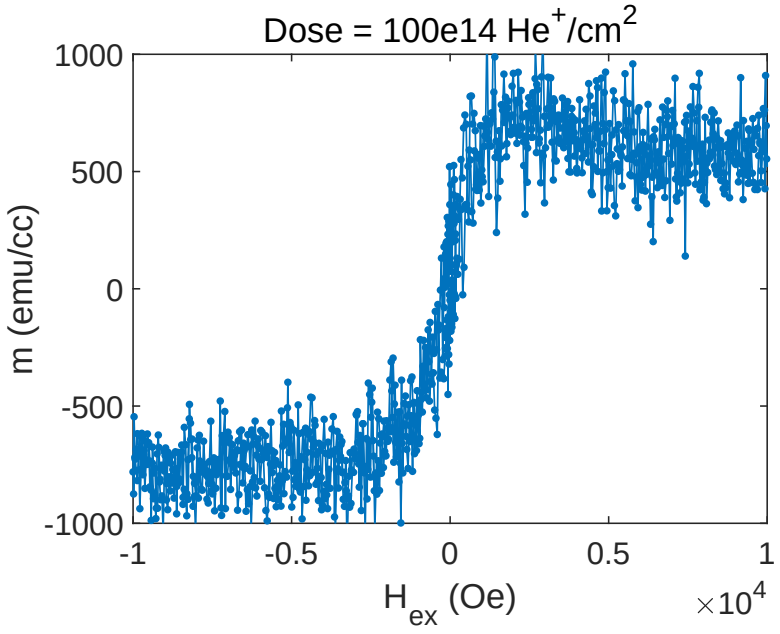

B: External field H_ex scanning from the in-plane direction.

FIGURE 3.13: The M-H loop of Ta(2)/CoFeB(1) irradiated by dose $100 \times 10^{14}\,\mathrm{He}^+/\mathrm{cm}^2$.

Since the low mass of the Helium ion and the incident energy we choose, the transferred energy T of most collision events is within the intermediate range. The rearrangement of atoms modifies the properties as expected, and some original defects can be repaired. However, according to the normal distribution of the transferred energy, a small part of the collision with too high T always creates Frenkel defects in the bulk. With the increase of irradiation dose, the defects accumulate, and finally, the destructive effect significantly overcomes the improvement from the rearrangement of atoms, that is, the cases of dose $14 \times 10^{14}\,\mathrm{He}^+/\mathrm{cm}^2$ and $100 \times 10^{14}\,\mathrm{He}^+/\mathrm{cm}^2$. In the thinner samples, this negative effect may show much easier due to the high strain inside or lower quality of the original lattice.

3.2.3 The XRD Patterns of the Thicker Ta(3,4)/CoFe(1) Samples

Since the situation of the group of thinner Ta(2)/CoFe(1) samples discussed in the last subsection, the unexpected crystallization of CoFe (110) and damage on the lattice may happen due to the He ion irradiation, it's necessary to check crystallization situation in the other group, the thicker Ta(3,4)/CoFeB(1) samples.

The XRD patterns of Ta(3,4)/CoFe(1) samples are shown in figure 3.15 in the same way. It notes that the y-axis is in a logarithm here to show the whole profile clearly. As expected, no characteristic peaks in addition to the substrate are spotted in the irradiated samples of both Ta(3)/CoFeB(1) and Ta(4)/CoFeB(1) due to the amorphous Ta and the cancellation of CoFe (110).

To specifically check the crystallization of CoFe (110), the XRD patterns of Ta(3,4)/CoFe(1) samples are also zoomed in around $2\theta = 44.5^\circ$ in common axis as shown in figure 3.16. There is no signal spotted for the crystallization of CoFe (110) in both Ta(3,4)/CoFe(1) samples. It shows consistent results compared with the results of m_s in constant in figure 3.5 because the crystallinity CoFe (001) of thicker samples is higher and no CoFe (110) is created. The coercive field h_c in figure 3.5 b decreases from the pristine sample until the dose $6 \times 10^{14}\,\mathrm{He}^+/\mathrm{cm}^2$, in consistance with previous studies as discussed in the previous section. In the high dose of $10 \times 10^{14}\,\mathrm{He}^+/\mathrm{cm}^2$, the damage from the irradiation accumulates as discussed in the last subsection, leading to the increase of domain pinning and thus the increase of h_c. At the same time, the m_s is not changed so much because of the higher crystallinity of CoFe (001) and the absence of the creation of CoFe (110).

In device applications, a stable and gentle modification on m_s is usually required in engineering technology. The thickness of the ferromagnetic layer is usually constant or in a very narrow range due to the requirement of PMA property. Still, the thickness of the heavy metal layer may vary widely depending on the specific purpose or design. In the case of thicker samples, there is no problem with the requirement of stable m_s. However, in some studies with ultrathin films like Ref. [33, 34, 35, 36], it's better to

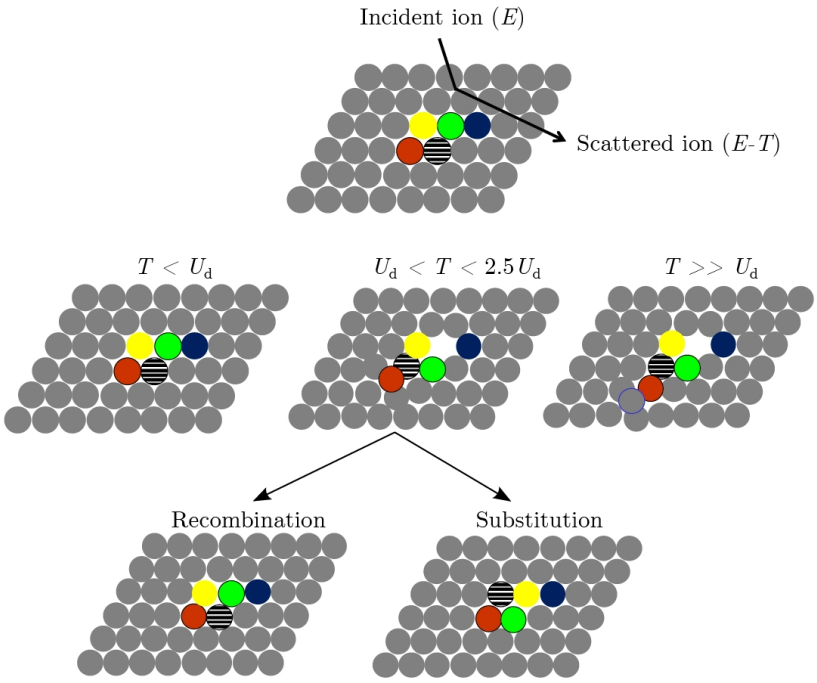

FIGURE 3.14: The different processes of the creation of Frenkel pair in bulk.

When the transferred energy T is lower than the threshold energy U_d, no atoms are kicked out from the lattice. When the T ranges from U_d to $2.5U_d$, a Frenkel pair is created, which may recombine or not. When the T is much higher than U_d, a stable Frenkel that is never recombined by itself is created, and the crystal is destroyed. The colorful circles indicate the individual atoms involved in the collision event, and the green circle indicates the first scattered atom. Figure adapted from Ref. [32].

consider the effect of unexpected crystallization in the ferromagnetic layer.

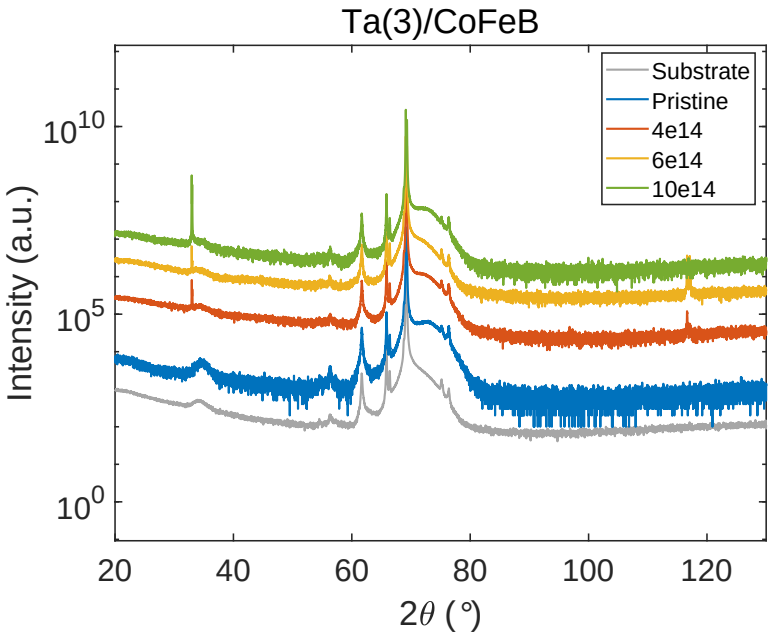

A: Ta(3)/CoFeB(1) samples.

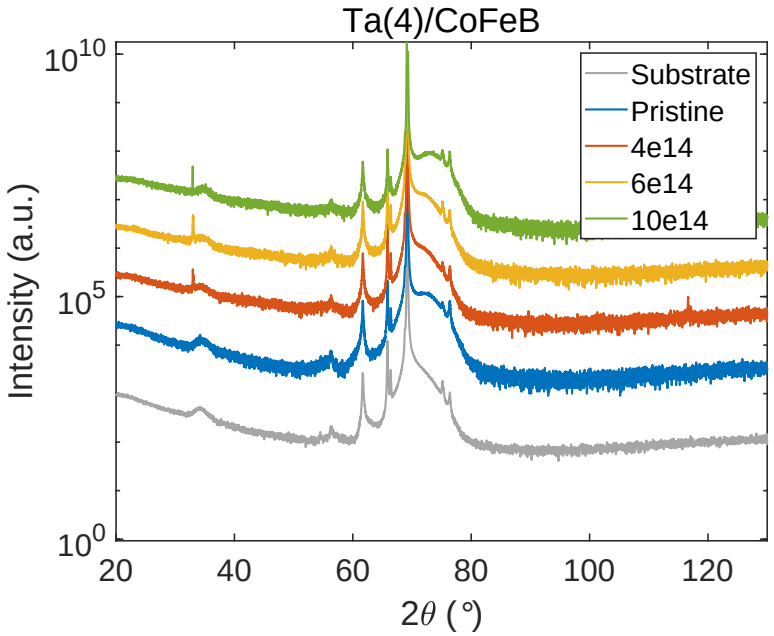

B: Ta(4)/CoFeB(1) samples.

FIGURE 3.15: The XRD patterns of (a) Ta(3)/CoFeB(1) samples and (b) Ta(4)/CoFeB(1) samples irradiated with different doses.

The y-axis is in logarithm. The patterns are vertically shifted in order of the doses from the bottom to the top. The pattern of the Si substrate is shown at the bottom for reference. No characteristic peak is spotted.

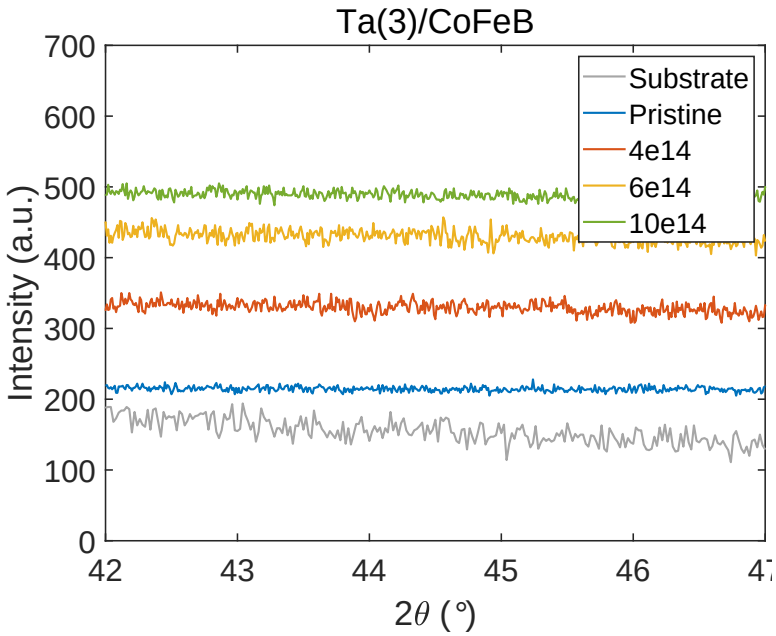

A: Ta(3)/CoFeB(1) samples.

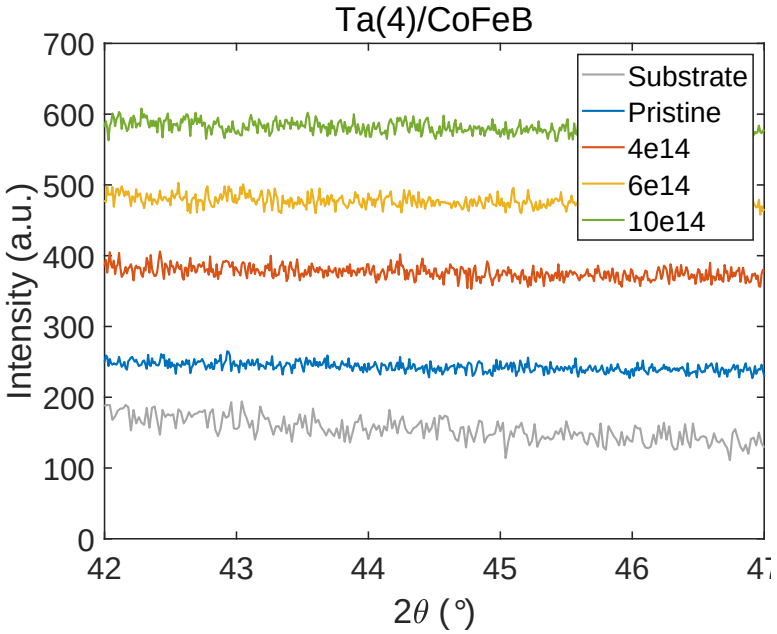

B: Ta(4)/CoFeB(1) samples.

FIGURE 3.16: The XRD patterns around $2\theta = 44.5°$ of(a) Ta(3)/CoFeB(1) samples and (b) Ta(4)/CoFeB(1) samples irradiated with different doses.

The y-axis is in a common axis. The patterns are vertically shifted in order of the doses from the bottom to the top. The pattern of the Si substrate is shown at the bottom for reference.

3.3 Conclusion

In this chapter, the magnetic properties of Ta/CoFeB samples are investigated by VSM. The M-H loop of samples is measured with an external magnetic field sweeping along the easy axis (out-of-plane direction). All the pristine samples and samples with an irradiation dose $< 14 \times 10^{14}\,\mathrm{He}^+/\mathrm{cm}^2$ remain PMA. The different behaviors of the extracted saturation magnetization m_s separate the samples into two groups: the thicker Ta(3,4)/CoFeB(1) samples and the thinner Ta(2)/CoFeB(1) samples. The group of Ta(3,4)/CoFeB(1) keeps a constant value of m_s after irradiation, which is suitable for device application as the stability. In comparison, the group of Ta(2)/CoFeB(1) shows a strong non-monotonic tendency, which increases about 30% until the dose $8 \times 10^{14}\,\mathrm{He}^+/\mathrm{cm}^2$ and then decreases. The coercivity field h_c of Ta(2)/CoFeB(1) also shows a similar tendency, suggesting the common origin. In the Ta/CoFeB samples with PMA, the crystallization of the CoFe (001) phase after annealing is very important. The change of m_s is attributed to the change of crystallinity of CoFe.

The crystallinity of Ta/CoFeB samples is measured by XRD to elucidate the reason for the change of m_s in the group of Ta(2)/CoFeB(1). The crystallinity of the new CoFe (110) phase is found in the irradiated Ta(2)/CoFeB(1) samples. The integrated intensity of XRD is analyzed for a quantitative discussion. In the lower doses, the results show the increasing crystallinity of the CoFe (110) consistent with the tendency of m_s, which means the increased crystallinity by the irradiation is the reason for the increased m_s. In the high doses, the dominant phase CoFe (001) in the CoFeB layer is damaged by the accumulated defects, leading to a decrease of m_s because the CoFe (001) is the easy axis of CoFe and the origin of the PMA property. However, the characteristic peak of CoFe (001) can not be measured since its bcc lattice. Therefore, we can only estimate the change of it with the change of m_s. On the other hand, no any extra crystallization is found in the irradiated thicker Ta(3,4)/CoFeB(1) samples, in consistent with the constant m_s.

In conclusion, we measured the magnetic properties of irradiated Ta/CoFeB samples and found the anomalous behavior of the m_s of Ta(2)/CoFeB(1) samples. This behavior is subsequently explained by the crystallization of the CoFe (110) phase.

Chapter 4

Thickness-dependent Pinning Density Modulation on Ta/CoFeB Thin Film

In this chapter, we present the study on the domain wall motion of irradiated Ta/CoFeB thin film. The domain wall motion is observed with a Kerr microscope by MOKE. We discuss the effects on different thicknesses of Ta/CoFeB qualitatively and quantitatively in section 4.1. Based on the model of the creep regime of domain wall motion, we discuss the different contributions from m_s, K_{eff}, and n_i. For determining the dominant contributions, the K_{eff} is measured by the anomalous Hall effect in section 4.2. Combining with the data of m_s and K_{eff}, we demonstrate the effect of irradiation on the pinning density n_i of the thicker Ta(3,4)/CoFeB(1) samples.

4.1 Domain Wall Motion Modulated by He Ion Irradiation

4.1.1 Introduction

As a competitive memory technology for high storage density and capacity, advanced racetrack memory devices based on the propagation of domain walls (DW) have received tremendous interest in recent years[37, 38], where the DW can be driven by a magnetic field directly, or an effective field through spin-transfer torque (STT) or spin-orbit torque (SOT).[39, 40, 4] One of the critical challenges before the practical application of racetrack memory is the sensitive dependence on the defects of materials because DW motion is interacted by both intrinsic defects related to the properties of materials and extrinsic defects that are introduced by the micro-nano fabrication processes and it usually uneasy to separate the different origins of defects in practical devices. Therefore, observing the motion of domain wall expansion directly on the samples before device fabrication is useful for investigating the effects on the materials' properties, including pinning landscape, average pinning energy barrier, and other magnetic properties. The Magneto-optic Kerr effect (MOKE) is a kind of magneto-optic effect describing the change of polarity angle and ellipticity of light reflecting from the surface of magnetic film. The intensity of the change is usually proportional to the magnetization. With this mechanism, we can measure the magnetization of samples quickly, as shown in the characterization part in Chapter 2.

When the measured direction of magnetization is perpendicular to the plane of the surface, it's called polarized-MOKE (p-MOKE). Combining with Kerr microscopy and coils for driving magnetic field, the images reflecting the DW motion can be obtained, where we can extract the information about the DW dynamics from the expansion of domains.[41] Since no additional treatments or device fabrication is necessary with this technology, this is a convenient and nondestructive method to

study the effects of He^+ ion irradiation on thin films with PMA avoiding the interference from fabrication.

4.1.2 Measurements Methods

The schematic of the measurements setup for domain wall motion observation is shown in figure 4.1, and the photo of the whole system is shown in figure 4.2, where the thin-film samples with PMA can be well measured. The sample is placed on the sample stage beneath the microscope. The sample stage combines magnetic coils connected to a bipolar DC supply to generate a magnetic field H_z along with the z-axis. The converted current factor is calibrated with a Hall magnetometer, and the rise time is confirmed to be ignorable compared with the measuring time. For the homogeneity of the magnetic field, the diameter of the coils should be large enough to cover the whole area of samples, and the homogeneity is also confirmed with a Hll magnetometer. Before measuring, the sample's magnetization should be saturated by a high enough applied field. When we apply a short pulse of a particular magnetic field on the sample, whose intensity depends on materials, a small nucleation would show on the film. A laser beam is projected on the film, and the reflecting light would show different polar angles θ_k depending on the direction of local magnetization as shown in figure 4.1. Then, the grayscale image of θ_k is transferred to a computer and saved.

The sequence of H_z pulses used for measurements is shown in figure 4.3. First, a high pulse of H_z is applied on the sample for a long enough time (usually more than 5 s) to saturate the sample, and the saturation is confirmed by the p-MOKE image. Second, a very short pulse of H_z is applied to create a nucleation of magnetic domains. The intensity can be high or low depending on the materials, but it does not impact the results. After the nucleation, we can find the domains by the microscope as shown in figure 4.4. Then, we can move the sample to focus on one clear domain as the original image and start the measurements. Pulses of a magnetic field with the

same intensity and time (e.g., pulses with 5 mT for 20 s) are applied on the sample one by one, and the Kerr microscope can observe the expansion of domain walls.

The obtained images of the domain wall expansion are combined into a single image by software for showing the expansion visually and calculating the distance of each expansion as figure 4.5. We choose the nonoverlapping, parallel, and clear boundaries as samples, and calculate the average velocity of the domain wall motion.

4.1.3 Qualitative Analysis of the Domain Wall Motion

The domain patterns of Ta/CoFeB with different thicknesses of Ta show several different types, as shown in figure 4.6. In figure 4.6, The patterns of Ta(2,3,4,5)/CoFeB(1) are arranged from left to right. The Ta(2)/CoFeB(1) pattern is a bubble-like domain, where the domain expands from the original nucleation to the outside isotropic. The patterns of Ta(3,4)/CoFeB(1) are significantly different, which nucleate from the edge of samples and then linearly expand toward other parts. With the increasing thickness of the Ta layer, the patterns of domains become more and more rough, and finally, as shown in the pattern of Ta(5)/CoFeB(1), that is dendritic even though it is still in linear expansion, indicating the change of the pinning landscape. In the case of Ta(2)/CoFeB(1), it is easy to define the distance of DW motion, which is the increase in the bubble's diameter. In the case of Ta(3,4)/CoFeB(1), the domain expanse linearly, and we can find the details of the edge remain unchanged during the expansion, so we can also define the distance of DW motion as the red arrows shown in figure 4.6. In the case of Ta(5)/CoFeB(1), the pattern of domains becomes very dendritic due to the texture of the film. Thus, it isn't easy to define DW motion's distance well. Therefore, in this work, we will only focus on the Ta(2,3,4)/CoFeB(1) samples as mentioned in Chapter 2. The different types between domain patterns of Ta(2)/CoFeB(1) and Ta(3,4)/CoFeB(1) also naturally separate them into two groups, consistent with the m_s analysis in Chapter 3.

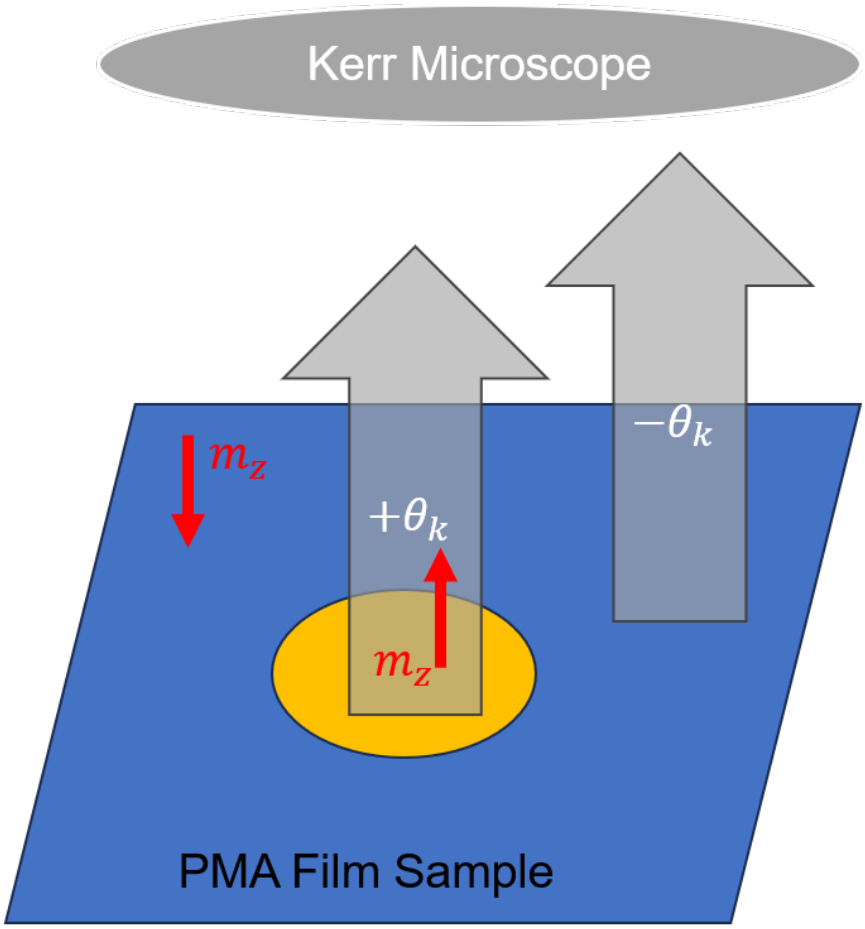

FIGURE 4.1: The schematic of the measurements setup.

FIGURE 4.2: The photo of the p-MOKE microscopy facility.

The left part includes the Kerr microscopy and accessory facilities for electric and magnetic control and measurements. The right part is the enlarged view of the Kerr microscopy.

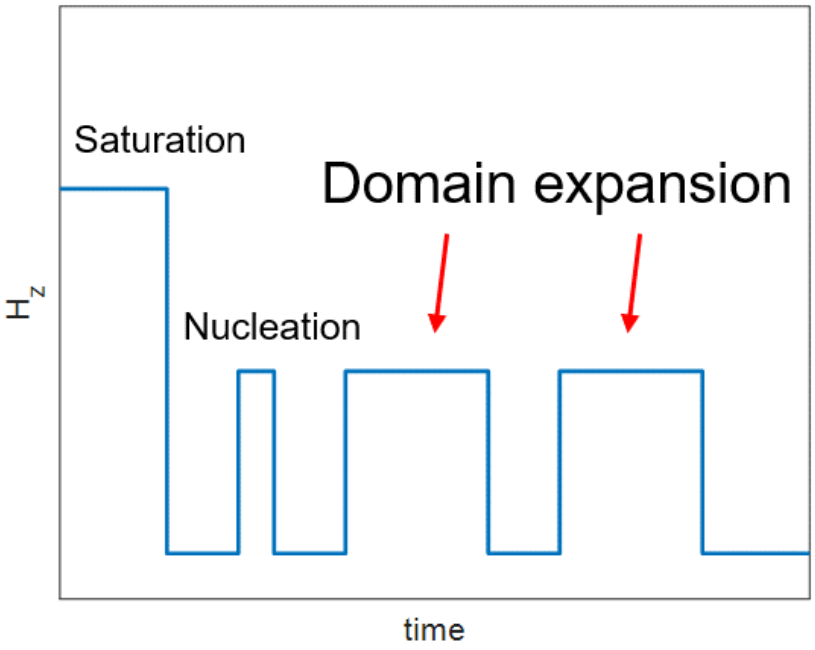

FIGURE 4.3: The magnetic field H_z sequence for saturation, domain nucleation, and domain expansion.

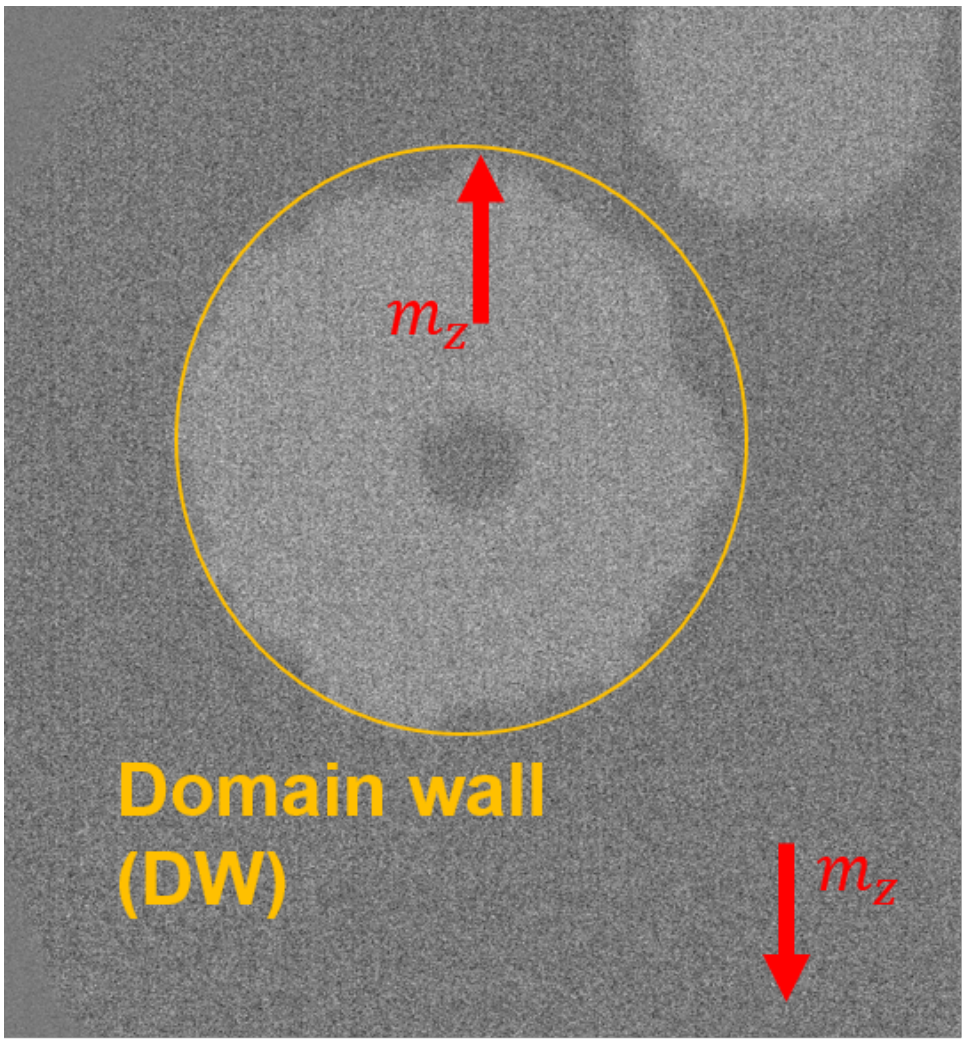

FIGURE 4.4: An image of the domain wall motion of pristine Ta(2)/CoFeB(1) samples.

The red arrows indicate the direction of magnetization, where we define the up direction as $+m_z$. The yellow circle indicates the domain wall.

Figure 4.7 shows the patterns of pristine and irradiated Ta(2)/CoFeB samples under the same driving magnetic field. Only pristine and irradiation doses 4, 6, 10 $10^{14}\,\mathrm{He}^{+}/\mathrm{cm}^{2}$ are shown as examples, but all irradiated samples are measured. For obtaining eligible images, the driving time differs from 10 s to 60 s as the description.

In all different irradiation samples, the domain patterns remain in a bubble-like shape. The patterns of pristine and irradiation dose 4 and 10 $10^{14}\,\mathrm{He}^{+}/\mathrm{cm}^{2}$ look almost the same, except the edge is smoother and isotropic, which may be due to the modification on pinning sites. However, the pattern of the irradiation dose $6 \times 10^{14}\,\mathrm{He}^{+}/\mathrm{cm}^{2}$ is specifically rough compared with other samples, which may be due to the change from magnetic properties and crystallization as discussed in Chapter 3.

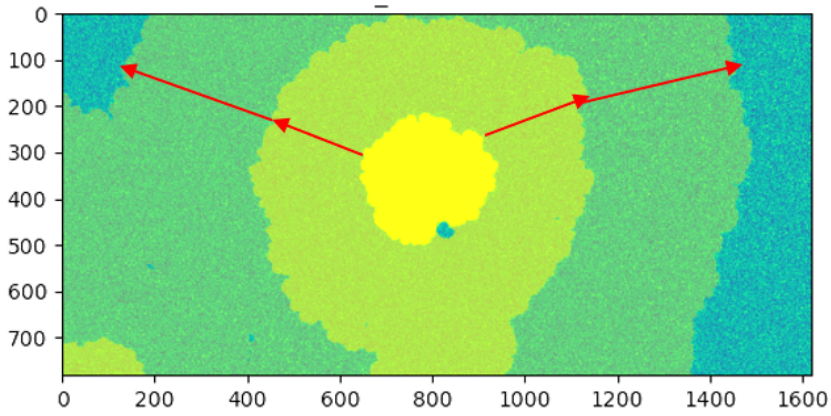

FIGURE 4.5: An image of the domain wall expansion of pristine Ta(2)/CoFeB(1) samples, composite with 3 images.

The red arrows indicate the expansion of domain walls.

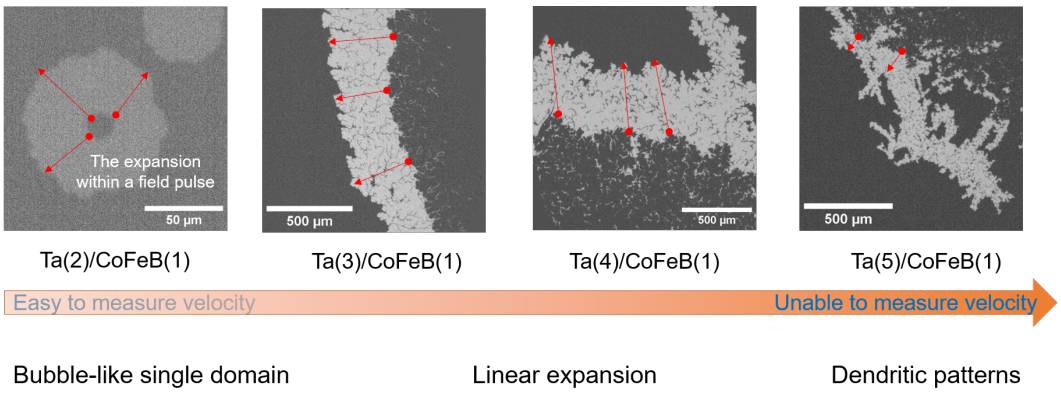

FIGURE 4.6: The different domain patterns of Ta/CoFeB with different Ta thickness.

The red arrows show the expansion of the domain wall.The driving magnetic fields from left to right are 4.45 mT, 1.31 mT, 1.31 mT, 2.36 mT, respectively.

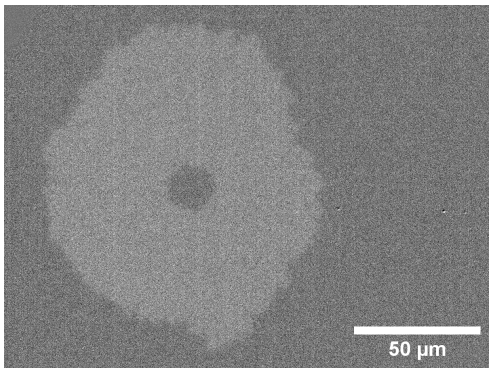

A: Ta(2)/CoFeB(1) pristine.

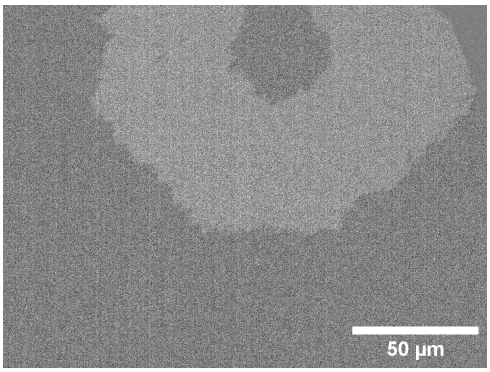

B: Ta(2)/CoFeB(1) dose $4 \times 10^{14}\,\mathrm{He}^{+}/\mathrm{cm}^{2}$.

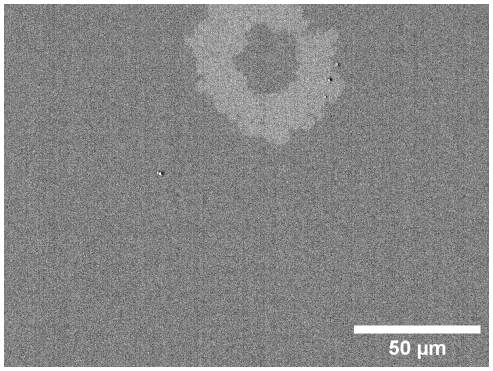

C: Ta(2)/CoFeB(1) dose $6 \times 10^{14}\,\mathrm{He}^{+}/\mathrm{cm}^{2}$.

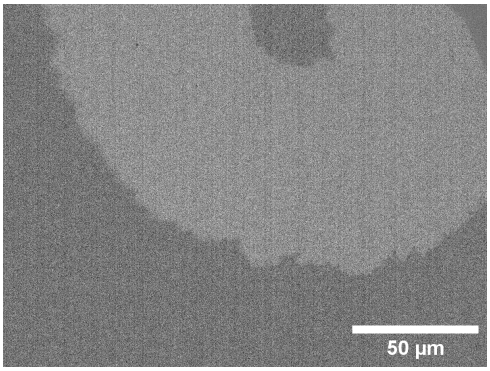

D: Ta(2)/CoFeB(1) dose $10 \times 10^{14}\,\mathrm{He}^{+}/\mathrm{cm}^{2}$.

FIGURE 4.7: The domain patterns of Ta(2)/CoFeB(1) with different irradiation doses.

(a) Pristine, (b) $4 \times 10^{14}\,\mathrm{He}^{+}/\mathrm{cm}^{2}$, (c) $6 \times 10^{14}\,\mathrm{He}^{+}/\mathrm{cm}^{2}$, (d) $10 \times 10^{14}\,\mathrm{He}^{+}/\mathrm{cm}^{2}$. The driving field $H_z = 3.06\,\mathrm{mT}$, the driving time is 60 s, 10 s, 30 s, 10 s, respectively.

As shown in figure 4.8, the domain patterns of Ta(3)/CoFeB(1) are significantly modified a lot by the irradiation. It notes that the driving magnetic field $H_z = 1.66\,\mathrm{mT}$ for pristine and irradiation doses $4 \times 10^{14}\,\mathrm{He^+/cm^2}$ and $10 \times 10^{14}\,\mathrm{He^+/cm^2}$ for comparison, but in sample of $6 \times 10^{14}\,\mathrm{He^+/cm^2}$ it can only reach $1.31\,\mathrm{mT}$ in a reasonable long driving time $4\,\mathrm{s}$ since the limitation of the rise time of H_z.

In all samples, the expansion of domains remains in the linear expansion. However, the texture, or the cracks in the domain, corresponding to the peaks in the pinning landscape, are modified from random to orderly parallel. In figure 4.8 a, the cracks in the domain of the pristine sample are growing randomly along with the expansion of the domain wall. In the figures of irradiated samples 4.8 b c d, especially very clear in figure 4.8 c, corresponding to the sample with irradiation dose $6 \times 10^{14}\,\mathrm{He^+/cm^2}$. The rearrangement of cracks indicates the effect of irradiation on the pinning landscape. Such an improvement should be beneficial to the domain wall motion. In figure 4.8 d, the cracks turn out to be random again, not as parallel as the sample $6 \times 10^{14}\,\mathrm{He^+/cm^2}$, which means the accumulation defects from the irradiation tend to damage the structure, in consistency with the mechanism of $\mathrm{He^+}$ ion irradiation discussed in Chapter 1.

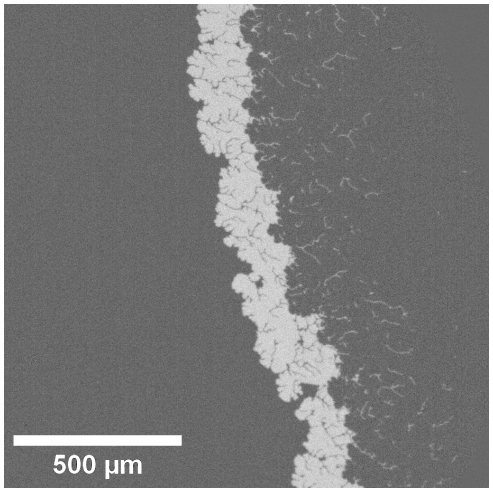

A: Ta(3)/CoFeB(1) pristine.

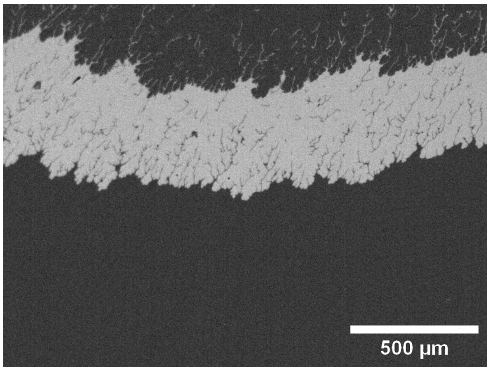

B: Ta(3)/CoFeB(1) dose $4 \times 10^{14}\,\mathrm{He}^{+}/\mathrm{cm}^{2}$.

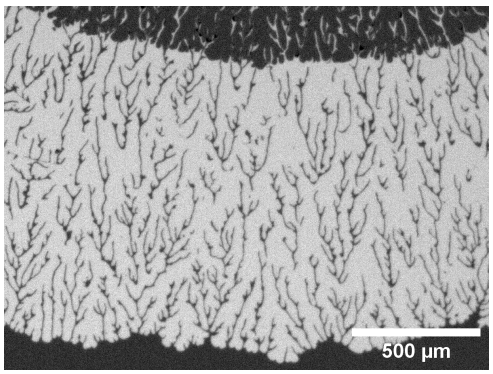

C: Ta(3)/CoFeB(1) dose $6 \times 10^{14}\,\mathrm{He}^{+}/\mathrm{cm}^{2}$.

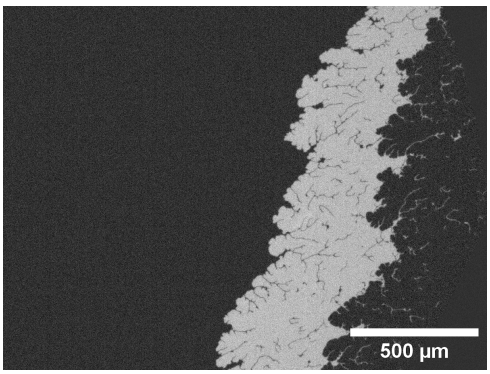

D: Ta(3)/CoFeB(1) dose $10 \times 10^{14}\,\mathrm{He}^{+}/\mathrm{cm}^{2}$.

FIGURE 4.8: The domain patterns of Ta(3)/CoFeB(1) with different irradiation doses.

(a) Pristine, (b) $4 \times 10^{14}\,\mathrm{He}^{+}/\mathrm{cm}^{2}$, (c) $6 \times 10^{14}\,\mathrm{He}^{+}/\mathrm{cm}^{2}$, (d) $10 \times 10^{14}\,\mathrm{He}^{+}/\mathrm{cm}^{2}$. The driving field $H_z = 1.66\,\mathrm{mT}$ for (a), (b), (d), and 1.31 mT for (c). The driving time is 5 s, 10 s, 4 s, 5 s, respectively.

In the case of Ta(4)/CoFeB(1), as shown in figure 4.9, the situation is similar to the Ta(3)/CoFeB(1), the domain wall motion of all samples remains in linear expansion after irradiation, and the cracks in the domain are modified from random to orderly parallel by irradiation. However, they are more rough and dendritic than Ta(3)/CoFeB(1). Specifically, the patterns of the domain in the pristine Ta(4)/CoFeB(1) are becoming dendritic towards the patterns of Ta(5)/CoFeB(1) in figure 4.6. Therefore, it's hard to define the distance of domain wall motion. However, after irradiation, the edge of patterns are much more smooth and isotropic so that we can measure the distance of domain wall motion again, showing the strong modification from He^+ ion irradiation.

4.1.4 Quantitative Analysis of the Domain Wall Motion

In the last subsection, we discussed the difference in domain patterns between the pristine and irradiated Ta(t_N)/CoFeB(1) thin films. However, although the He^+ ion irradiation visually shows different effects on samples with varying thicknesses of the Ta layer, it is hard to compare the effects quantitatively. In this subsection, the distance of the domain wall motion driven by different magnetic field intensities H_z is measured and fitted by the model of creep regime as introduced in subsection **??**.

Since the velocity of domain wall motion v in the creep regime is described as

$$v = v_0 exp((\frac{-U_c}{k_B T})(\frac{H_{dep}}{H})^{\frac{1}{4}}), \tag{4.1}$$

where the U_C is the pinning energy, H_{dep} is the depinning field, k_B is Boltzmann constant, T is the temperature, and H is the driving magnetic field H_z in our cases.

If we take the logarithm of both sides, we will have

$$ln(v) = (\frac{-U_c}{k_B T})(\frac{H_{dep}}{H})^{\frac{1}{4}} + v_0. \tag{4.2}$$

From the equation (4.2) we can see the $ln(v)$ should be proportional to $H^{-\frac{1}{4}}$ in single sample. Subsequently we will have the slope $\zeta = \left|(\frac{-U_c}{k_B T} H_{dep}^{\frac{1}{4}})\right|$.

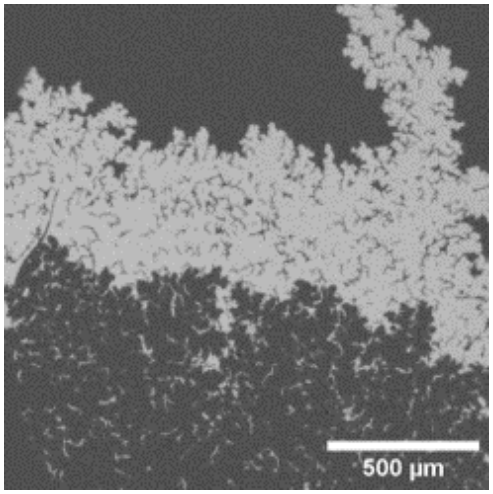

A: Ta(4)/CoFeB(1) pristine.

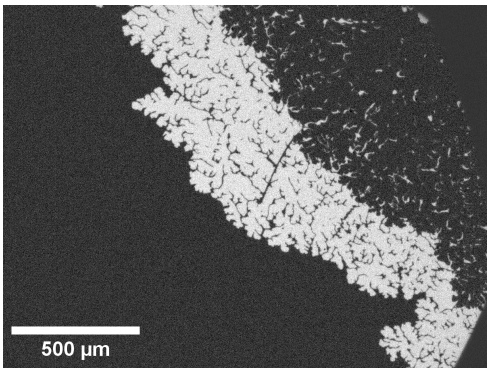

B: Ta(4)/CoFeB(1) dose $4 \times 10^{14}\,\mathrm{He}^{+}/\mathrm{cm}^{2}$.

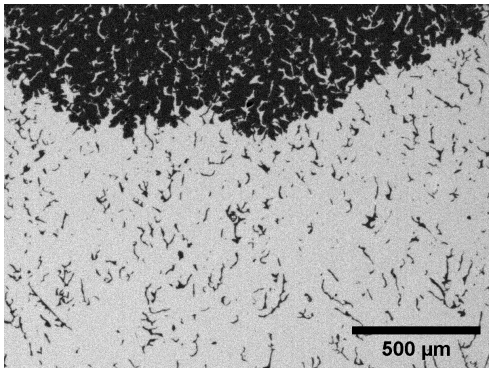

C: Ta(4)/CoFeB(1) dose $6 \times 10^{14}\,\mathrm{He}^{+}/\mathrm{cm}^{2}$.

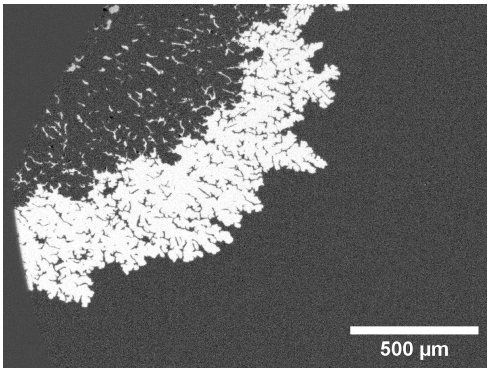

D: Ta(4)/CoFeB(1) dose $10 \times 10^{14}\,\mathrm{He}^{+}/\mathrm{cm}^{2}$.

FIGURE 4.9: The domain patterns of Ta(4)/CoFeB(1) with different irradiation doses.

(a) pristine, (b) $4 \times 10^{14}\,\mathrm{He}^{+}/\mathrm{cm}^{2}$, (c) $6 \times 10^{14}\,\mathrm{He}^{+}/\mathrm{cm}^{2}$, (d) $10 \times 10^{14}\,\mathrm{He}^{+}/\mathrm{cm}^{2}$. The driving field $H_z = 1.31\,\mathrm{mT}$ for all samples. The driving time is 5 s.

In the ideal cases, if we can scan the magnetic field H_z to high intensity for covering the whole creep regime, we can directly extract the parameter H_{dep}. However, because the velocity is exponentially increasing with increasing H_z, it is impossible to cover the whole creep regime in our samples due to the limitations of the field of view of the Kerr microscope and the rise time of the magnetic field.

Furthermore, the parameters U_c and H_{dep} in equation (4.1) and (4.2) are the physical parameters of the model, it would be better to convert them into material parameters that we can directly measure. In the model of domain wall motion, the physical parameters are relative to the magnetic properties of thin films, we have

$$U_c \propto \sqrt{K_{eff}} n_i^{\frac{1}{3}}, \tag{4.3}$$

and

$$H_{dep} \propto \frac{\sqrt{K_{eff}} n_i^{\frac{2}{3}}}{m_s}, \tag{4.4}$$

where the K_{eff} is the effective anisotropy, n_i is the pinning density, and m_s is the saturation magnetization.[24]

Combining the equations (4.3) and (4.4) into the equation (4.2), we can extract the relationship between the slope ζ and the materials properties m_s, K_{eff}, and n_i as

$$\zeta \propto m_s^{-\frac{1}{4}} K_{eff}^{\frac{5}{8}} n_i^{\frac{1}{2}}. \tag{4.5}$$

In equation (4.5), the materials parameters m_s and K_{eff} can be directly measured. Thus, such a conversion would be very convenient for the analysis.

According to the model of the creep regime, we take the logarithm of the velocity of domain wall motion and the $H_z^{-1/4}$ as figure 4.10, which shows a linear relationship as expected. The curves of different irradiation doses are vertically shifted for a clearer visual since the intercept is not crucial in our analysis.

With the method introduced above, the slope ζ of each curve of Ta(2,3,4)/CoFeB(1)

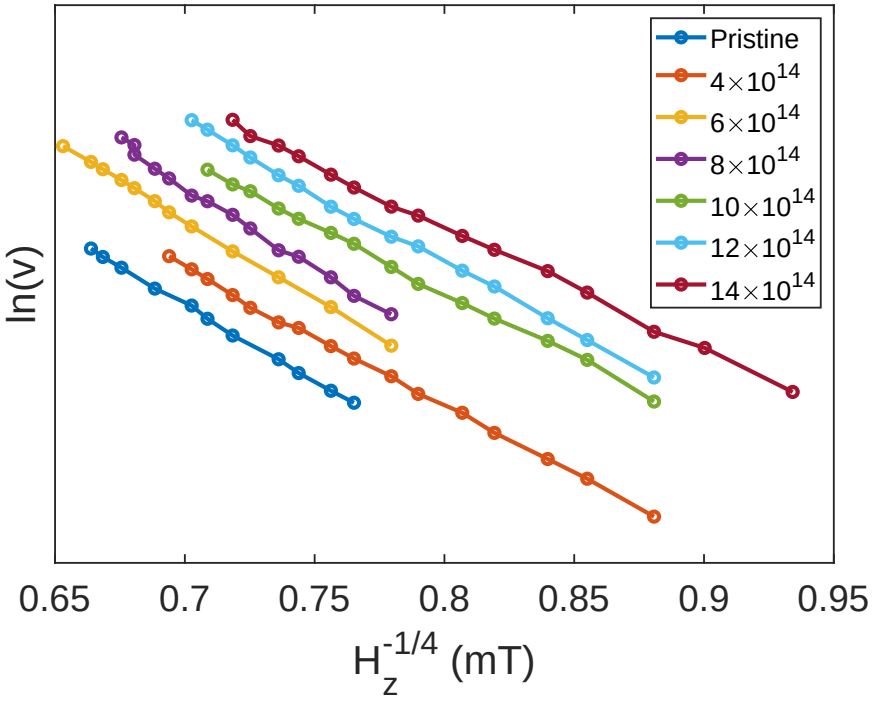

FIGURE 4.10: The domain wall motion velocity of Ta(2)/CoFeB(1).

The velocity is in logarithm, and the x-axis is $H_z^{-1/4}$. The curves are vertically shifted from bottom to top in the order of irradiation dose.

is extracted by linear fitting as shown in figure 4.11. The tendency of slopes can be obviously separated into two groups, Ta(2)/CoFeB(1) and Ta(3,4)/CoFeB(1), which is consistent with the previous discussion. The group of Ta(2)/CoFeB(1) shows an entirely different tendency from Ta(3,4)/CoFeB(1), suggesting the different physical origin behind it.

In the group of Ta(3,4)/CoFeB(1), both thicknesses show an identical tendency opposite to Ta(2)/CoFeB(1) depending on the irradiation dose, just different in the values. The slope ζ determines the exponential relationship between the driving magnetic field and the velocity of domain wall motion. Thus, the lower slope ζ means the easier controlled by the magnetic field. From the view of the device application, lower values of ζ would be more desirable for STT- or SOT-based devices because lower modulation on switching current is needed. In figure 4.11, Ta(2)/CoFeB(1) and Ta(3)/CoFeB(1) have similarly low values, meaning their better adaptability in device application. However, as discussed in Chapter 3, the m_s of Ta(2)/CoFeB(1) is not stable due to the unexpected crystallization of CoFe (110), so it should be avoided. On the other hand, the ζ of Ta(3)/CoFeB(1) is significantly decreased in the irradiation dose $6 \times 10^{14}\,\mathrm{He}^{+}/\mathrm{cm}^2$, showing an excellent improvement in the performance.

Subsequently, we can discuss the different effects of the He^+ ion irradiation on the two groups of samples. As shown in equation (4.5), we have $\zeta \propto m_s^{-\frac{1}{4}} K_{eff}^{\frac{5}{8}} n_i^{\frac{1}{2}}$, which means there are 3 main contribution to the slope ζ. As for the group of Ta(3,4)/CoFeB(1), the slope ζ and m_s are compared in figure 4.12, where the m_s is measured in Chapter 3. The m_s of both Ta(3,4)/CoFeB(1) keep constant after irradiation, instead of the inverse relationship as shown in equation (4.5), which means the slope ζ is not modulated through the m_s.

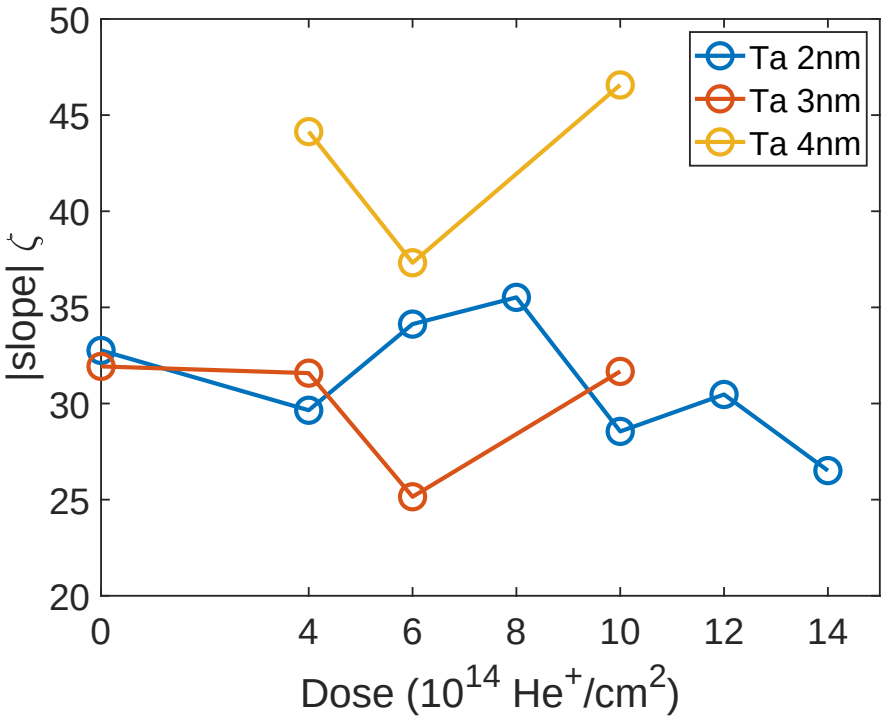

FIGURE 4.11: The extracted slope ζ of Ta/CoFeB.

In the group of Ta(2)/CoFeB(1), the slope ζ and m_s are compared in figure 4.13. Although both the ζ and m_s are strongly modulated by irradiation and reach the summit in the irradiation dose $8 \times 10^{14}\,\mathrm{He}^{+}/\mathrm{cm}^2$, they show the same tendency instead of the inverse relationship as shown in equation (4.5), therefore the m_s is nether the main contribution the ζ in this case.

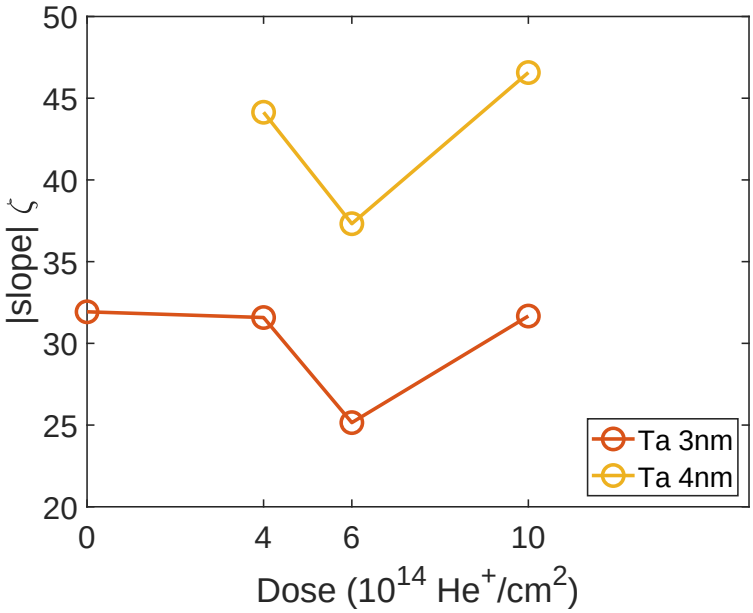

A: The extracted slope ζ of Ta(3,4)/CoFeB(1).

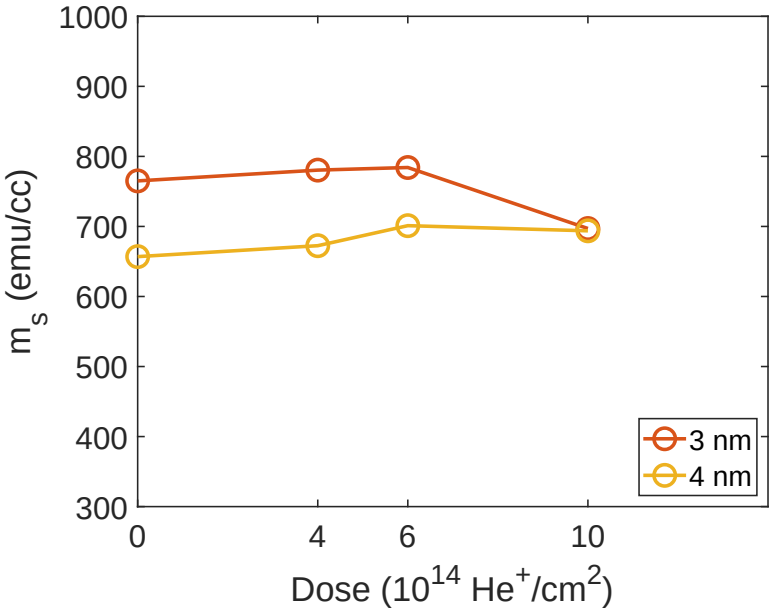

B: The saturation magnetization m_s of Ta(3,4)/CoFeB(1).

FIGURE 4.12: The comparison between the extracted slope ζ and m_s of Ta(3,4)/CoFeB(1).

The summary of the contribution to the slope ζ is shown in the figure 4.14. As discussed above, m_s is confirmed not the dominant contribution in all irradiated samples. According to the relationship 4.5, the remaining contributions are K_{eff} and n_i. The K_{eff} will be discussed in the next section.

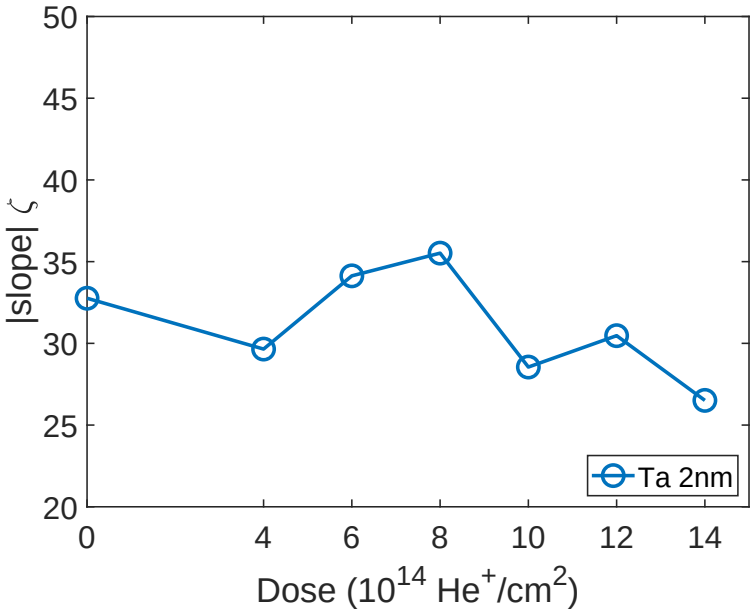

A: The extracted slope ζ of Ta(2)/CoFeB(1).

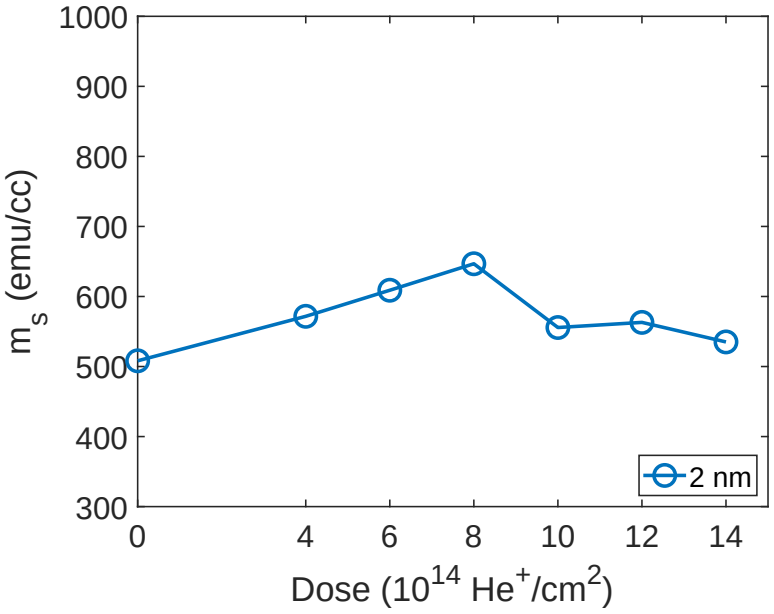

B: The saturation magnetization m_s of Ta(2)/CoFeB(1).

FIGURE 4.13: The comparison between the extracted slope ζ and m_s of Ta(2)/CoFeB(1).

4.2 Measuring Magnetic Anisotropy by Anomalous Hall Effect

In the previous section, the effective anisotropy K_{eff} is demonstrated as one of the possible contributions to the slope ζ. The K_{eff} can be measured by measuring the magnetization with a scanning magnetic field along with the easy axis and the hard axis. However, due to the limitation of the VSM facility, measuring the magnetization directly along the hard axis is difficult. In the anomalous Hall effect (AHE), the transverse resistance of a ferromagnet/metal bilayer increases anomalously when a magnetic field is applied due to the magnetization tilted by the field, and the AHE signal is proportional to the z-component of magnetization.[42, 43] Therefore, here, we will measure the AHE of Hall bar structures instead of the magnetization of bare films, which have a much higher sensitivity.

The thin-film samples are fabricated into Hall bar structures with the standard photolithography method, as shown in Chapter 2. The geometry of the Hall bar structures and the schematic of the electrical circuit for AHE measurements are shown in figure 4.15. The probe current is 0.1 mA DC by a YOKOGAWA GS200 DC source. The transverse voltage is measured by a Keysight 34411A $6_{1/2}$ Digit Multimeter.

4.2.1 Generalized Sucksmith-Thompson Method

Since the limitation of the scanning magnetic field for our probe station is only 800 mT in the x-y plane, it is difficult to saturate the magnetization along the hard axis sufficiently. Here, we follow the generalized Sucksmith-Thompson (GST) method to fit the anomalous Hall resistance data to extract the 1st-order perpendicular magnetic anisotropy field.[44, 45, 46, 25] It notes that the obtained 1st order anisotropy fields are the effective anisotropy, including the demagnetization effect.

Thickness	m_s	K_{eff}	n_i
2	×		
3	×		
4	×		

FIGURE 4.14: The summary table of the contribution to the slope ζ.

The crosses mean the parameters are confirmed as not a dominant origin. The thickness notes the thicknesses of Ta layers.

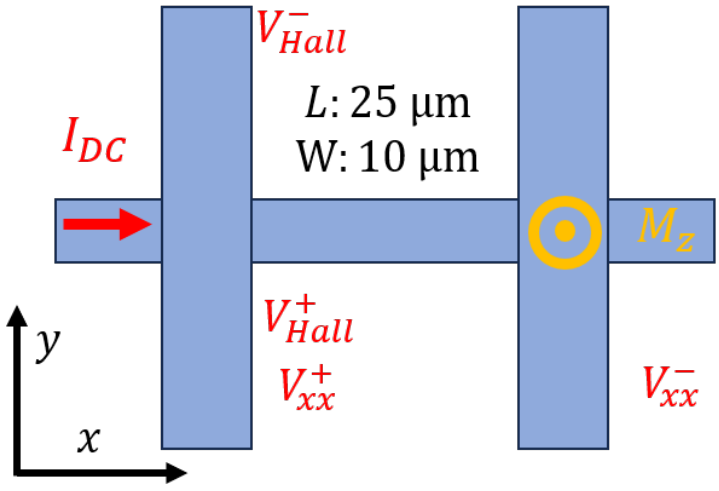

FIGURE 4.15: The geometry of the Hall bar structures and the schematic of the electrical circuit for AHE measurements.

In the GST method, for the anisotropy energy $E(\theta_M)$ of a certain polar angle of the tilted magnetizaiton θ_M we have

$$E(\theta_M) = K_1^{eff} sin^2\theta_M + K_2 sin^4\theta_M, \tag{4.6}$$

where the K_1^{eff} and K_2 are the 1st and 2nd order effective anisotropy field, respectively.

The measured parameters follow the equation,

$$H_{K1}^{eff} + H_{K2}(1 - m^2) = \alpha H_{ex}, \tag{4.7}$$

$$\alpha = \frac{msin\theta_H - \sqrt{1-m^2}cos\theta_H}{m\sqrt{1-m^2}}, \tag{4.8}$$

where the H_{K1}^{eff} and H_{K2} are the 1st and 2nd order PMA effective field, respectively. $m = cos\theta_M = R_H(H_{ex}/R_{AHE})$ is the normalized magnetization, R_AHE is the anomalous resistance, $R_H(H_{ex})$ is the transverse Hall resistance under an external magnetic field H_{ex}. θ_H is the polar angle of the external magnetic field, which is $\theta_H = 85^\circ$ in our measurements setup. Subsequently, from the extracted parameters H_{K1}^{eff} and H_{K2} we have

$$K_1^{eff} = \frac{(H_{K1}^{eff} + 4\pi m_s)m_s}{2}, \tag{4.9}$$

and

$$K_2 = \frac{H_{K2}m_s}{4}. \tag{4.10}$$

In figure 4.16, the raw data of the Hall resistance of pristine Ta(3)/CoFeB(1) is shown as an example. The GST method is applied to analyze the Hall resistance in which the external field scans along the x-axis or the current direction (figure 4.16 b).

The raw Hall resistance is firstly normalized for the normalized magnetization m

as shown in figure 4.17. The spikes in the raw data originate from the electrical noise and environmental oscillation, which will be ignored by processing with scripts in the following fitting.

Combining with the m_s values measured in Chapter 3, the values of α are calculated, and the αH_{ex} via $1 - m^2$ is plotted as the example in figure 4.18. Then the data is linearly fitted for extracting the intercept parameter, which is the 1st order PMA effective field in equation 4.7 and 4.9, thus the 1st order effective anisotropy field K_1^{eff} can be extracted following equation 4.9.

4.2.2 Extracted 1st Effective Anisotropy K_1^{eff}

The K_1^{eff} extracted by GST method of Ta(2,3,4)/CoFeB(1) are shown in figure 4.19. The situation of K_1^{eff} is very similar to the m_s, separated into 2 groups, Ta(2)/CoFeB(1) and Ta(3,4)/CoFeB(1), and the tendencies of them are also similar. The K_1^{eff} of Ta(3,4)/CoFeB(1) almost keep constant after irradiation. In contrast, the K_1^{eff} of Ta(2)/CoFeB(1) increase to almost double in the dose $8 \times 10^{14}\,\mathrm{He}^+/\mathrm{cm}^2$ and then decrease in higher doses, showing a strong relationship with the crystallization of CoFe (110) as the m_s discussed in Chapter 3.

According to equation (4.5), we have $\zeta \propto K_{eff}^{\frac{5}{8}}$, so the K_{eff} should show the same tendency with the slope ζ if anisotropy is the dominant contribution. The compared results of 2 groups between K_1^{eff} and slope ζ are shown in figure 4.20 for Ta(2)/CoFeB(1) and figure 4.21 for Ta(3,4)/CoFeB(1).

In the group of Ta(2)/CoFeB(1), the K_1^{eff} has a similar non-monotonic tendency compared with the slope ζ in figure 4.20. Therefore, the K_1^{eff} should be a strong contribution to the change of slope ζ as expected. The irradiation on Ta(2)/CoFeB(1) increases the crystallinity of CoFe in lower doses, especially the crystallization of CoFe(110), which increases both m_s and K_{eff}. In the higher doses, the accumulated defects damage the crystallinity of CoFe(001) and reduce the m_s and K_{eff}. Such an effect modulates the domain wall motion by changing the K_{eff}. However, the pinning density n_i in equation (4.5) remains unknown, and it is possible to show a similar non-monotonic tendency as the qualitative discussion in section 4.1.3, thus the contribution from n_i can not be excluded.

In the group of Ta(3,4)/CoFeB(1), the anisotropy K_{eff} is not changed so much by the irradiation. At the same time, the slope ζ shows a strong modulation from the irradiation, which means the K_{eff} is not the dominant contribution to ζ. According to the equation (4.5), only the 3 parameters, m_s, K_{eff}, and n_i, are relative to the slope ζ, and the contribution from m_s and K_{eff} are already excluded. Therefore, the only remaining factor is the n_i, and the tendency of ζ is actually reflecting the tendency of

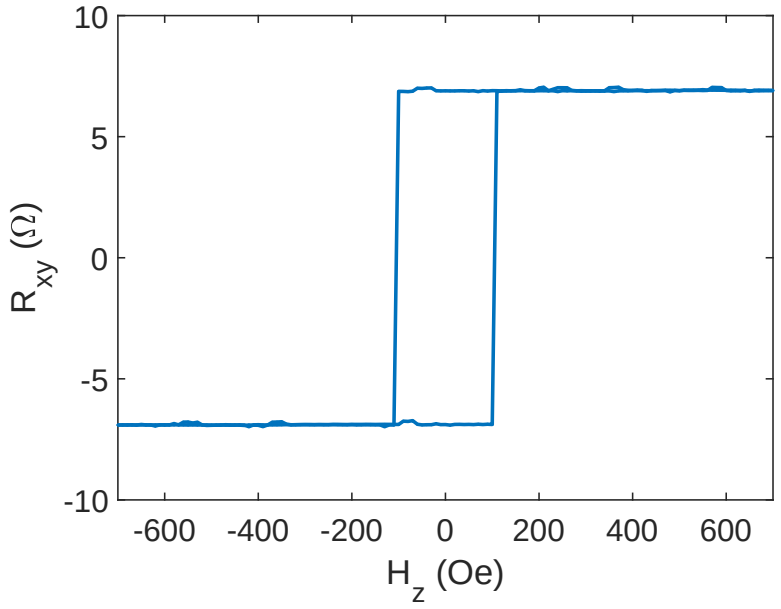

A: The Hall resistance of pristine Ta(3)/CoFeB(1). H_{ex} scanning along the out-of-plane direction.

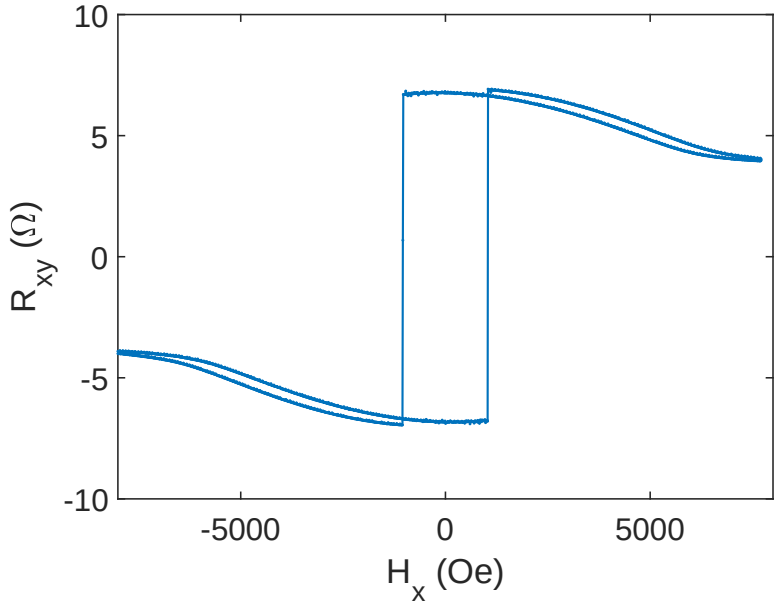

B: The Hall resistance of pristine Ta(3)/CoFeB(1). H_{ex} scanning along the x direction (current direction).

FIGURE 4.16: The Hall resistance of pristine Ta(3)/CoFeB(1) for example.

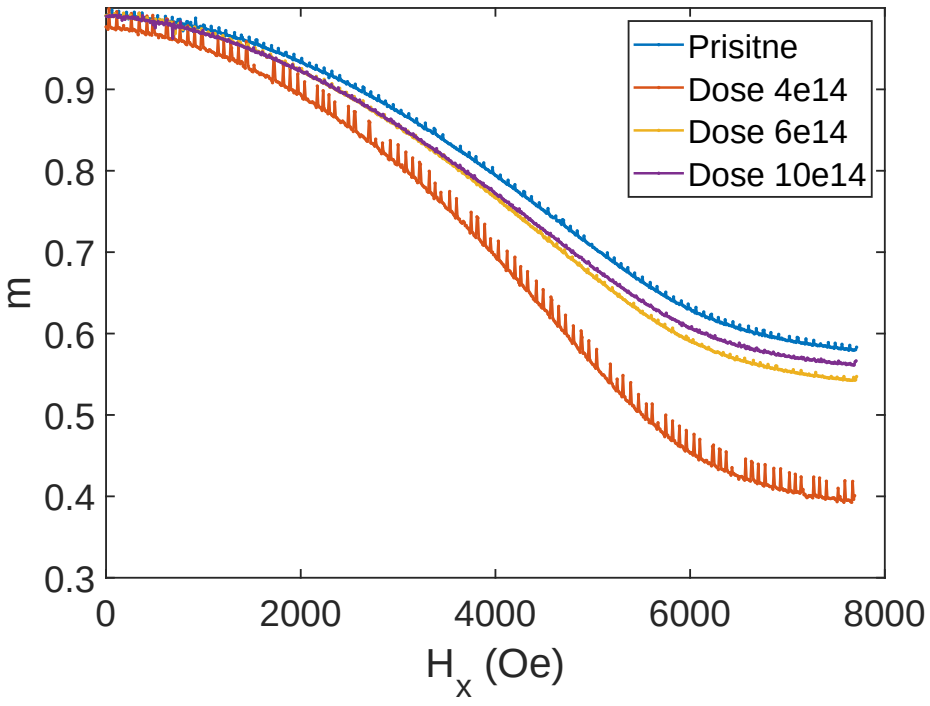

FIGURE 4.17: The normalized anomalous Hall resistance.

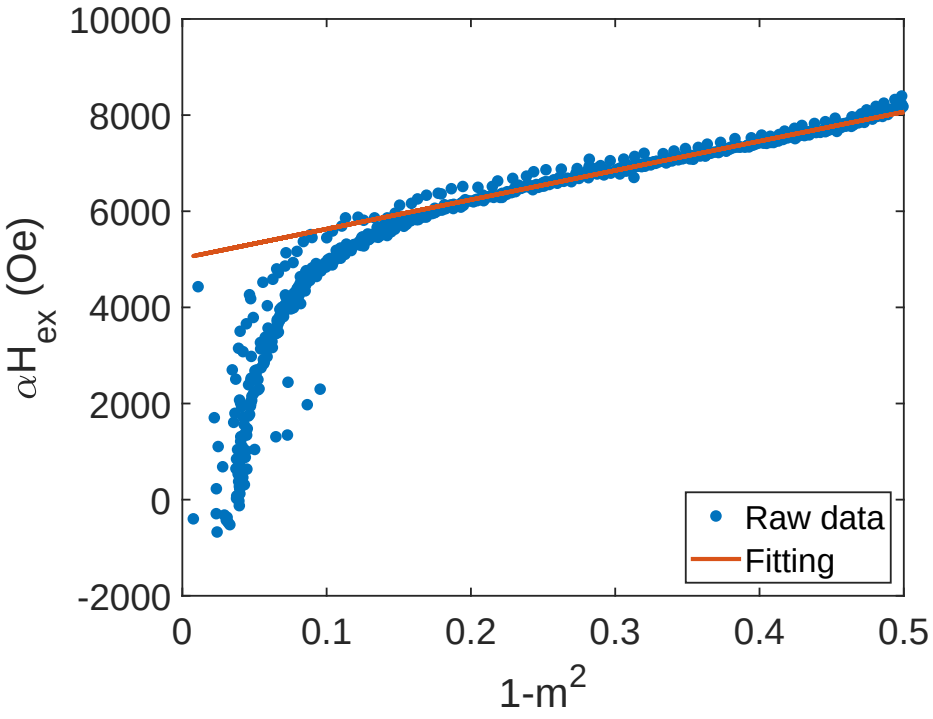

FIGURE 4.18: The converted data and the fitting result.

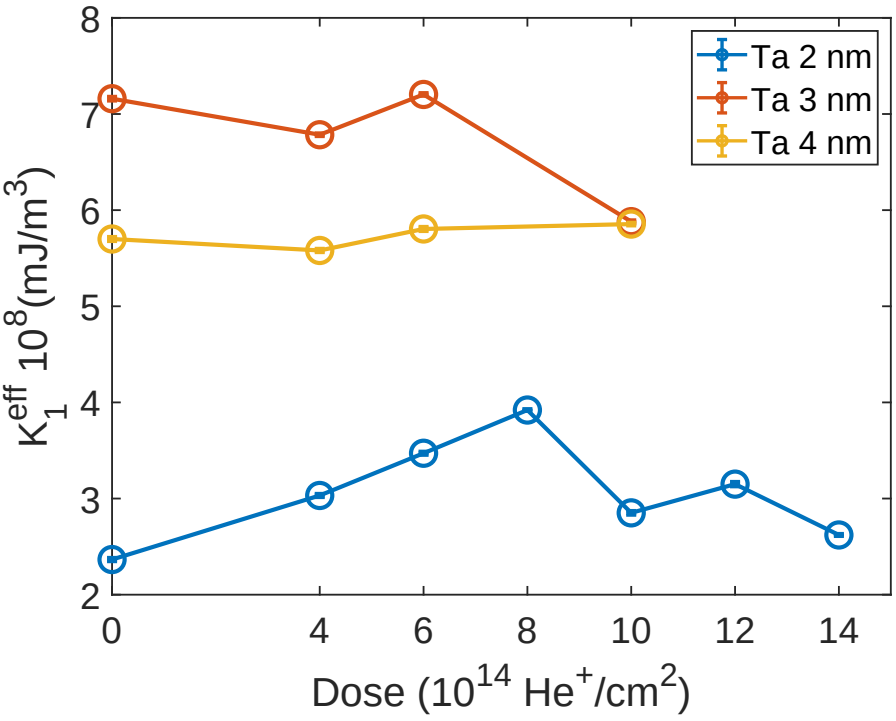

FIGURE 4.19: The K_1^{eff} extracted by GST method of Ta(2,3,4)/CoFeB(1).

n_i.

Following this deduction, we can divide the measured m_s and K_{eff} from ζ to clearly show the tendency of n_i as shown in figure 4.22. The values of the n_i in figure 4.22 are not important because the constant factors of Ta(3)/CoFeB(1) and Ta(4)/CoFeB(1) may be different. However, the results show that the He^+ ion irradiation has a strong effect on the modulation of the pinning density n_i of Ta(3,4)/CoFeB(1). Especially in dose $6 \times 10^{14}\,He^+/cm^2$, irradiation significantly promotes the domain wall motion by reducing the pinning density.

4.3 Conclusion

In this chapter, the velocity of domain wall motion in Ta/CoFeB is measured, and the slope ζ in the logarithm relationship is extracted. According to the model of the domain wall motion in the creep regime, the slope ζ describes the controllability of the DW velocity by a magnetic field, and a lower value of slope ζ is more satisfying because the demand to an external magnetic field or effective field is reduced. Furthermore, more information on the landscape of the pinning barrier, such as the pinning energy U_c and the depinning field H_{dep}, can be extracted from the slope ζ. Therefore, the slope ζ of materials is directly relative to the performance of DW-based devices, and as expected, the thinner Ta(2)/CoFeB(1) and thicker Ta(3)/CoFeB(1) show opposite dependence on the irradiation dose, especially the Ta(3)/CoFeB(1), whose ζ is significantly reduced in the dose $6 \times 10^{14}\,\mathrm{He}^{+}/\mathrm{cm}^2$, meaning the superiority in DW-based device application within the three thicknesses.

Subsequently, According to the proportional or the inverse proportional relationship on the K_{eff} and m_s, the contribution of them to ζ is determined or excluded, which is summarized in figure 4.23. In the case of the thicker Ta(3,4)/CoFeB(1) samples, because the almost constant K_{eff} and m_s are contradictory with the tendency of the slope ζ, meaning that K_{eff} or m_s can not be the reason of the change of ζ, the modification on the pinning density n_i is confirmed to be the dominant contribution, sharing the same tendency with the slope ζ. Therefore, the optimal point in the ζ of Ta(3)/CoFeB(1) is also the optimal point in the pinning density n_i. The large decrease of n_i in dose $6 \times 10^{14}\,\mathrm{He}^{+}/\mathrm{cm}^2$ demonstrated the improvement on defects by the He^+ ion irradiation. On the other hand, the tendency of the slope ζ of Ta(2)/CoFeB(1) is the same as the tendency of the effective magnetic anisotropy K_{eff}, meaning that the K_{eff} should be the dominant contribution to the change of the slope ζ after irradiation. However, the pinning density n_i can not be determined in this case, so the contribution from n_i can not be excluded.

In conclusion, the performance on domain wall motion of He^+ irradiated Ta/CoFeB

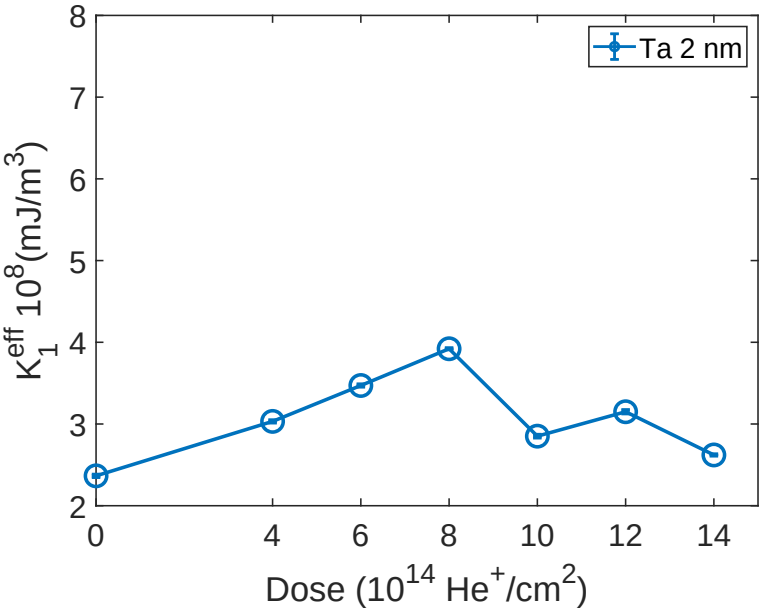

A: The K_1^{eff} of Ta(2)/CoFeB(1).

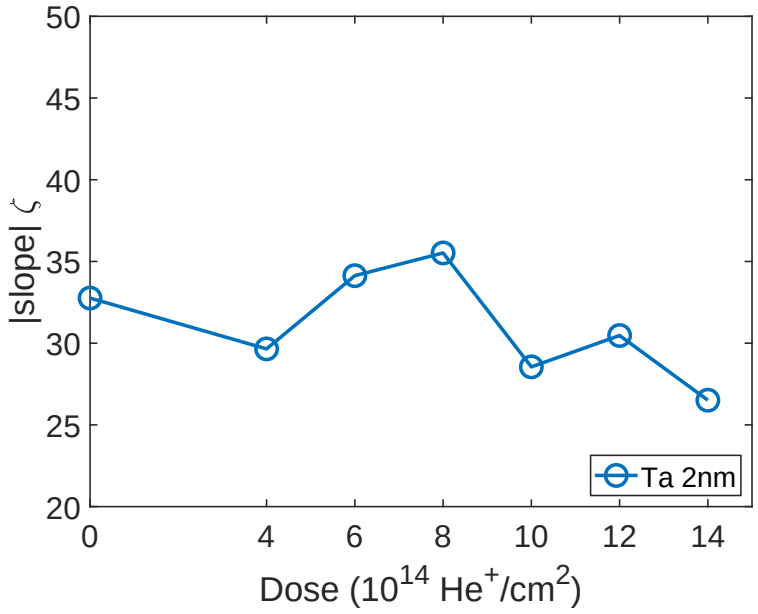

B: The slope ζ of Ta(2)/CoFeB(1).

FIGURE 4.20: The similar tendencies of (a) K_1^{eff} and (b) slope ζ of Ta(2)/CoFeB(1).

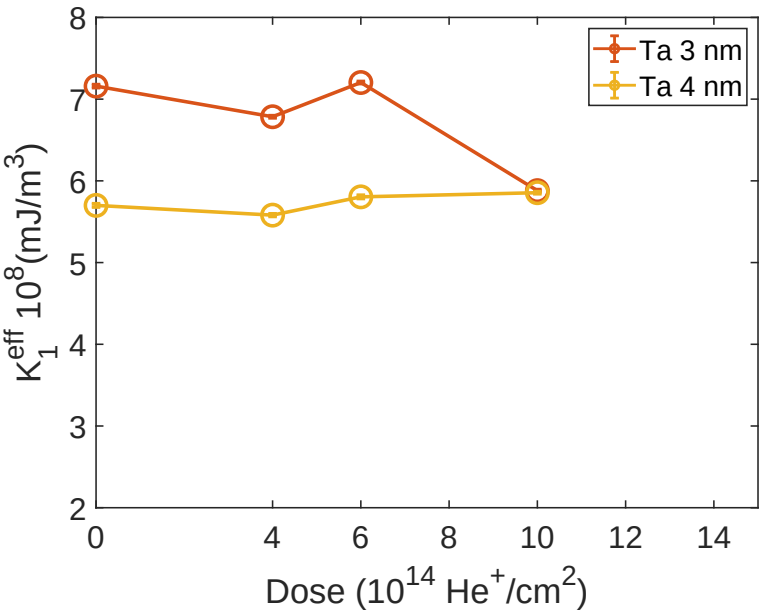

A: The K_1^{eff} of Ta(3,4)/CoFeB(1).

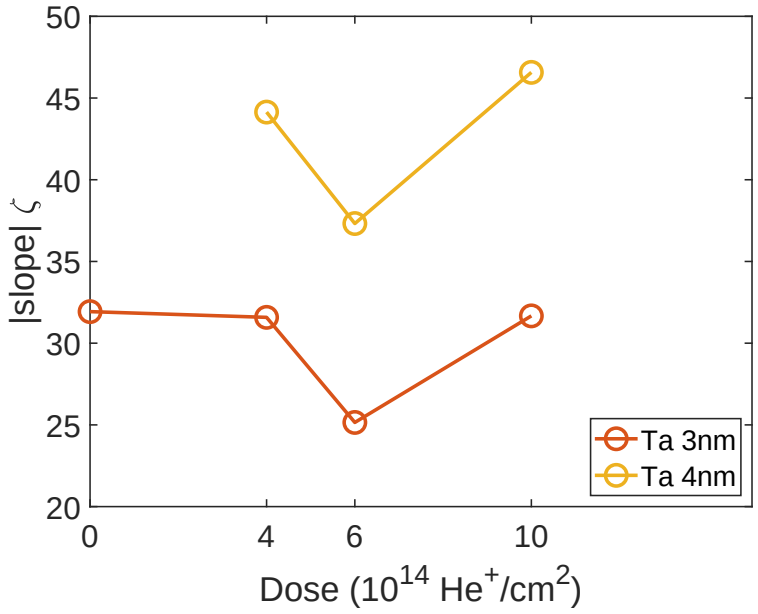

B: The slope ζ of Ta(3,4)/CoFeB(1).

FIGURE 4.21: The irrelevant tendencies of (a) K_1^{eff} and (b) slope ζ of Ta(3,4)/CoFeB(1).

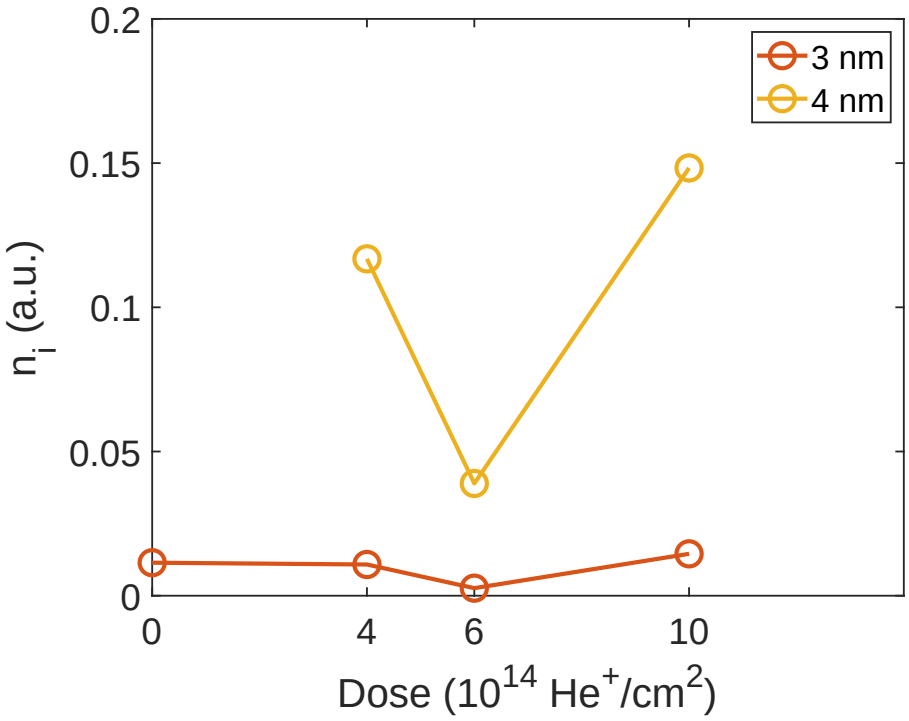

FIGURE 4.22: The tendency of extracted pinning density n_i of Ta(3,4)/CoFeB(1).

is measured by Kerr microscopy, the Ta(3)/CoFeB(1) irradiated by the dose $6 \times 10^{14}\,\mathrm{He}^{+}/\mathrm{cm}^{2}$ is the optimal point. By excluding the contribution from the change of magnetic properties, the dominant contribution from irradiation to the improvement of domain wall motion is determined.

Thickness	m_s	K_e	n_i
2	×	◯	▲
3	×	×	◯
4	×	×	◯

FIGURE 4.23: The summary table of the contribution to the slope ζ.

The crosses mean the parameters are confirmed not dominant, the circles mean the dominant contribution, and the solid triangle means the possible unknown contribution. The thickness notes the thicknesses of Ta layers.

Chapter 5

The Effect of He+ Irradiation on Spin-Orbit Torque

In this chapter, we investigate the spin-orbit torque (SOT) property of irradiated Ta/CoFeB thin films. In the previous chapters, the magnetic properties and domain wall dynamics of the irradiated samples are discussed and are consistent with other studies. However, it lacked research on the He^+ ion irradiation on the SOT property. Here, we measured the SOT by harmonic Hall measurements and demonstrated that the thickness of the Ta layer is essential to the SOT modulation by the He^+ ion irradiation.

5.1 Measurement Method

As a typical structure widely studied by many researchers, thin films of Ta/CoFeB with PMA properties are reported to have a strong spin Hall effect (SHE), Rashba effect, and large spin Hall angle,[47, 48, 49, 50, 51] showing an attractive potential in spintronics devices application. Among many different measurement methods for investigating the spin-orbit torque (SOT) property, the harmonic Hall analysis is a powerful tool to probe the current-induced SOT by measuring the magnetization dynamics because of its precision and convenience (it only needs a low-frequency AC source).

In order to investigate the SOT property of He^+ ion irradiated Ta/CoFeB thin films, harmonic measurements are performed on the samples.[52, 47, 53] In a system with inversion asymmetry like a ferromagnet/normal metal (FM/NM) bilayer system, the coupling between the spin and orbital degrees of freedom generates strong SOT.[52] The SOT originates from the structure asymmetry SHE or interface asymmetry Dresselhaus-Rashba effect. The SHE refers to the spin-dependent deviation of the electron trajectory, contributed by the scattering (skew jump and side jump) and the intrinsic mechanisms[54, 55], transferring a damping-like torque into the magnetization of the ferromagnet layer. The Rashba effect is an interface effect, leading to the spin polarization of the conduction electrons at the interface of a material with broken inversion symmetry.[56, 57] The SOT property of material has been studied extensively for its significant advantages in spintronic device applications.

5.1.1 Spin-orbit Torque Driven Harmonic signals

The harmonic Hall measurements need a Hall bar structure, which is shown in figure 5.1 When an AC current is applied in a device with a Hall bar structure, periodic oscillations of the magnetization are generated due to the SOT, creating a periodic oscillating transverse voltage signal:

$$V_{xy}(t) = R_{xy}(t) I_0 sin(\omega t), \tag{5.1}$$

where $R_{xy}(t)$ is the oscillating transverse resistance or Hall resistance, $I_0 sin(\omega t)$ is the oscillating AC current.

When an external magnetic field is applied, the Hall resistance is affected by both the external field and SOT, thus we have

$$R_{xy}(t) = R(B_{ex} + B_I(t)), \tag{5.2}$$

where the $B_I(t)$ means the current-induced effective field, including damping-like effective field and field-like effective field, which generates damping-like (DL) torque and field-like (FL) torque on the magnetization.

Since B_{ex} is a constant magnetic field compared with the oscillating field $B_I(t)$, $R(t)$ can be approximately expansed as

$$R_{xy}(t) \approx R_{xy}(B_{ex}) + \frac{dR}{dB_I} \cdot B_I sin(\omega t). \tag{5.3}$$

Combining the equation (5.1) and (5.3), we have

$$V_{xy}(t) \approx I_0[R_0 + R_{xy}^{1\omega} sin(\omega t) + R_{xy}^{2\omega} cos(2\omega t)], \tag{5.4}$$

where V_{xy} is the transverse Hall voltage, $R_{xy}^{1\omega}$ and $R_{xy}^{2\omega}$ are the 1st and 2nd order harmonic resistance, respectively.

The $R_{xy}^{1\omega}$ equals the Hall signal in the case of DC measurements, and we have

$$R_{xy}^{1\omega} = R_{AHE} cos\theta + R_{PHE} sin^2\theta sin(2\varphi), \tag{5.5}$$

where R_{PHE} is the planar Hall effect resistance, θ is the polar angle and φ is the azimuthal angle of the magnetization vector.

As for the $R_{xy}^{2\omega}$ we have

$$R_{xy}^{2\omega} = (R_{AHE} - 2R_{PHE}cos\theta sin(2\varphi))\frac{dcos\theta}{dB_I} \cdot B_I + R_{PHE}sin^2\theta\frac{dsin(2\varphi)}{dB_I} \cdot B_I, \tag{5.6}$$

where B_I is the current induced effective field.

In the case that magnetic field sweeping along the x axis or y axis, combining with the equation (5.4), (5.5), and (5.6), we have $R_{xy}^0 = \frac{1}{2}\frac{dR_{xy}}{dB_I} \cdot B_I$, $R_{xy}^{1\omega} = R_{xy}(B_{ex})$, and $R_{xy}^{2\omega} = -\frac{1}{2}\frac{dR_{xy}^{1\omega}}{dB_I} \cdot B_I$.

Compared with the steady DC measurements, the harmonic signal $R_{xy}^{2\omega}$ is a dynamic signal, including both the current-induced effects such as H_{DL}, H_{FL}, and the thermoelectric effects such as the anomalous Nernst effect (ANE), which will be eliminated in the analysis.

5.1.2 Measurement Setup

The harmonic measurements are performed on the same Hall bar device with the anisotropy measurements in Chapter 4 for reducing fabrication procedures and error.

The measurements are performed with a Wave Factory 1941 as the AC current source, supplying an AC current with 13 Hz, the amplitude is adjusted to keep the same current density in all samples with different thicknesses. The applied current I_0 is determined by the voltage of the reference resistor V_{ref}, measured by a Keysight 34411A $6_{1/2}$ Digit Multimeter real-time. The harmonic signal of the Hall bar is measured simultaneously by 2 Stanford Research Systems SR830 lock-in amplifiers. The samples are slightly tilted out-of-plane ($\approx 5^\circ$).

Take the data of pristine Ta(2)/CoFeB(1) as an example to show the analysis procedures. As discussed in the last subsection, in PMA samples, the first harmonic signal is equivalent to the anomalous Hall resistance in DC measurements. In the range of sweeping field around zero, the signal $R_{xy}^{1\omega}$ can be fitted by a quadratic formula as shown in figure 5.3, where the H_ex sweeps in a x direction and b y direction.

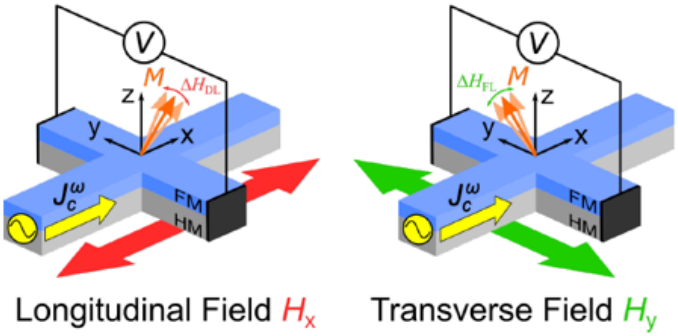

FIGURE 5.1: The diagram of a harmonic Hall measurements setup for FM/NM thin films with PMA.

J_C^ω is an AC current at frequency ω, causing the magnetization M to oscillate due to SOT. The external magnetic field sweeps longitudinally (H_x) or transversely (H_y), corresponding to the signal of the damping-like effective field H_{DL} (left) and the field-like effective field H_{FL} (right), respectively. Adapted from Ref. [53]

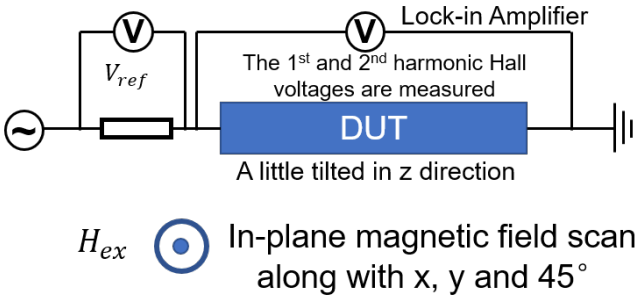

FIGURE 5.2: The electrical circuit of the harmonic measurement setup.

The second harmonic signal as shown in figure 5.4, where the $H_e x$ sweeps in a x direction and b y direction. The second harmonic signal is a dynamic signal originating from the oscillating magnetization by SOT. Therefore, the scanning direction in figure 5.4 a x-axis and b y-axis correspond to the longitudinal and transverse effective field, respectively. In the range of sweeping field around zero, the signal $R_{xy}^{2\omega}$ can be fitted by a linear formula. In the case of the x-scan, the positive part of raw data (corresponding to the up magnetization M^+) and the negative part of raw data (corresponding to the down magnetization M^-) are parallel. On the other hand, in the case of the y-scan, the slopes of the positive part and the negative part are opposite.

As per the previous discussion, the thermoelectric effect also contributes to the second harmonic signal, which is the anomalous Nernst effect (ANE). In our system, ANE shows a hysteresis in figure 5.4, and the values remain constant in the upper and lower branches, respectively. Therefore, we can directly subtract the intercept from both branches to remove the ANE contribution.

In addition, after removing the contribution from ANE, the mixing contribution to the second harmonic signal from anomalous Hall effect (AHE) and planar Hall effect (PHE) should be considered. The mixing factor depends on the ratio between the AHE and PHE, which we define as $\xi = \frac{\Delta R_{PHE}}{\Delta R_{AHE}}$. With the method from Ref. [58], the value of ξ can be determined.

In the first harmonic signal, R_{xy} follows the $sin(2\varphi)$ dependence on the azimuthal angle, thus it is eliminated at $\varphi = 0^\circ$ and maximized at $\varphi = 45^\circ$, while the AHE contribution remains unchanged. The difference can be written as

$$\Delta R_{xy} = R_{xy}^{45} - R_{xy}^{0} = \frac{1}{2}\Delta R_{PHE} sin^2\theta. \tag{5.7}$$

After normalizing the R_{xy}^{45} and R_{xy}^{0}, we have the normalized version of equation (5.7) as

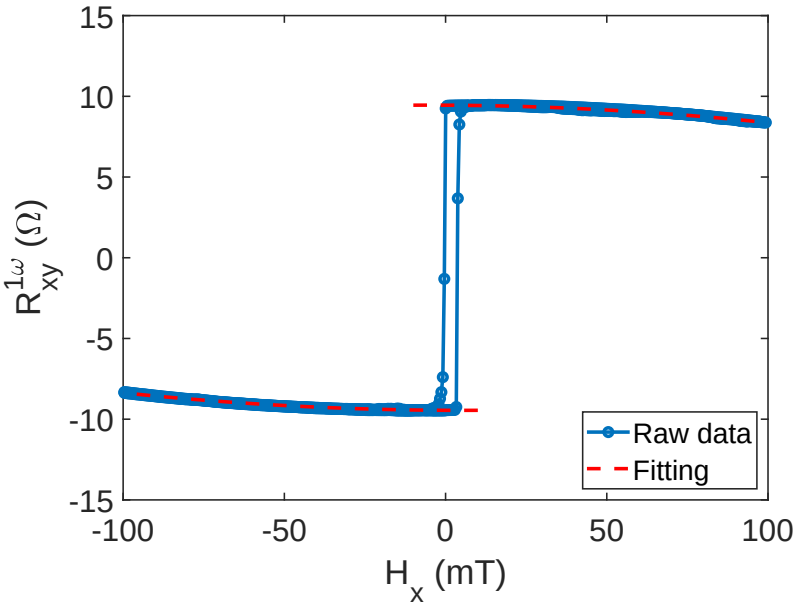

A: x-scan.

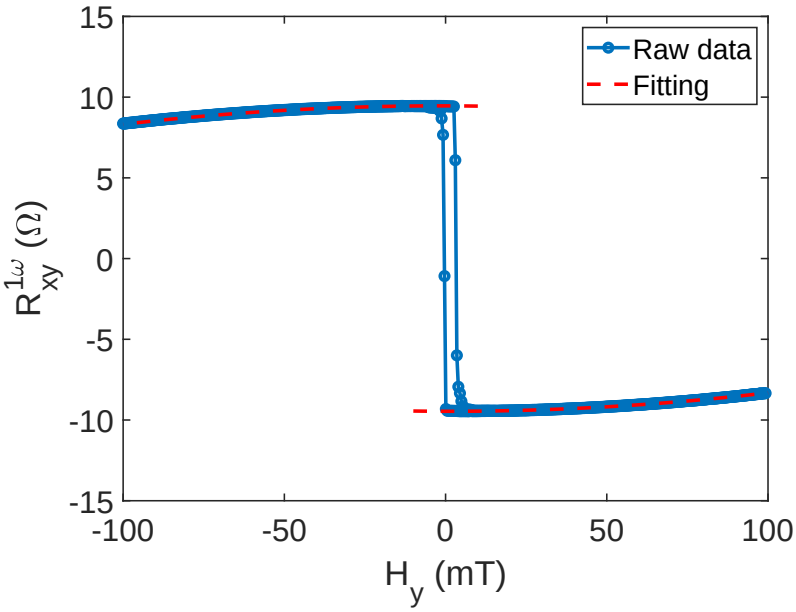

B: y-scan.

FIGURE 5.3: The first harmonic Hall resistance of pristine Ta(2)/CoFeB(1) sample.

(a) Magnetic field sweeping along the x-axis, (b) magnetic field sweeping along the y-axis. The red dotted line is the quadratic fitting results.

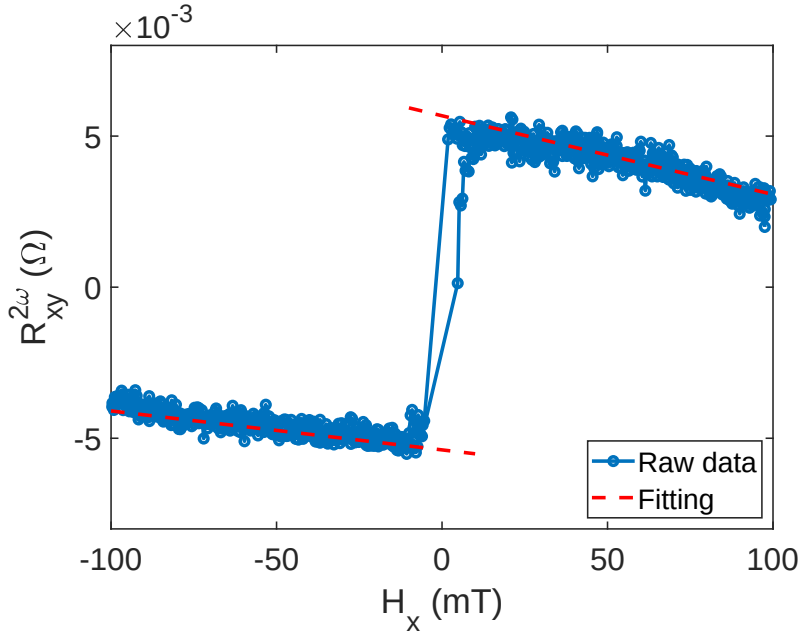

A: x-scan.

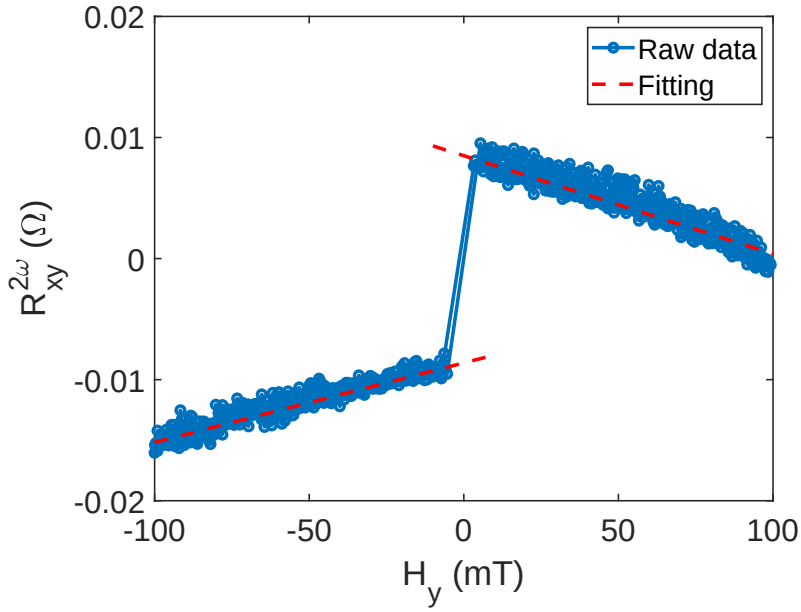

B: y-scan.

FIGURE 5.4: The second harmonic Hall resistance of pristine Ta(2)/CoFeB(1) sample

(a) Magnetic field sweeping along the x-axis, (b) magnetic field sweeping along the y-axis. The red dotted line is the linear fitting results.

$$\Delta\tilde{R}_{xy} = \tilde{R}^{45}_{xy} - \tilde{R}^{0}_{xy} = (cos\theta + \frac{\Delta R_{PHE}}{\Delta R_{AHE}} sin^2\theta) - cos\theta = \frac{\Delta R_{PHE}}{\Delta R_{AHE}}[1 - (\tilde{R}^{0}_{xy})^2]. \tag{5.8}$$

The normalized $R^{1\omega}_{xy}$ of the data at $\varphi = 0°$ and $\varphi = 45°$ are shown in figure 5.5, and the plot of $\Delta\tilde{R}_{xy}$ vs $(1 - (\tilde{R}^{0}_{xy})^2)$ is shown in figure 5.6, showing a good consistence with the linear fitting. From the linear fitting, we can obtain the slope of the fitting curve, which is the ratio $\xi = \frac{\Delta R_{PHE}}{\Delta R_{AHE}}$ in equation (5.8).

According to the discussion in the previous subsection, the longitudinal effective field (B_x) and the transverse effective field (B_y) can be written as [47]

$$B_x = 2\frac{\frac{\partial R^{2\omega}_{xy}}{\partial H_x}}{\frac{\partial^2 R^{1\omega}_{xy}}{\partial H_x^2}}, \tag{5.9}$$

and

$$B_y = 2\frac{\frac{\partial R^{2\omega}_{xy}}{\partial H_y}}{\frac{\partial^2 R^{1\omega}_{xy}}{\partial H_y^2}}. \tag{5.10}$$

In considering the contribution from PHE, we can correct them from the B_x and B_y to obtain the damping-like effective field (H_{DL}) and field-like effective field (H_{FL})

$$H_{DL} = \frac{B_x + 2\xi B_y}{1 - 4\xi^2}, \tag{5.11}$$

and

$$H_{FL} = \frac{B_y + 2\xi B_x}{1 - 4\xi^2}. \tag{5.12}$$

Furthermore, the spin Hall angle θ_{SH} can be calculated [59, 50] with the equations

$$\frac{H_{DL}}{J} = \frac{H^{\infty}_{DL}}{J}(1 - sech(\frac{t_N}{\lambda})), \tag{5.13}$$

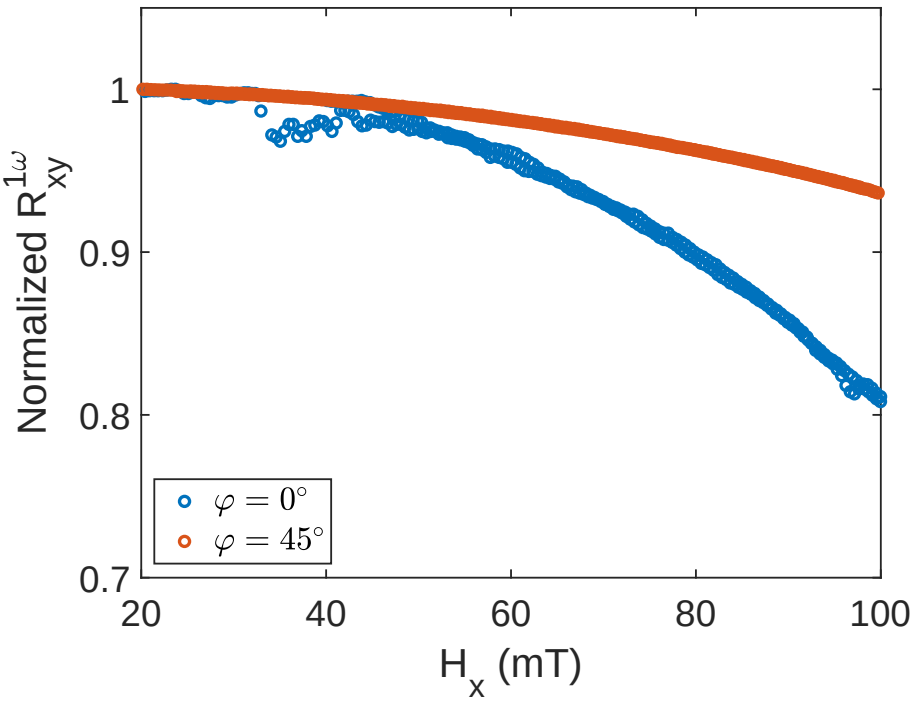

FIGURE 5.5: The normalized first harmonic Hall resistance at $\varphi = 0°$ and $\varphi = 45°$.

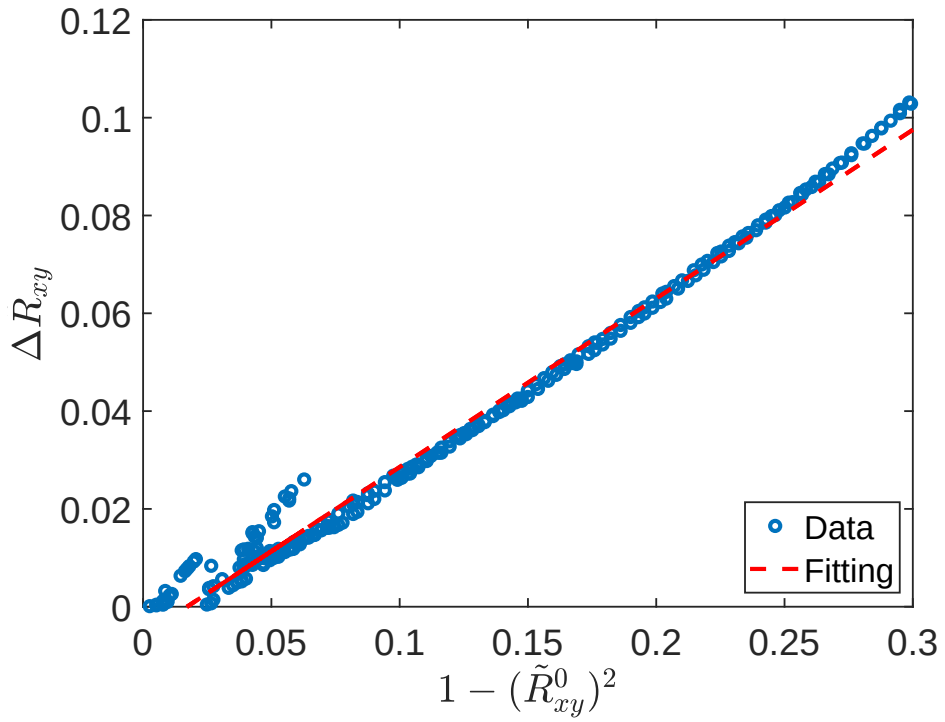

FIGURE 5.6: The plot of $\Delta\tilde{R}_{xy}$ vs $(1-(\tilde{R}^0_{xy})^2)$.

where the J is the current density, t_N is the thickness of the Ta layer, λ is the spin diffusion length of Ta, and $\lambda = 0.33\,\mathrm{nm}$ according to the previous research on the materials grown by the same way[50], and

$$\theta_{SH} = \frac{2em_s t_F}{\hbar}\frac{H_{DL}^{\infty}}{J}, \tag{5.14}$$

where the e is the elementary charge, m_s is the saturation magnetization, t_F is the thickness of ferromagnetic layer, and $\hbar$ is the reduced Planck constant.

5.2 SOT Property of Irradiated Samples

Following the methods described in the last section, the SOT effective field H_{DL} and H_{FL} are calculated. The results of Ta(2)/CoFeB(1) are shown in figure 5.7.

From figure 5.7 a and b we can see that both the H_{DL} and H_{FL} share a very similar tendency, both are decreasing from pristine until the dose $8 \times 10^{14}\,\mathrm{He}^{+}/\mathrm{cm}^{2}$, and then increase again in higher doses. The H_{DL} comes from the SHE in bulk, which is very relative to the scattering or defects because of the skew-jump and side-jump mechanism.[54, 55, 60] Therefore, we measured the resistivity ρ of all samples as shown in figure 5.9.

As expected, the ρ of Ta(2)/CoFeB(1) is the highest within all the thicknesses. Compared with the resistivity of Ta(3,4)/CoFeB(1), which changes only a little after irradiation, the resistivity of Ta(2)/CoFeB(1) fluctuates enormously depending on the irradiation doses (around $\pm 15\,\%$), showing a similar non-monotonic tendency with the minimum at dose $8 \times 10^{14}\,\mathrm{He}^{+}/\mathrm{cm}^{2}$ with H_{DL}. There are two possible reasons: first, the irradiation increases the crystallinity of both CoFe (001) and CoFe (110) in lower doses, as discussed in Chapter 3, which leads to the lower resistivity of the CoFeB layer and thus stronger current shutting effect. If the current flowing through the Ta layer is smaller than expected, the effective field would be smaller. When the dose increases and the crystallinity of CoFe (001) becomes damaged, the shutting effect turns weaker again. Thus, we have a stronger effective field in higher doses. Second, the lower doses of He^{+} ion irradiation can rearrange the atoms, which helps reduce defects in low doses, and consequently, the SHE becomes weaker. In the higher doses, the accumulated defects increase and enhance the SHE again, leading to higher H_{DL}. More investigation is needed to figure out the reasons. Besides, for directly comparing the charge-spin conversion efficiency, the spin Hall angle θ_{SH} is calculated as figure 5.8, which shows the same tendency with H_{DL}.

Compared with the slope ζ extracted from the domain wall motion, which is shown in figure 5.10, which shows the domain wall dynamic properties, we can

see the Ta(2)/CoFeB(1) has the lowest effective field and worst domain wall motion in the irradiation dose $8 \times 10^{14}\,\mathrm{He}^{+}/\mathrm{cm}^{2}$, and the m_s of it is easily changed by irradiation. In general, the disadvantages overcome the advantages a lot in this structure. Therefore the Ta(2)/CoFeB(1) is not suitable for the application of He^{+} ion irradiation technology.

In the group of Ta(3,4)/CoFeB(1) samples, the situations are different from the Ta(2)/CoFeB(1). As shown in figure 5.11, the SOT properties show very different tendencies. Especially in the case of the SOT of Ta(3)/CoFeB(1), which offers a strong increase in the dose $6 \times 10^{14}\,\mathrm{He}^{+}/\mathrm{cm}^{2}$, both H_{DL} and H_{FL} are increased more than two times. At the same time, we can check the results of slope ζ in figure 5.12, Ta(3)/CoFeB(1) also shows the best performance in the dose $6 \times 10^{14}\,\mathrm{He}^{+}/\mathrm{cm}^{2}$, which means the dose $6 \times 10^{14}\,\mathrm{He}^{+}/\mathrm{cm}^{2}$ is a sweet spot of Ta(3)/CoFeB(1) satisfying the requirement in all the magnetic properties, domain wall dynamics, and SOT property. In general, the performance of Ta(3)/CoFeB(1) is significantly improved in domain wall motion, and SOT property by He^{+} ion irradiation, showing completely different results from the Ta(2)/CoFeB(1), and the magnetic property remain stable at the same time.

On the other hand, although the Ta(4)/CoFeB(1) is as good as Ta(3)/CoFeB(1) in magnetic properties and similarly good in domain wall dynamics, its tendency of SOT property via the irradiation doses seems to be shifted to higher doses. Especially in the H_{DL} shown in figure 5.11 a, where the H_{DL} of Ta(3)/CoFeB(1) reaches the maximum in dose $6 \times 10^{14}\,\mathrm{He}^{+}/\mathrm{cm}^{2}$, and then decrease. However, the H_{DL} of Ta(4)/CoFeB(1) just starts to increase from $6 \times 10^{14}\,\mathrm{He}^{+}/\mathrm{cm}^{2}$, and reach the similar value in dose $10 \times 10^{14}\,\mathrm{He}^{+}/\mathrm{cm}^{2}$. Even if it reached a higher H_{DL} with much higher doses, the slope ζ in figure 5.12 would become much higher and worse, which means the effect on SOT property doesn't match the effect on domain wall dynamics.

Therefore, according to the above discussion, the effects of He^{+} ion irradiation are highly relative to the thickness of the sample and show strong potential on the spintronic device application of Ta/CoFeB thin films. Even only the difference of 1 nm,

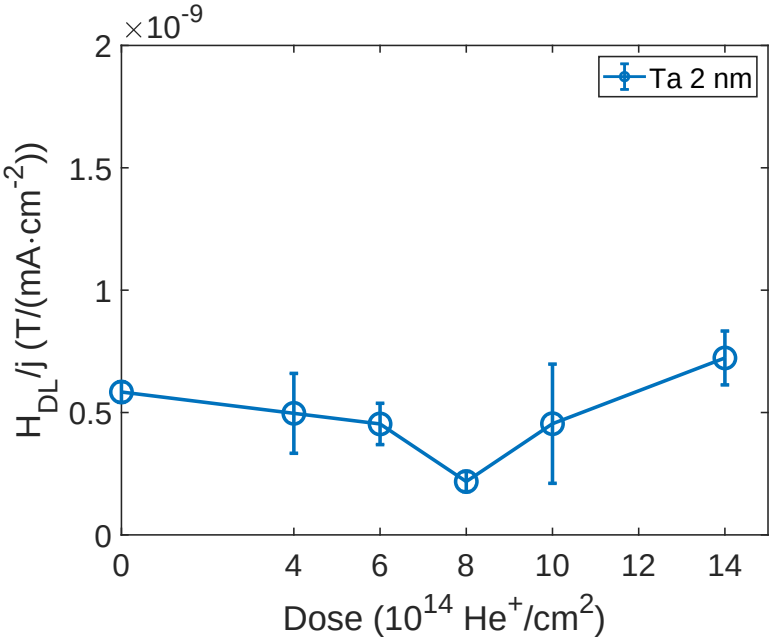

A: H_{DL} of Ta(2)/CoFeB(1).

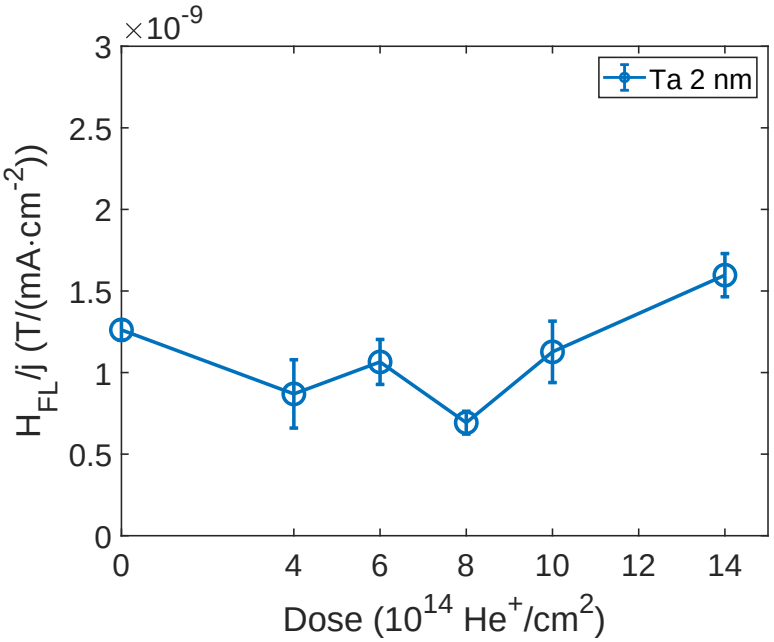

B: H_{FL} of Ta(2)/CoFeB(1).

FIGURE 5.7: The SOT of Ta(2)/CoFeB(1).

(a) The damping-like field H_{DL} and (b) the field-like field H_{FL} of Ta(2)/CoFeB(1).

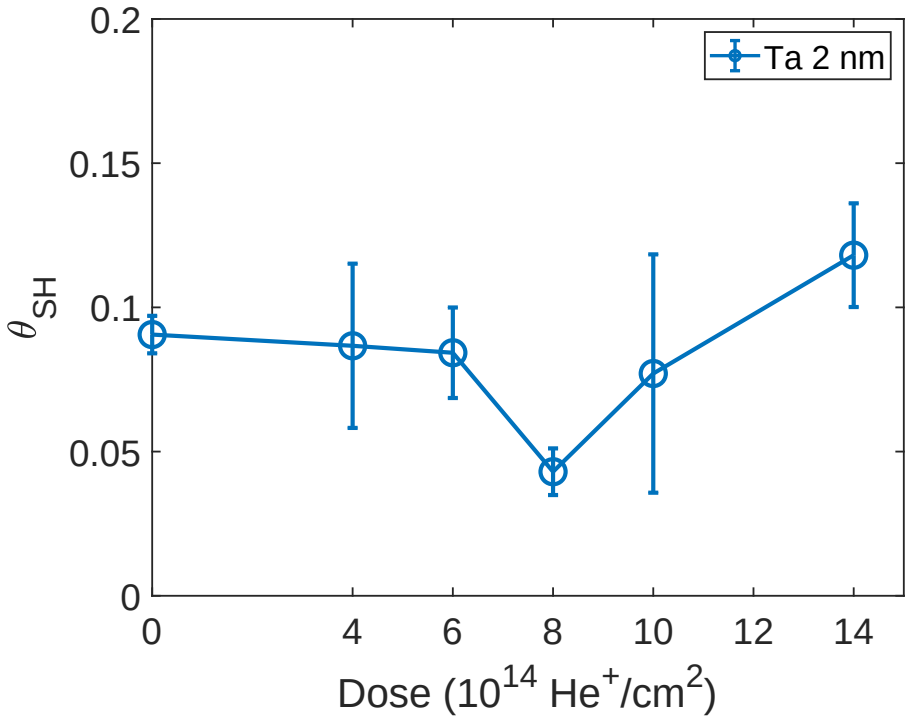

FIGURE 5.8: The spin Hall angle θ_{SH} of Ta(2)/CoFeB(1) samples.

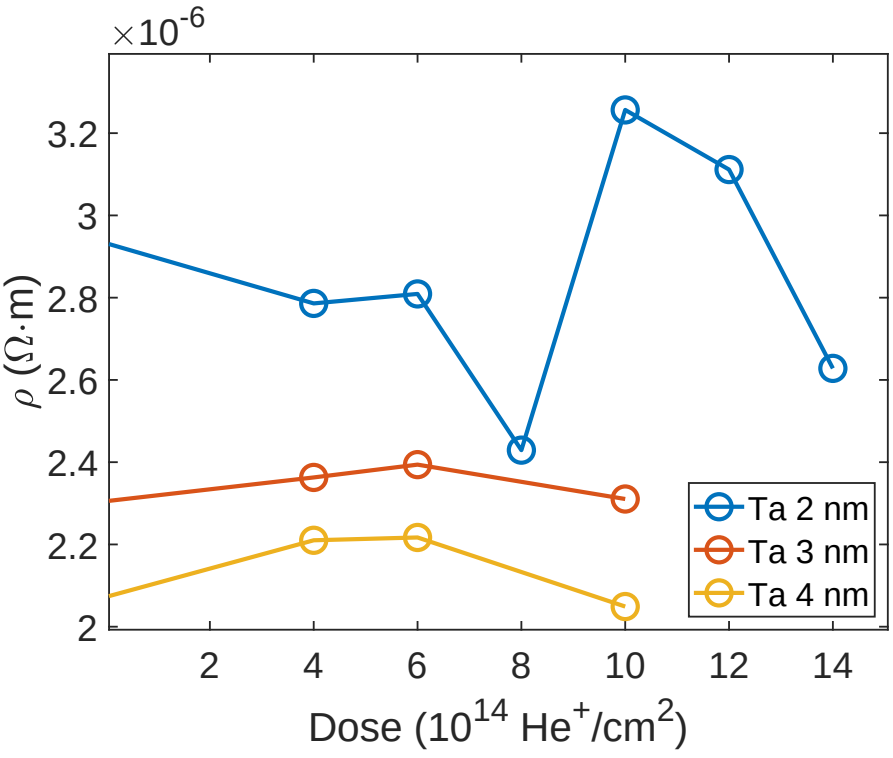

FIGURE 5.9: The resistivity for Ta(2,3,4)/CoFeB(1) samples, measured by the same Hall bar structure with DC current.

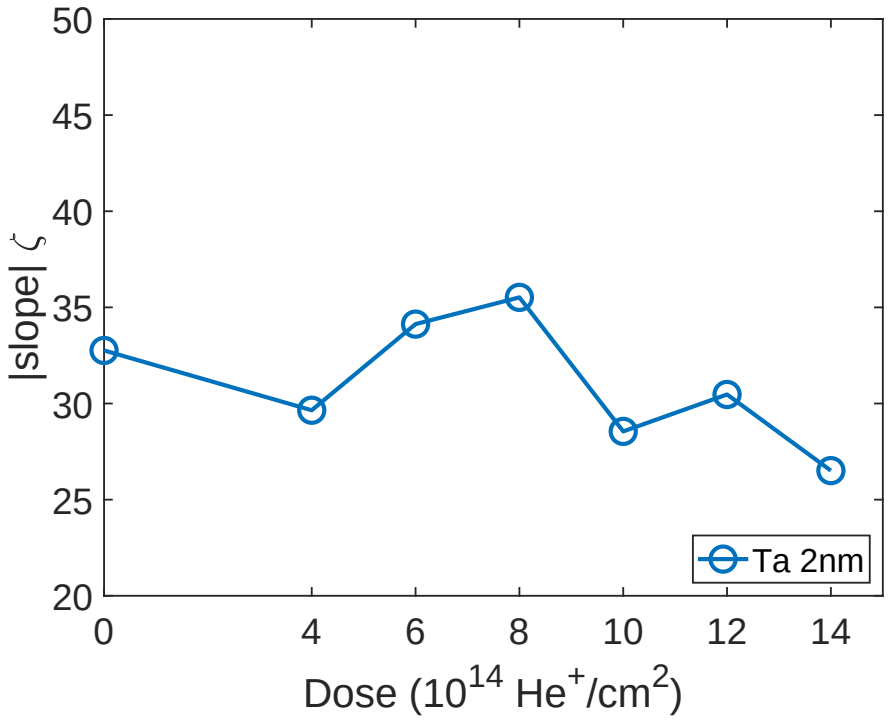

FIGURE 5.10: The slope ζ of Ta(2)/CoFeB(1) from Chapter 4.

the effects may be completely different (Ta(2)/CoFeB(1) and Ta(3,4)/CoFeB(1)), or miss the sweet spot (Ta(3)/CoFeB(1) and Ta(4)/CoFeB(1)).

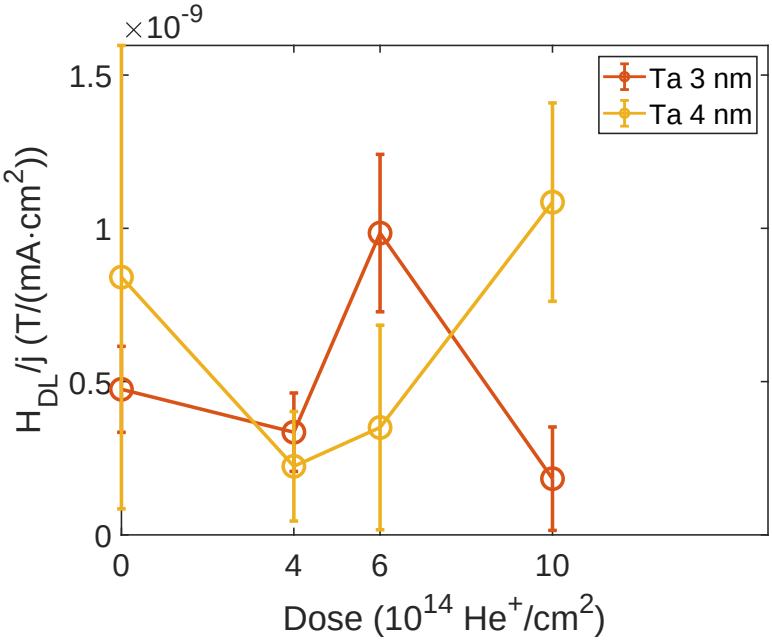

A: H_{DL} of Ta(3,4)/CoFeB(1).

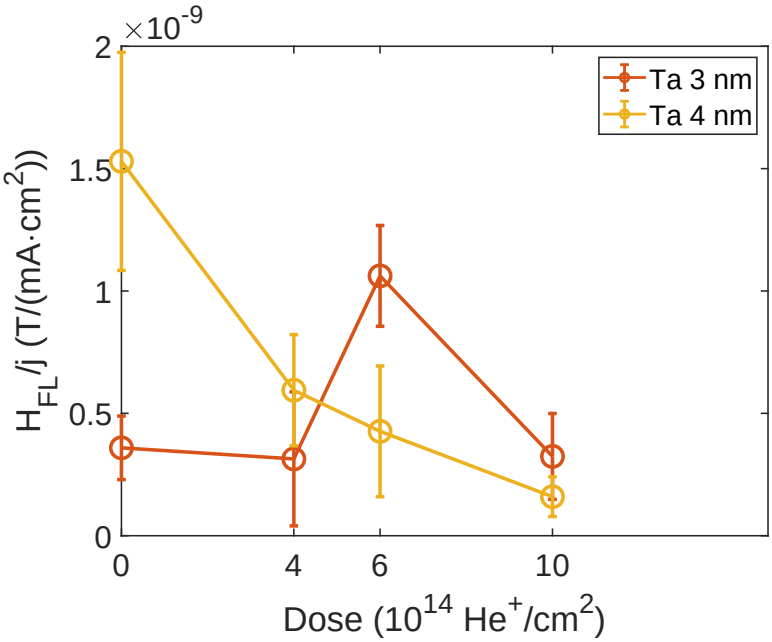

B: H_{FL} of Ta(3,4)/CoFeB(1).

FIGURE 5.11: The SOT of Ta(3,4)/CoFeB(1).

(a) The damping-like field H_{DL} and (b) the field-like field H_{FL} of Ta(3,4)/CoFeB(1).

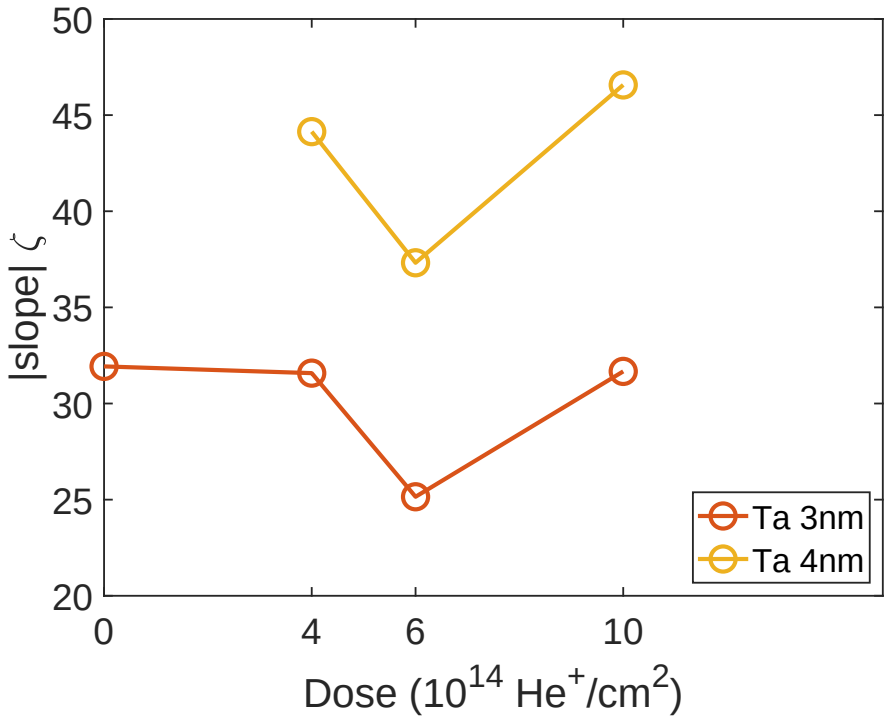

FIGURE 5.12: The slope ζ of Ta(3,4)/CoFeB(1) from Chapter 4.

5.3 Conclusion

In the previous sections, the SOT of irradiated Ta/CoFeB thin films is well investigated. In the demands for the device application, the higher SOT of materials is critical and pleasing because the higher SOT can reduce the switching current, increase the efficiency, and reduce Joule heat. As discussed in Chapter 3 and 4, the samples should be divided into two groups, the thinner Ta(2)/CoFeB(1) and the thicker Ta(3,4)/CoFeB(1). Here, we summarized the conclusions combined with the previous results on the magnetic properties and domain wall dynamics.

In the group of Ta(2)/CoFeB(1) thin films, the summary of results is shown in figure 5.13. In all properties, Ta(2)/CoFeB(1) are strongly modulated by the He^+ ion irradiation, showing a very relative tendency and getting the worst point in dose $8 \times 10^{14}\,He^+/cm^2$. The reason for those changes is demonstrated to be the crystallinity changed by irradiation. Such effects show that the structure Ta(2)/CoFeB(1) is unsuitable for He^+ ion irradiation in the device application.

In the group of Ta(3,4)/CoFeB(1), those samples have similar results in the magnetic properties and domain wall dynamics, but they are slightly different in the SOT property. As shown in figure 5.14, the Ta(3)/CoFeB(1) has stable m_s and the best result in both SOT and ζ in irradiation dose $6 \times 10^{14}\,He^+/cm^2$, which means that would be a sweet spot for the He^+ ion irradiation.

However, in the case of Ta(4)/CoFeB(1), as shown in figure 5.15, the SOT tendency depending on the irradiation dose seems to be shifted towards high doses, leading to the mismatch in the domain wall dynamics. Thus, the performance of the too-thick Ta/CoFeB thin film would not be as good as that of Ta(3)/CoFeB(1). Besides, the change of the field-like effective field H_{FL} of Ta(4)/CoFeB(1) is always decreasing after irradiation until the maximum dose $10 \times 10^{14}\,He^+/cm^2$, which is very different from the Ta(2)/CoFeB(1) and Ta(3)/CoFeB(1). The reason is unclear so far. Samples irradiated by higher doses would help reveal the whole tendency of it.

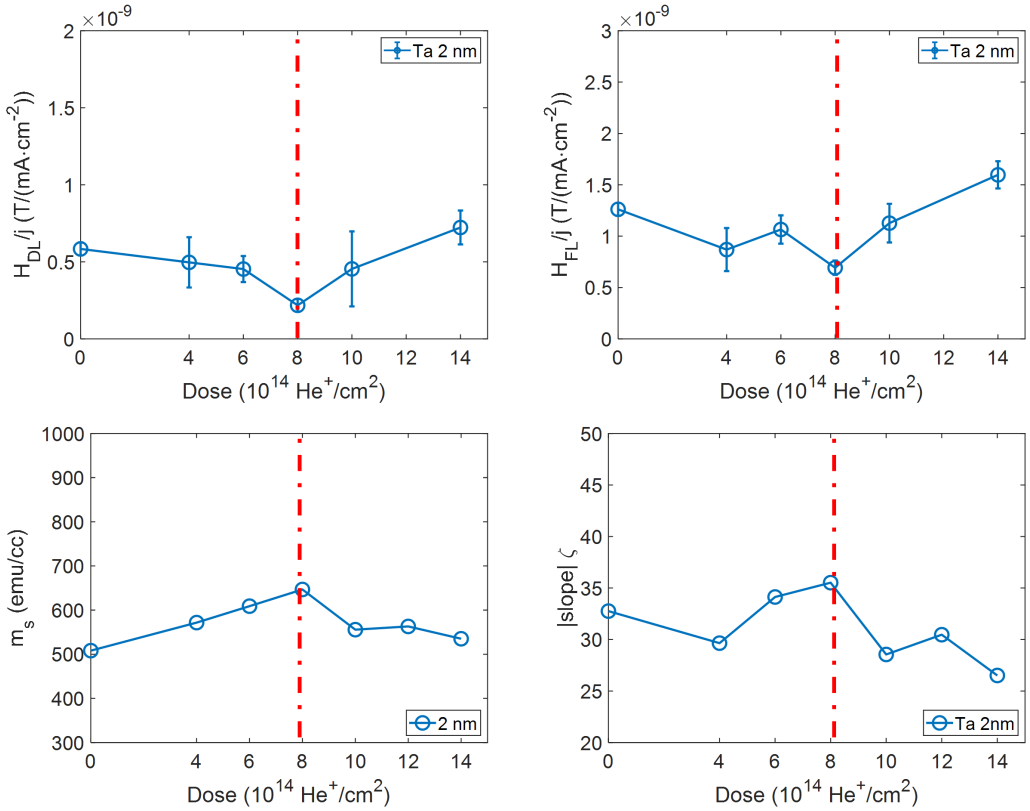

FIGURE 5.13: The summary of results of Ta(2)/CoFeB(1).

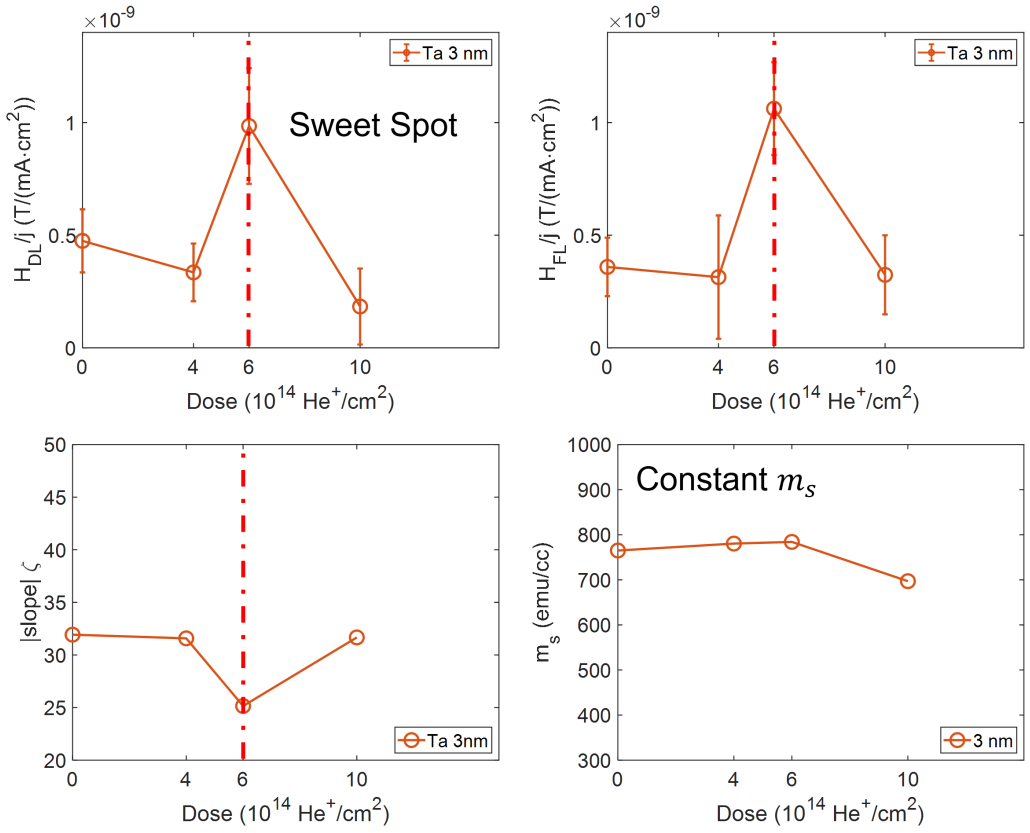

FIGURE 5.14: The summary of results of Ta(3)/CoFeB(1).

The high dependence of He^+ irradiation on the thickness of the Ta layer means that we should carefully consider the thickness of the thin film in the application of this technology. On the one hand, the He^+ ion irradiation shows an impressively excellent improvement on different properties when it meets the sweet spot of Ta/CoFeB, showing the great potential on the device application. On the other hand, this technology is highly sensitive to the thickness, which may limit the design and stacks of spintronic devices.

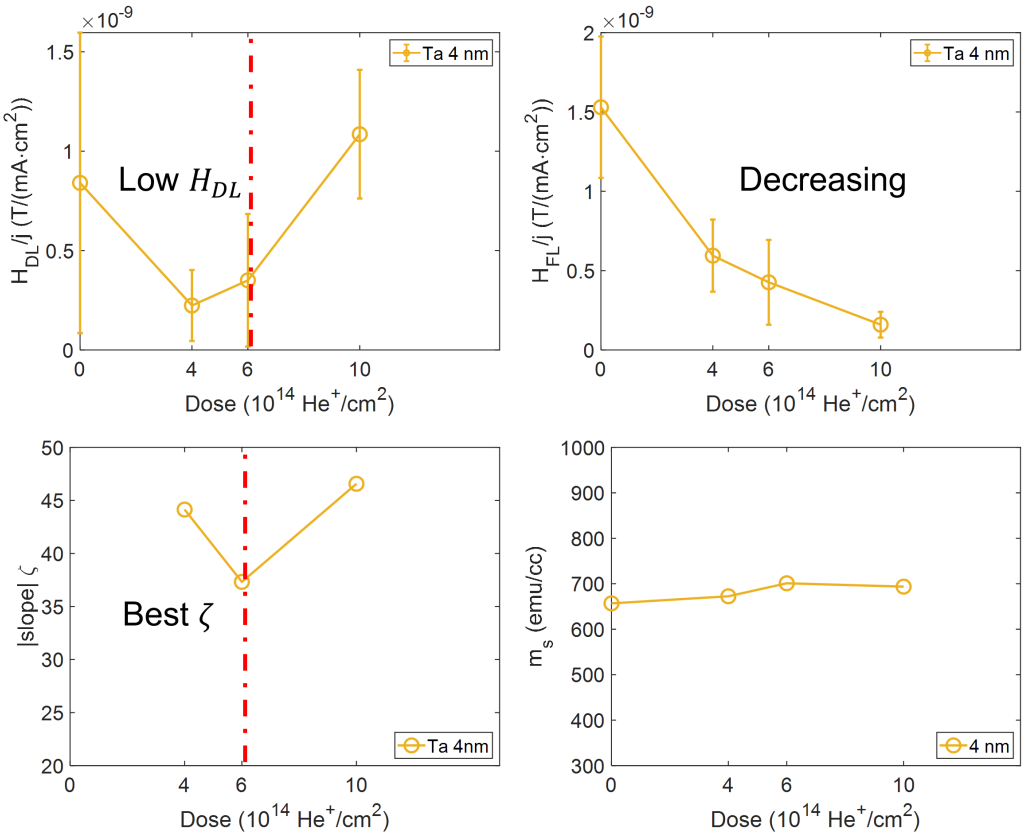

FIGURE 5.15: The summary of results of Ta(4)/CoFeB(1).

Chapter 6

Conclusion

6.1 Conclusion

As a non-destructive and convenient method modifying the properties of materials, He^+ ion irradiation technology has attracted great interest in investigating the mechanism and effects for promoting its application on spintronic devices, especially the domain-based devices like racetrack memory. However, most of the studies are only focusing on the domain wall motion or the magnetic properties such as m_s and K_{eff}, and lack of studies on the SOT properties, which is also critical for the spintronic devices. On the other hand, He^+ ion irradiation often shows different effects in different systems or even similar systems, which can not be well understood before.

Therefore, the objective of this thesis is to clarify the effects of He^+ ion irradiation on both domain wall motion and spin-orbit torque in Ta/CoFeB thin film for domain wall devices. To achieve this objective, we break it into three sub-objectives:

Sub-objective 1: The dose-dependent effect on the magnetic properties and the origin of it. Magnetic properties attracted most of the attention in previous studies and are highly relative to the domain wall motion. In Chapter 3, we demonstrated that the dose-dependent effects differ on thinner and thicker Ta/CoFeB thin films. In the case of the thicker Ta(3,4)/CoFeB(1) samples, the magnetic properties keep constant with different doses. In comparison, in the case of the thinner Ta(2)/CoFeB(1) samples, the magnetic properties are highly modulated by the irradiation doses. Furthermore, we conclude that the origin of the modulation in Ta(2)/CoFeB(1) is the change of crystallinity and first demonstrates the crystallization of the CoFeB (110) phase.

Sub-objective 2: To clarify the domain wall motion of irradiated samples, figuring out the microscopic pinning properties. In Chapter 4, we present the analysis, which shows a significant improvement in the thicker Ta(3,4)/CoFeB(1) with irradiation dose $6 \times 10^{14}\,He^+/cm^2$. To clarify the dominant contribution to the improvement in domain wall motion, we measured the m_s and K_{eff} of the irradiated samples, which are proved not the dominant contribution. By excluding the m_s and K_{eff}, the only remaining candidate pinning density n_i is determined. The results elucidate that the

He^+ ion irradiation can modify and improve the microscopic pinning properties.

Sub-objective 3: To analyze the spin-orbit torque of irradiated samples for determining the modulation from He^+ ion irradiation using the harmonic Hall method. In Chapter 5, we present the results of SOT properties modulated by He^+ ion irradiation. In the case of Ta(2)/CoFeB(1), the effect of irradiation generally behaves as damage, and the SOT gets worst in the irradiation dose $8 \times 10^{14}\,He^+/cm^2$, which is also the worst point of domain wall dynamics, suggesting the negative effect of irradiation. In the case of Ta(3,4)/CoFeB(1), the Ta(3)/CoFeB(1) shows the strongest SOT in the irradiation dose $6 \times 10^{14}\,He^+/cm^2$, which is also the best point of other properties. The irradiation dose $6 \times 10^{14}\,He^+/cm^2$ is a sweet spot of Ta(3)/CoFeB(1), where the best value of the main properties can be reached simultaneously. However, the SOT of Ta(4)/CoFeB(1) seems to be different in that it needs a higher dose to improve the damping-like effective field, which makes it miss the sweet spot of other properties.

Combining with the sub-objectives, we first finished a systemic study on the effects of He^+ ion irradiation for the spintronic device application, clarified the different contributions of them, and pointing out that the He^+ ion irradiation is highly sensitive to the thickness of samples.

6.2 Outlook

This thesis clarified the different effects of He^+ ion irradiation on Ta/CoFeB thin films, and pointting out the sensitivity to the thickness. Devices with high performance by modifying the properties with ion irradiation are possible to succeed in the future. In addition, the sensitivity to the thickness also hinders the application of this technology. To solve this problem, the dependence between the parameters of He^+ ion irradiation (e.g. energy, beam density, temperature...) should be investigated. If we can control the sweet spot of thickness by controlling those parameters, the application of He^+ ion irradiation technology would be much pushed.

References

[1] Ioan Mihai Miron et al. “Perpendicular switching of a single ferromagnetic layer induced by in-plane current injection”. In: *Nature* 476.7359 (2011), pp. 189–193.

[2] Dan A Allwood et al. “Magnetic domain-wall logic”. In: *science* 309.5741 (2005), pp. 1688–1692.

[3] Jean Anne Currivan et al. “Low energy magnetic domain wall logic in short, narrow, ferromagnetic wires”. In: *IEEE Magnetics Letters* 3 (2012), pp. 3000104–3000104.

[4] Satoru Emori et al. “Current-driven dynamics of chiral ferromagnetic domain walls”. In: *Nature materials* 12.7 (2013), pp. 611–616.

[5] Durgesh Kumar et al. “Domain wall memory: Physics, materials, and devices”. In: *Physics Reports* 958 (2022), pp. 1–35.

[6] Gwang-Guk An et al. “Highly enhanced perpendicular magnetic anisotropic features in a CoFeB/MgO free layer via WN diffusion barrier”. In: *Acta Materialia* 110 (2016), pp. 217–225.

[7] Masahiro Kudo et al. “Crystal orientation of epitaxial α-Ta (110) thin films grown on Si (100) and Si (111) substrates by sputtering”. In: *Japanese journal of applied physics* 47.7R (2008), p. 5608.

[8] S Gnanarajan, SKH Lam, and A Bendavid. “Coexistence of epitaxial Ta (111) and Ta (110) oriented magnetron sputtered thin film on c-cut sapphire”. In: *Journal of Vacuum Science & Technology A* 28.2 (2010), pp. 175–181.

[9] Jun Hayakawa et al. "Dependence of giant tunnel magnetoresistance of sputtered CoFeB/MgO/CoFeB magnetic tunnel junctions on MgO barrier thickness and annealing temperature". In: *Japanese Journal of Applied Physics* 44.4L (2005), p. L587.

[10] Xiang Li et al. "Enhancement of voltage-controlled magnetic anisotropy through precise control of Mg insertion thickness at CoFeB| MgO interface". In: *Applied Physics Letters* 110.5 (2017).

[11] SU Jen et al. "Magnetic and electrical properties of amorphous CoFeB films". In: *Journal of applied physics* 99.5 (2006).

[12] A Ramazani et al. "Magnetic behavior of as-deposited and annealed CoFe and CoFeCu nanowire arrays by ac-pulse electrodeposition". In: *Journal of crystal growth* 402 (2014), pp. 42–47.

[13] *Spin-Ion Technologies*. URL: https://www.spin-ion.com/.

[14] *Recipe for S1813 resist*. URL: https://www.tudelft.nl/en/faculty-of-applied-sciences/about-faculty/departments/quantum-nanoscience/kavli-nanolab-delft/equipment/process-recipes/resist-recipes/recipe-for-s1813-resist.

[15] Brad Dodrill and Jeffrey R Lindemuth. "Vibrating sample magnetometry". In: *Magnetic measurement techniques for materials characterization* (2021), pp. 15–37.

[16] *Vibrating-sample magnetometer*. 2023. URL: https://en.wikipedia.org/wiki/Vibrating-sample_magnetometer.

[17] T Devolder. "Light ion irradiation of Co/Pt systems: Structural origin of the decrease in magnetic anisotropy". In: *Physical Review B* 62.9 (2000), p. 5794.

[18] Lalminthang Kipgen et al. "In-plane magnetic anisotropy and coercive field dependence upon thickness of CoFeB". In: *Journal of magnetism and magnetic materials* 324.19 (2012), pp. 3118–3121.

[19] D Stanescu et al. “Tailoring magnetism in CoNi films with perpendicular anisotropy by ion irradiation”. In: *Journal of Applied Physics* 103.7 (2008), 07B529.

[20] T Blon et al. “Effects of ion irradiation on cobalt thin films magnetic anisotropy”. In: *Journal of Magnetism and Magnetic Materials* 272 (2004), E803–E805.

[21] Anmol Mahendra et al. “Tailoring of magnetic anisotropy by ion irradiation for magnetic tunnel junction sensors”. In: *Journal of Alloys and Compounds* 910 (2022), p. 164902.

[22] Jeffrey McCord et al. “Magnetic anisotropy and domain patterning of amorphous films by He-ion irradiation”. In: *Applied Physics Letters* 86.16 (2005).

[23] Johannes Wilhelmus van der Jagt. “Tailoring magnetic phenomena and disorder in ultra-thin films with He irradiation”. PhD thesis. Université Paris-Saclay, 2023.

[24] L Herrera Diez et al. “Controlling magnetic domain wall motion in the creep regime in He+-irradiated CoFeB/MgO films with perpendicular anisotropy”. In: *Applied Physics Letters* 107.3 (2015).

[25] Suhyeok An et al. “Improved spin–orbit torque induced magnetization switching efficiency by helium ion irradiation”. In: *Scientific Reports* 12.1 (2022), p. 3465.

[26] Xiaoxuan Zhao et al. “Enhancing domain wall velocity through interface intermixing in W-CoFeB-MgO films with perpendicular anisotropy”. In: *Applied Physics Letters* 115.12 (2019).

[27] L Herrera Diez et al. “Enhancement of the Dzyaloshinskii-Moriya interaction and domain wall velocity through interface intermixing in Ta/CoFeB/MgO”. In: *Physical Review B* 99.5 (2019), p. 054431.

[28] Giovanni Esteves et al. “LIPRAS: Line-profile analysis software”. In: *Preprint at https://www. researchgate. net/publication/316985889_LIPRAS_Line-Profile_Analysis_Software* (2017).

[29] Kun Huang. *Solid state physics*. Higher Education Press, 2014.

[30] Charles Kittel and Paul McEuen. *Introduction to solid state physics*. John Wiley & Sons, 2018.

[31] James F Ziegler and Jochen P Biersack. “The stopping and range of ions in matter”. In: *Treatise on Heavy-Ion Science: Volume 6: Astrophysics, Chemistry, and Condensed Matter*. Springer, 1985, pp. 93–129.

[32] Thibaut Devolder. “Structuration et nanostructuration de couches magnétiques Co/Pt par irradiation ionique”. PhD thesis. Paris 11, 2000.

[33] T Devolder et al. “Magnetic properties of He+-irradiated Pt/Co/Pt ultrathin films”. In: *Physical Review B* 64.6 (2001), p. 064415.

[34] J Ferré et al. “Magnetic phase diagrams of He ion-irradiated Pt/Co/Pt ultrathin films”. In: *Journal of Physics D: Applied Physics* 36.24 (2003), p. 3103.

[35] P Mazalski et al. “Ion irradiation induced enhancement of out-of-plane magnetic anisotropy in ultrathin Co films”. In: *Journal of Applied Physics* 113.17 (2013).

[36] Cristina Balan et al. “Control of domain wall and pinning disorder interaction by light He^+ ion irradiation in Pt/Co/AlOx ultrathin films”. In: *arXiv preprint arXiv:2303.04577* (2023).

[37] Stuart SP Parkin, Masamitsu Hayashi, and Luc Thomas. “Magnetic domain-wall racetrack memory”. In: *Science* 320.5873 (2008), pp. 190–194.

[38] WS Zhao et al. “A compact model of domain wall propagation for logic and memory design”. In: *Journal of applied physics* 109.7 (2011).

[39] Arne Brataas, Andrew D Kent, and Hideo Ohno. “Current-induced torques in magnetic materials”. In: *Nature materials* 11.5 (2012), pp. 372–381.

[40] Aurelien Manchon et al. “Current-induced spin-orbit torques in ferromagnetic and antiferromagnetic systems”. In: *Reviews of Modern Physics* 91.3 (2019), p. 035004.

[41] P Géhanne et al. “Strength and length scale of the interaction between domain walls and pinning disorder in thin ferromagnetic films”. In: *Physical Review Research* 2.4 (2020), p. 043134.

[42] Naoto Nagaosa et al. “Anomalous hall effect”. In: *Reviews of modern physics* 82.2 (2010), p. 1539.

[43] T Jungwirth, Qian Niu, and AH MacDonald. “Anomalous Hall effect in ferromagnetic semiconductors”. In: *Physical review letters* 88.20 (2002), p. 207208.

[44] MT Johnson et al. “Magnetic anisotropy in metallic multilayers”. In: *Reports on Progress in Physics* 59.11 (1996), p. 1409.

[45] Satoshi Okamoto et al. “Enhancement of magnetic surface anisotropy of Pd/Co/Pd trilayers by the addition of Sm”. In: *Journal of Applied Physics* 90.8 (2001), pp. 4085–4088.

[46] S Okamoto et al. “Chemical-order-dependent magnetic anisotropy and exchange stiffness constant of FePt (001) epitaxial films”. In: *Physical Review B* 66.2 (2002), p. 024413.

[47] Junyeon Kim et al. “Layer thickness dependence of the current-induced effective field vector in Ta| CoFeB| MgO”. In: *Nature materials* 12.3 (2013), pp. 240–245.

[48] Baoshan Cui et al. “Field-free spin–orbit torque switching of perpendicular magnetization by the Rashba interface”. In: *ACS applied materials & interfaces* 11.42 (2019), pp. 39369–39375.

[49] Qiming Shao et al. “Strong Rashba-Edelstein effect-induced spin–orbit torques in monolayer transition metal dichalcogenide/ferromagnet bilayers”. In: *Nano letters* 16.12 (2016), pp. 7514–7520.

[50] Hiromu Gamou et al. “Enhancement of spin current generation in epitaxial α-Ta/CoFeB bilayer”. In: *Physical Review B* 99.18 (2019), p. 184408.

[51] Qiang Hao and Gang Xiao. “Giant spin Hall effect and magnetotransport in a Ta/CoFeB/MgO layered structure: A temperature dependence study”. In: *Physical Review B* 91.22 (2015), p. 224413.

[52] Can O Avci. “Current-induced effects in ferromagnetic heterostructures due to spin-orbit coupling”. PhD thesis. ETH Zurich, 2015.

[53] RYAN BRENT THOMPSON. “Crystal Orientation Dependence of Spin-orbit Torque in Epitaxial Pt Thin Films for Spintronic Applications”. PhD thesis. Tohoku University, 2021.

[54] Jairo Sinova et al. “Spin hall effects”. In: *Reviews of modern physics* 87.4 (2015), p. 1213.

[55] Tomas Jungwirth, Jörg Wunderlich, and Kamil Olejník. “Spin Hall effect devices”. In: *Nature materials* 11.5 (2012), pp. 382–390.

[56] Victor M Edelstein. “Spin polarization of conduction electrons induced by electric current in two-dimensional asymmetric electron systems”. In: *Solid State Communications* 73.3 (1990), pp. 233–235.

[57] Junsaku Nitta et al. “Gate control of spin-orbit interaction in an inverted I n 0.53 G a 0.47 As/I n 0.52 A l 0.48 as heterostructure”. In: *Physical Review Letters* 78.7 (1997), p. 1335.

[58] Seonghoon Woo et al. “Enhanced spin-orbit torques in Pt/Co/Ta heterostructures”. In: *Applied Physics Letters* 105.21 (2014).

[59] Luqiao Liu et al. “Spin-torque ferromagnetic resonance induced by the spin Hall effect”. In: *Physical review letters* 106.3 (2011), p. 036601.

[60] Minh-Hai Nguyen, DC Ralph, and RA Buhrman. “Spin torque study of the spin Hall conductivity and spin diffusion length in platinum thin films with varying resistivity”. In: *Physical review letters* 116.12 (2016), p. 126601.

Acknowledgements

I would like to thank Prof. Junsaku Nitta and Prof. Makoto Kohda first. As my supervisors in the stages of my master's and doctorate, they gave me a lot of guidance and suggestions, which shed light on the direction of my scientific path. I still remember when I first came to Sendai on a snowy day, Prof. Nitta introduced his laboratory to me and warmly accepted me to join his lab as a fresh student. After his retirement, Prof. Kohda became my supervisor for the doctoral course. Although we faced countless difficulties in research or facilities, their encouragement and teaching helped me finally overcome those problems. The terrible epidemic of COVID-19 burst out in the second year of my master's course and has continued for four years until now, which has disorganized almost everything in my research and daily life. Fortunately, with their kind help and tolerance, I successfully adjusted the direction, and everything got on the right track in time.

I would also like to thank Assist. Prof. Shutaro Karube and Assist. Prof. Chaoliang Zhang in my lab. As a foreign student, I often encounter many inconveniences in the complicated paperwork processes, in different symposiums or workshops, or my daily life. Thanks to their kind help, I can easily learn how to handle those issues and adapt to the new environment. They also teach a lot in my experiments with their rich experience, especially in the part of VSM measurements and harmonic Hall measurements. Although they have left my lab, I still miss them very much. I also thank our new Assistant. Prof. Jun Ishihara and Assist. Prof. Sota Yamamoto, thank you for your help in my defense.

Besides, I would like to thank Researcher Liza Herrera Diez, my supervisor at the University of Paris-Sclay. The domain wall motion measurements in this work are completed under her guidance. She is very professional in both the physics and experiments of magnetic domains. Her supervision is the key for me to complete Chapter 4. I enjoyed the time we discussed the physics and experiments very much.

Moreover, she helped me a lot in my life in Paris, I often feel sorry for occupying her time so much.

While completing this thesis, I would like to thank Prof. Yuji Sutou, Prof. Mikihiko Oogane, Prof. Rie Umetsu, Prof. Takeshi Seki, and Assoc. Prof. Nobuki Tezuka for their valuable comments and suggestions. Their constructive criticism is very helpful for me to improve my thesis.

I would also like to thank the members of my lab. Aya Saitou, the secretary of my lab, you are always enthusiastic to help me finish complicated paperwork and often invites me to join some very funny parties. Dr. Hiromu Gamou, you are as kind as a big brother to me and always care about the younger students in our lab. You taught me many experiment skills even after your graduation, which are essential for finishing this work. Dr. Keita Nakagawara, the specialist on facilities in my lab, thank you for your great help in my experiments. Dr. Ryan Brent Thompson, thank you so much for suggesting my study. Zihao Fan, thank you so much for your help in my daily life. As a freshman joining our lab the same year, I greatly enjoyed our time together. Takeshi Odagawa, Kazuki Koyama, and many other members of my lab that I can not list here, thank you for the time we spent studying together.

Finally, I would like to thank my parents. Struggling for a doctoral degree is a very tough job. I can not finish it without your support and tolerance. I appreciate your encouragement despite how many things have changed during these years. After the burst of COVID-19, I haven't been back home for four years. As the family's only son, I felt really sorry that I couldn't accompany you during the most difficult time of the epidemic. Thank you from the bottom of my heart.